Deliverable 5.3: Report on the final demonstrator

Editors:	TID/UPM	
Deliverable nature:	Document, report (R)	
Dissemination level:	Public (PU)	
Date: planned | actual	31 July 2023	6 October 2023
Version | No. of pages	1.0	67
Keywords:	D-band radios, directional links, cross-polarization interference cancellation, reflectarray antennas, metasurfaces, AI / ML networking	

Abstract

This deliverable presents the final results of all the project demonstrators envisioned in ARIADNE. The two hardware demonstrators make use of all the development work of WP3, while the work outcomes of WP4 lead to the software demonstrators. The deliverable extends the intermediate results presented in the intermediate deliverable D5.2.

This project has received funding from the European Union's Horizon 2020 research and innovation program under grant agreement No 871464. This publication reflects only the author's view and the European Commission is not responsible for any use that may be made of the information it contains.

Impressum

Full project title: Artificial Intelligence Aided D-band Network for 5G Long Term Evolution

Short project title: ARIADNE

Number and title of work-package: WP5 - Demonstration of Intelligent D-Band Network

Number and title of tasks:

Task 5.2 - Point-to-point outdoor demonstration

Task 5.3 - Metasurface demonstration

Task 5.4 - Intelligent D-band network demonstration

Document title: Report on the final demonstrator

Editors: TID/UPM

Work-package leader: Evangelos Pikasis, ICOM

Executive summary

This deliverable presents the final measurements and results carried out in ARIADNE for its varied hardware in order to assess the different technologies and architectures researched within the project.

It represents an update over D5.2, in which intermediate results and integration activities at the time of its delivery, during integration phase, were presented.

These demonstrators are based on the developed hardware and software from WP3 and WP4, respectively. The following 3 demonstrators are reported in this deliverable:

- A Point-to-Point Line-of-Sight hardware demonstrator working at D-band frequencies.
- A metasurface-enabled Point-to-Point non-Line-of-Sight hardware demonstrator working at D-band frequencies.
- Various Software demonstrators addressing multiple scenarios of Machine Learning and Artificial Intelligence supported B5G networking topics.

By envisioning beyond 5G networks, ARIADNE has set three key research targets:

- (I) development of new radio technologies using the above 100 GHz D-Band frequency range,
- (II) exploitation of advanced connectivity based on metasurfaces
- (III) application of Machine Learning and Artificial Intelligence techniques to network management.

The main objective of the first hardware demonstrator is to showcase an error-free long-range outdoor communication, which will validate the capability of the developed hardware of work package 3 for reliable communication at the D band, addressing key target (I).

The main objective tackled by the second hardware proof-of-concept demonstrator is to showcase, that an alternative propagation route can be established in which a transmitted beam is reflected in a reconfigurable manner towards the intended receiver using metasurface structures, thus maintaining the reliability of the communication, addressing key target (II).

The third and final software demonstrator is addressing key target (III), showing that reliability across the whole D-band network can be maintained by applying ML/AI techniques to solve problems like beamforming selection and different aspects of UE-AP association.

List of authors

Coordinator of this deliverable is TID/UPM. Technical contributors are all partners participating in the work package. The technical quality is assured by the Technical Manager Prof. Angeliki Alexiou, the WP Leader ICOM and the Task Leaders ICOM (Task 5.1), IAF (Task 5.2), AALTO (Task 5.3) and NCSRD (Task 5.4).

Company	Author	Contribution
TID/UPM	Rafael Cantó	Editor
IAF	Benjamin Baumann	Input to Section 2 & 3
IAF	Christian Zech, Sébastien Chartier	Document review
ICOM	Evangelos Pikasis, Elias Tsirbas, Sotirios Aloimonos, Spiridon Grigoriadis, Dimitrios Mylonakis, Dimitrios Kritharidis	Input to Section 2
NCSRD	Aris Tsolis, Antonis Alexandridis, Stefanos Lampiris	Input to Section 3
NCSRD	Fotis Lazarakis, Kyriakos Manganaris, Nikos Katzouris, Elias Alevizos	Input to Section 4
Altair RapidMiner	Edwin Yaqub, Rachana Desai	Input to Section 4
Nokia	Tachporn Sanguanpuak	Input to Section 4
UPRC	Angeliki Alexiou	Final review & editing
EUR	Halid Hrasnica	Final review

Table of Contents

Executive summary 3
List of authors 4
Table of Contents 5
List of figures and tables 6
Abbreviations 9
1 Introduction 10
2 Demonstrator 1: A Point-to-Point Line-of-Sight Link 11
2.1 Test-bed Description 11
2.1.1 Indoor Testbed 11
2.1.2 Outdoor Testbed 14
2.2 Demonstration Scenario 17
2.3 Measurement and Results 18
3 Demonstrator 2: A Metasurface-enabled point-to-point NLoS link 27
3.1 Test-bed Description 27
3.2 Demonstration Scenario 28
3.3 Realization of dielectric lens antennas 28
3.3.1 Dielectric lens antennas final design and prototyping 28
3.3.2 Manufacturing / assembly of lens antennas and feed-package 36
3.4 Measurement and Results 39
4 Demonstrator 3: An intelligent D-Band network demonstrator 43
4.1 AI/ML application for LoS-aware directional connectivity 43
4.1.1 Demonstration scenario 1.1: AI/ML based UE-AP association (a joint resource allocation and LoS blockage minimization problem) in dense and evolving networks 44
4.1.2 Demonstration scenario 1.2: Exploration of ML predictions for environment-specific LoS Connectivity 50
4.2 Deep Reinforcement Learning for B5G Wireless Communications 56
4.3 Complex Event Forecasting for Handover Reduction 60
4.3.1 Demonstration Scenario 3.1: Handover reduction in time evolving scenarios using FFA for UE-AP association 60
5 Conclusions 65
References 67

List of figures and tables

List of figures:

Figure 2-1: The two pairs of the integrated BBUs/RFUs 11
Figure 2-2: Indoor testing at distances of 6m and 12m 12
Figure 2-3: Constellation diagrams of the recovered 4-QAM symbols of the two modems of BBU_1 corresponding to each polarization: (a) horizontal and (b) vertical. 13
Figure 2-4: Constellation diagrams of the recovered 4-QAM symbols of the two modems of BBU_2 corresponding to each polarization: (a) horizontal and (b) vertical. 13
Figure 2-5: Indoor link validation via streaming video test. 14
Figure 2-6: The 226 m link distance between the poles at the rooftops of the two buildings on ICOM premises. 14
Figure 2-7: The two installed BBU/RFU pairs on the poles of the two buildings on ICOM premises. 15
Figure 2-8: The spectrum analyzer used in the alignment process 15
Figure 2-9: The USB power meter used for the alignment process 16
Figure 2-10: The spectrum analyser's screen used for the alignment process 16
Figure 2-11: The GUI on the PC of the USB power meter showing the received RF power in dBm 16
Figure 2-12: Test Plan Flowchart 18
Figure 2-13: System topology for dual-polarization transmission/reception in ARIADNE [3] 19
Figure 2-14: Block diagram of the outdoor experimental setup 19
Figure 2-15: Free space path loss in the frequency range 150 to 160GHz based on Friis transmission formula [1, 2] 20
Figure 2-16: Histogram distribution of the received power in both modems of BBU-2 21
Figure 2-17: Power spectrum magnitude of the received QAM signals in the 1st modem of the BBU-1 21
Figure 2-18: Power spectrum magnitude of the received QAM signals in the 2nd modem of the BBU-1 21
Figure 2-19: Power spectrum magnitude of the received QAM signals in the 1st modem of the BBU-2 22
Figure 2-20: Power spectrum magnitude of the received QAM signals in the 2nd modem of the BBU-2 22
Figure 2-21: Constellation diagrams of the recovered QAM signals of the two modems of the BBU-1 22
Figure 2-22: Constellation diagrams of the recovered QAM signals of the two modems of the BBU-2 23
Figure 2-23: Constellation diagrams of the recovered QAM signals for the case of 16- and 32-QAM 23
Figure 2-24 : Time traces and histogram distributions of the estimated XPD (dB) based on XPIC algorithm 24
Figure 2-25: Estimated BER vs. estimated SNR (dB) 24
Figure 2-26 : (a) The free space path losses based on Friis formula versus the operating carrier frequency in the range of 150GHz up to 160GHz and the estimated losses in dB of D-band link, and (b) the estimated path losses (F, 1m) and path loss exponent versus the operating carrier frequency 25
Figure 2-27: Experimental setup for testing reflection coefficients. The values of Y are the experimentally achieved efficiencies of anomalous reflection at the three operational frequencies 26
Figure 3-1: Metasurface geometry and simulated efficiency of anomalous reflection ("LL" - lossless model, "Lossy" - simulations include the effects of dissipation) 27
Figure 3-2: Sample manufacturing (Aalto University facilities) 27
Figure 3-3: Demonstrator scenario: delivering a D-band signal into the shadow of a wall via reflections in an anomalously reflecting metasurface 28
Figure 3-4: Lens misalignment to horn position (lens antenna side view and top view) 29
Figure 3-5: Contour plots of gain radiation patterns for various misalignment cases (Δx, Δy): (a) (0mm, 0mm), (b) (0.5mm, 0mm), (c) (-0.5mm,0mm), (d) (0.5mm,-0.5mm). 30
Figure 3-6: Evolution of the design of lens with the feed horn package 31
Figure 3-7: Three 0deg-tilt lenses for various F (15mm, 20mm, 25mm) and 20deg-titled lens with F=25mm 31
Figure 3-8: Feed horn package and CWG-to-RWG transition 32
Figure 3-9: a) Horn with CWG-to-RWG transition, b) S11 performance 32
Figure 3-10: Radiation pattern of horn antenna at E-plane and H-plane 33
Figure 3-11: Radiation pattern (E-plane) of lens antenna (F=15mm) @144.75GHz with and without package 33
Figure 3-12: Radiation pattern (E-plane) of lens antenna (F=15mm) @144.75GHz with and without phase center correction 34

Figure 3-13: Simplified designs: 0° tilt lenses for various F (15mm, 20mm, 25mm) and titled lens for F=25mm . 34
Figure 3-14: Far Field radiation patterns (H-plane) for lenses F=25mm (0°and 20° tilt) at 144.75GHz (green: "carved-base", red: "flat-base")..... 35
Figure 3-15: Final lens antenna model adjustments (details) for manufacturing (from step CAD file). a) waveguide port, b) dielectric lens (tilted)..... 35
Figure 3-16: Manufactured horn-package (a) and exemplary HDPE 20 ° tilted lens (b)..... 36
Figure 3-17: Lens antennas characterization measurement set-up at IAF..... 37
Figure 3-18: Lens antennas measurement procedure at IAF 37
Figure 3-19: Radiation patterns E and H-planes of 0° tilted lenses for F=15mm, F=20mm and F=25mm 38
Figure 3-20: Radiation pattern (H-plane) of 20° tilted lens, F=25mm..... 39
Figure 3-21:: Lab environment with MTS measurement set-up. Anechoic material around wafer removed for enhanced visibility..... 40
Figure 3-22: Left: Block-diagram of measurement setup of a MTS-enabled PtP NLoS demonstration targeting demonstrator 2. Right: Angular coherencies of the proposed measurement setup w.r.t. the moving robot arm. (a): 0 °, (b): +10 ° (specular reflection), (c): -40 ° (anomalous reflection)..... 40
Figure 3-23: Far-field radiation plot of MTS sample S05 at various frequencies using proposed measurement setup. Design-frequency of S05 is 157.75 GHz..... 41
Figure 3-24: Far-field radiation plot of MTS sample S06 at various frequencies using proposed measurement setup. Design-frequency of S06 is 144.75 GHz..... 42
Figure 3-25: Far-field radiation plot of MTS sample S08 at various frequencies using proposed measurement setup. Design-frequency of S08 is 170.9 GHz..... 42
Figure 3-26: Metasurface demonstration on the EuCNC in Gotheburg 2023 43
Figure 4-1: Design of Hybrid Metaheuristic-Machine Learning Framework 44
Figure 4-2: Conceptual design of demonstration application 45
Figure 4-3: AI/ML Demonstrator for UE-AP Associations - View of Online Optimizer Module 46
Figure 4-4 A new UE added in the network..... 47
Figure 4-5 An existing UE is moved in the network..... 47
Figure 4-6 Before Resource Change Trigger: UE104 requires 2.0 MHz bandwidth resource and is assigned to AP104 48
Figure 4-7: After Resource Change Trigger: UE104 now requires 5.0 MHz bandwidth resource and is assigned to AP10..... 48
Figure 4-8 Addition and Removal of an AP 49
Figure 4-9: AI/ML Demonstrator for UE-AP Associations - View of Online Predictor Module..... 50
Figure 4-10: Conceptual design to explore the influence of features on ML predictions 52
Figure 4-11: Demonstrator Homepage 53
Figure 4-12: Import Data..... 54
Figure 4-13: Interactive exploration of observed vs predicted and NLOS vs LOS values 55
Figure 4-14: Correlation chart showing positively and negatively influencing attributes..... 55
Figure 4-15: Predefined beam codebook selection 57
Figure 4-16: Iillustration of single-agent DRL for beam prediction with the association of observation space, environment, and action space..... 57
Figure 4-17: Reward versus number of episodes 58
Figure 4-18: Value variation versus reward 58
Figure 4-19: Histogram of Reward..... 58
Figure 4-20: Reward versus number of episodes 59
Figure 4-21: Value loss function versus number of episodes..... 59
Figure 4-22: Histogram of reward when BS/gNB serves 20, 25, and 30 UEs 60
Figure 4-23 Trajectories of 8 UEs within simulated geographical area. The largest dot of a specific trajectory corresponds to the initial placement of the UE, while the smallest one corresponds to its final position. 61
Figure 4-24: Network's graph for the application of max-fow algorithm (FFA) towards UEs allocation to APs... 63
Figure 4-25 Snapshot of UEs' placement (blue dots) within the simulated area at the 131st time slot of the simulation session. At the right side, the load of each AP is provided with and without AI together with Wayeb score..... 64

Figure 4-26 Snapshot of time evolved handover performance with and without forecasting at the 131st time slot of the simulation session *64*
Figure 4-27 Snapshot of UEs' placement (blue dots) within the simulated area at the 1489th time slot of the simulation session. At the right side, the load of each AP is provided with and without AI together with Wayeb score *65*
Figure 4-28 Snapshot of time evolved handover performance with and without forecasting at the 1489th time slot of the simulation session *65*

List of tables:

Table 2-1: The functional parameters and their values *19*
Table 3-1: Gain variation for misalignment cases (Δx, Δy) at theta=-20.5 deg *30*
Table 4-1 APs coordinates *61*

Abbreviations

Abbreviation	Explanation
AD	Analog-to-Digital
AI	Artificial Intelligence
AP	Access Point
B5G	Beyond 5G
BBU	Baseband Unit
BS	Base Station
CER/F	Complex Event Recognition and Forecasting
DA	Digital-to-Analog
DC	Direct Current
DRL	Deep Reinforcement Learning
DSP	Digital Signal Processing
FFA	Ford-Fulkerson algorithm
GUI	Graphical User Interface
I/Q	In-Phase / Quadrature
IF	Intermediate Frequency
IoT	Internet of Things
LO	Local Oscillator
LoS	Line-of-Sight
ML	Machine Learning
MS	Mobile Station
MTS	Metasurface
NLoS	Non-Line-of-Sight
ODU	Outdoor Unit
PDM	Polarization Division Multiplexing
PLL	Phase-Locked-Loop
PtP	Point-to-Point
QAM	Quadrature Amplitude Modulation
RF	Radio Frequency
RFU	Radio Frequency Unit
RIS	Reconfigurable Intelligent Surface
Rx	Receiver
Tx	Transmitter
UART	Universal Asynchronous Receive and Transmit
UE	User Equipment
XPIC	Cross Polarization Interference Cancellation

1 Introduction

This document builds upon the preliminary demonstrators, and intermediate results based on hardware- and software-outcomes of WP3 and WP4, described in detail in D5.2., providing details of the final demonstrators implemented within ARIADNE, along with the measurements and results obtained by them, showing the advances over state of the art achieved within the project.

Demonstrators built within the project correspond to the challenges defined at the time of writing the proposal, structured under the different tasks defined in WP5, T5.2 Point-to-point outdoor demonstration, T5.3 Metasurface Demonstration, and T5.4 Intelligent D-Band network demonstration.

Each of those tasks addresses one of the three pillars of ARIADNE:

- PILLAR I: D-band for 100 Gbit/s reliable wireless connectivity, by means of advanced, power-efficient transceiver design, extending wireless capacity in terms of high-bandwidth, and consistently high-quality and low-latency link, making it an attractive alternative for RF backhauling in B5G technologies.
- PILLAR II: Communications beyond the Shannon paradigm, by means of metasurfaces for NLOS/obstructed LOS connectivity, enabling potential applications, such as simultaneous support of multiple wireless connections, adaptive network reconfiguration, implementation of new switching functions, or focusing on devices in the vicinity of the surfaces. For those applications, reflective metasurfaces (MTS) form the essential building blocks for implementing reconfigurable intelligent surfaces (RIS), to enable non-LoS (NLoS) wireless links.
- PILLAR III: Artificial Intelligence based wireless system concept, by means of ML approaches, enabled by software demonstrators that permit to show the use cases and opportunities that AI/ML provide to wireless communications architectures in general, and to ARIADNE in particular.

The organization of this deliverable report follows that same structure. In section 2 **Demonstrator 1: A PtP LoS Link** describes the indoor and outdoor testbeds of the PtP LoS demonstrator along the final demonstration and the obtained measurements and results with the extensive measurement campaign carried within the project. Section 3 **Demonstrator 2: A MTS-enabled PtP NLoS Link** describes the testbed created using D-band anomalous reflectors developed by WP3, the demonstration scenario, and the implementation and characterization of the medium-gain dielectric lens antenna providing the easily adaptable antenna structure required for the MTS-enabled PtP NLoS demonstrator, which has been shown at the 2023 EuCNC in Gothenburg, Sweden, with a final sub-section on measurements and results. Last, section 4 **Demonstrator 3: An intelligent D-band network** describes final results of the various software demonstrators regarding AI/ML application for LoS-aware connectivity, deep reinforcement learning for 5G/B5G wireless communications as well as complex event forecasting for proactive handover and blockage avoidance. First software demonstrator showcases the use of **AI/ML for solving the User Equipment fo Access Point association problem** under dynamic settings for very large scales and dense evolving B5G networks. Second demonstrator deals with **deep reinforcement learning** to establish algorithms to allocate proper beamforming vector to the moving UEs in order to facilitate UEs' real time interaction with the environment. Last, through system level simulations, **Complex Event Forecasting for Handover Reduction** demonstrator showcases the capability of AI/ML techniques to reduce handovers events though the deployment of Complex Event Forecasting Techniques.

2 Demonstrator 1: A Point-to-Point Line-of-Sight Link

The implementation of ARIADNE's D-band LoS PtP long-range demonstrator's two main subsystems, namely the baseband unit with the AD/DA converters board (referred to as "BBU" for simplicity) developed by ICOM and the D-band RF Unit with the Cassegrain antennas (referred to as "RFU" for simplicity) developed by IAF, followed by their integration, indoor testbed setup as well as the outdoor testing preparations, were analytically described in deliverable D5.2. In this chapter, the results of the extensive campaign executed at ICOM's HQs, first during the indoor and eventually during the outdoor testing, are presented.

2.1 Test-bed Description

2.1.1 Indoor Testbed

During the integration phase, each BBU was interconnected with an RFU using 8 SMA cables for the transmission and reception of the QAM data streams in each polarization (T_XI_H/T_XQ_H, T_XI_V/T_XQ_V, R_XI_H/R_XQ_H, R_XI_V/R_XQ_V) as shown in Figure 2-1 for the two RFU/BBU pairs.

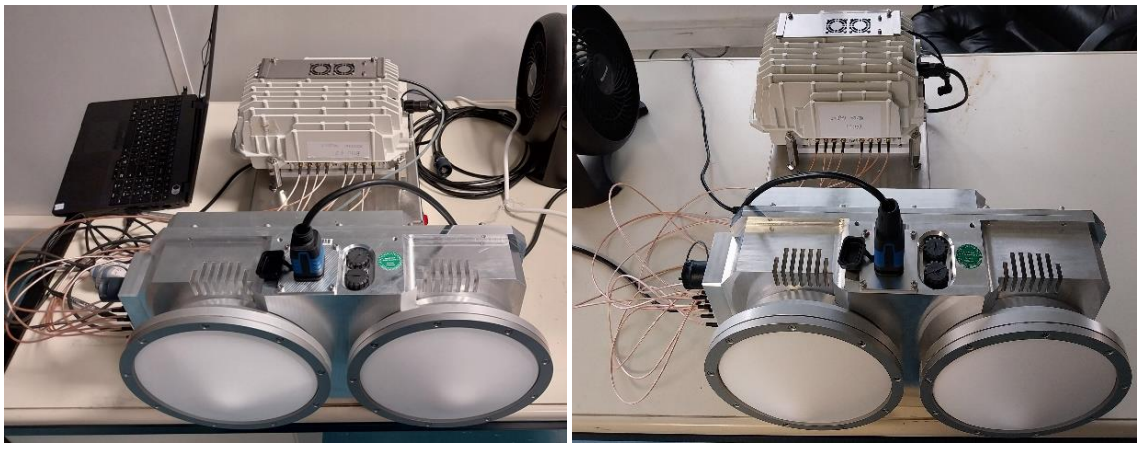

(a) (b)

Figure 2-1: The two pairs of the integrated BBUs/RFUs

Management of both the BBUs and the RFUs was performed by using the management (1GbE) Ethernet port of the BBU and the Ethernet port of the RFU, using an Ethernet switch and a laptop, installed with the required software programs for their control. Each BBU and RFU was assigned an IP address and communication with each one was achieved after power-up. Communication with the BBUs was realised through telnet, via which it was possible to control and monitor specific parameters of the baseband unit, while management of the RFUs was achieved through an IAF-provided python script that was initiating the RFUs.

ICOM initiated a set of indoor experiments to guarantee that the integrated systems would be functional and the link operational, before committing them to the outdoor poles where the effort to debug and correct any possible malfunction, would be extremely difficult as the systems would be fixed on the poles, their connectors waterproof sealed and more importantly, aligned.

Two different indoor experiments were conducted, one at a link distance of 6 m and one at 12 m, as depicted in Figure 2-2 (a) and (b) respectively.

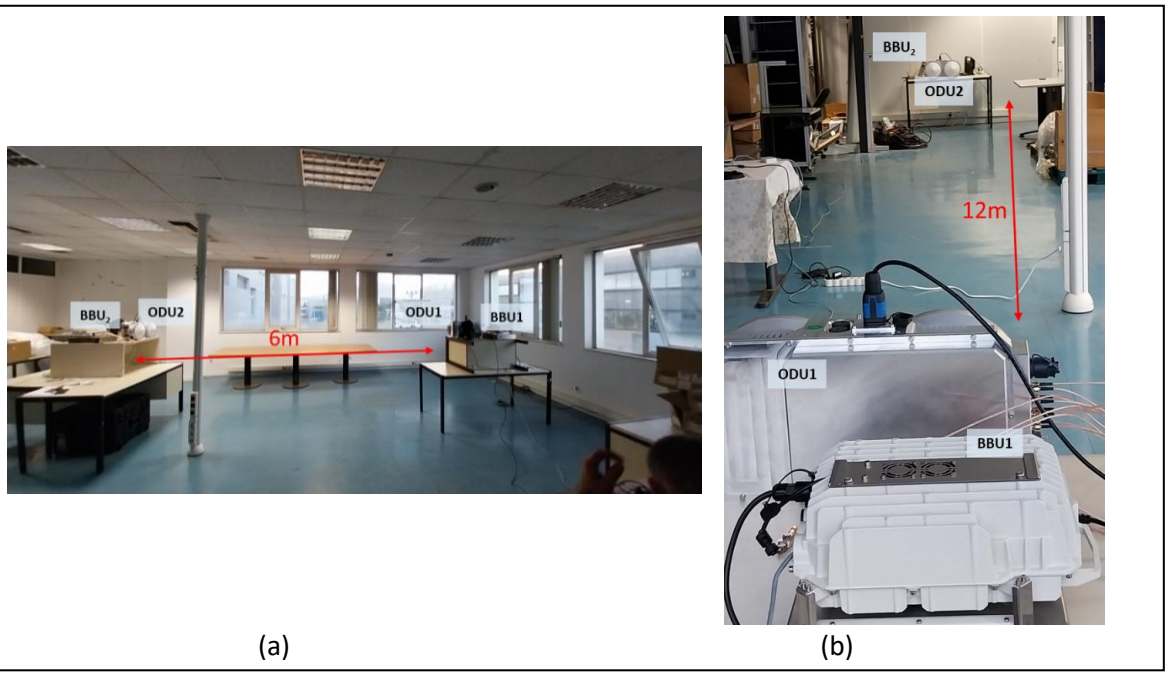

Figure 2-2: Indoor testing at distances of 6m and 12m

As we know, the radiation behaviour of antennas is characterized by their far-field radiation pattern. The far- field region of the antenna generally starts from the Fraunhofer distance $d=2D^2/\lambda$ from the antenna, with D the largest dimension (diameter in our case) of the antenna and λ the operating wavelength. In ARIADNE D-band demonstrator, as the RFU/antenna subsystem was designed for long-range outdoor use, the Cassegrain antennas with a diameter of about 21 cm, at the frequency of 150 GHz had a Fraunhofer limit at a radial distance of 45m, while at 160 GHz, the limit was about 50 m. In these (far-field) case, the antennas were designed for a ~51dBi gain. Given that, we have to appreciate that all indoor testing, taking place at a maximum distance of 12 m, was effectively performed within the near field of the antennas, justifying an observed gain 4-5 dB lower than the expected one, based on the power budget analysis for the far-field, in a long-range outdoor scenario. This had as a consequence a laborious alignment process and a degraded measured performance, compared to the expected long-range one, as reported in D5.2.

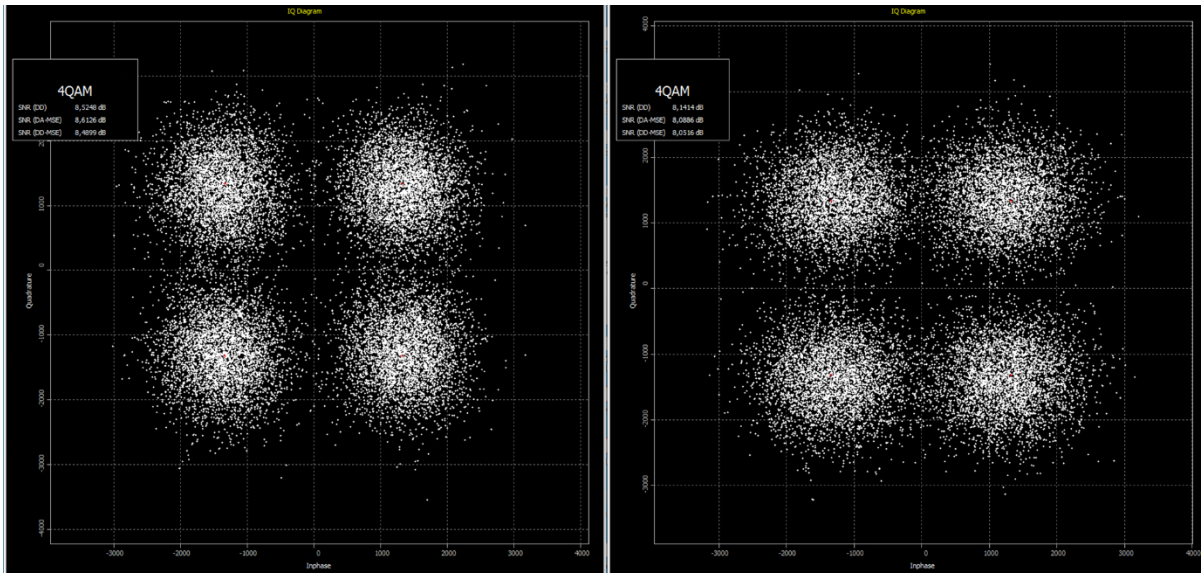

Figure 2-3: Constellation diagrams of the recovered 4-QAM symbols of the two modems of BBU_1 corresponding to each polarization: (a) horizontal and (b) vertical.

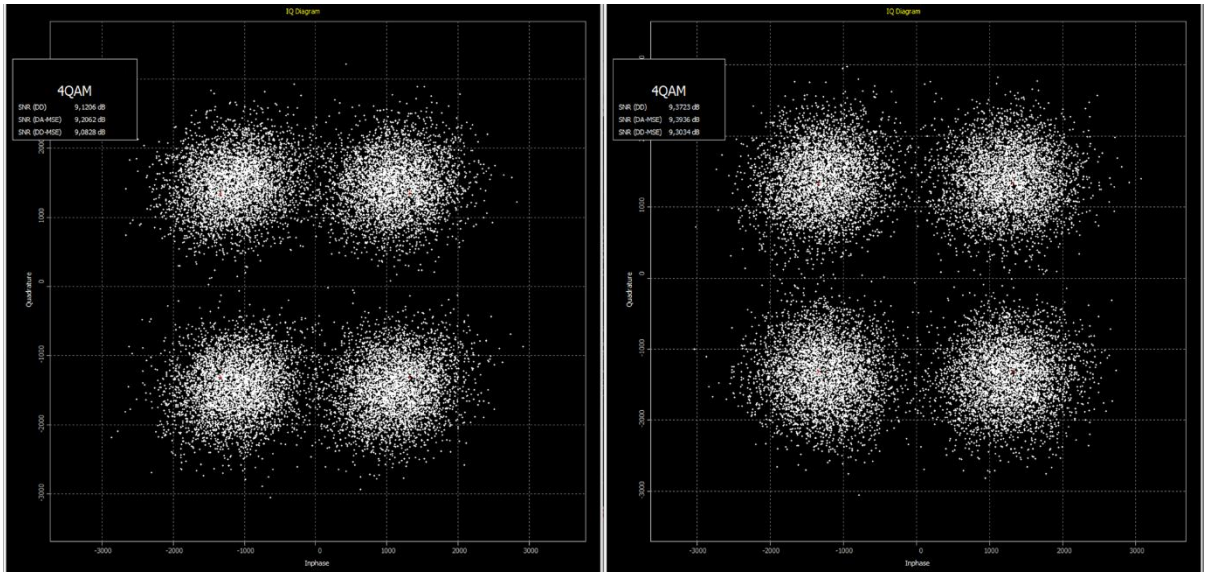

Figure 2-4: Constellation diagrams of the recovered 4-QAM symbols of the two modems of BBU_2 corresponding to each polarization: (a) horizontal and (b) vertical.

Figure 2-3 and Figure 2-4 show the respective constellation diagrams of the recovered QAM symbols (for both polarizations) after the compensation of the induced impairments, by the DSP functions of the BBUs.

After confirming the correct operation of the link at the physical layer, a streaming video test, using at the one side of the link a laptop with a video client and at the other side a laptop with a video server, was successfully performed, fully validating the link operation even at a lower SNR, as already explained (Figure 2-5).

Figure 2-5: Indoor link validation via streaming video test.

2.1.2 Outdoor Testbed

After completing the indoor testing, the units were moved to the rooftops of the A1 and A5 buildings of ICOM HQs. The poles at the two preassigned sites have been prepared to accommodate the BBU/RFU pairs. The distance between the two poles was measured to be approximately 226 m (Figure 2-6).

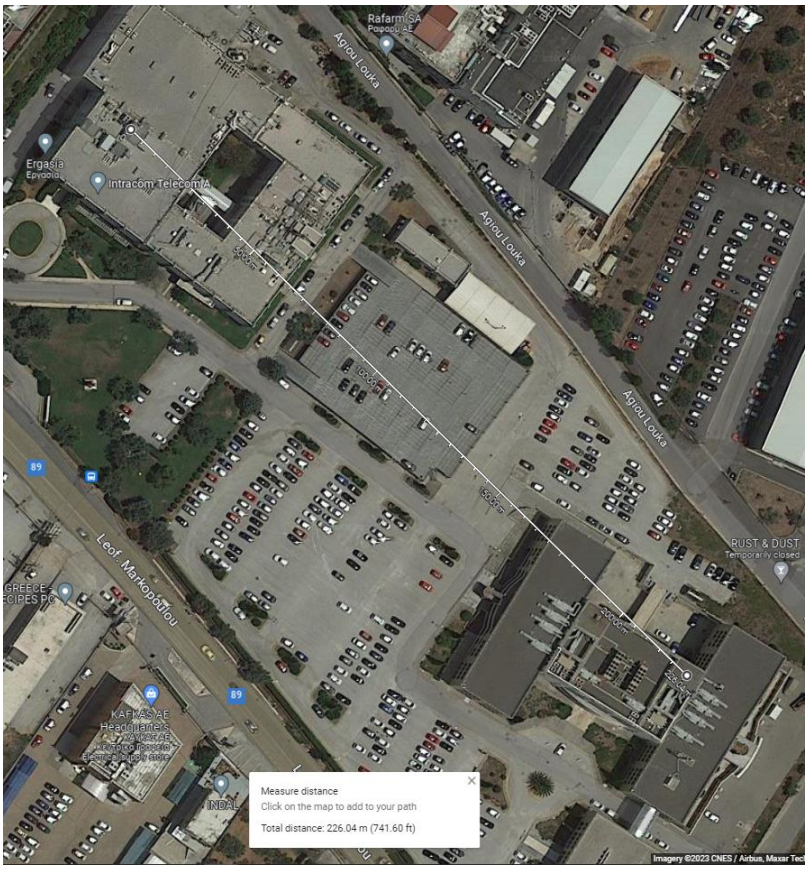

Figure 2-6: The 226 m link distance between the poles at the rooftops of the two buildings on ICOM premises.

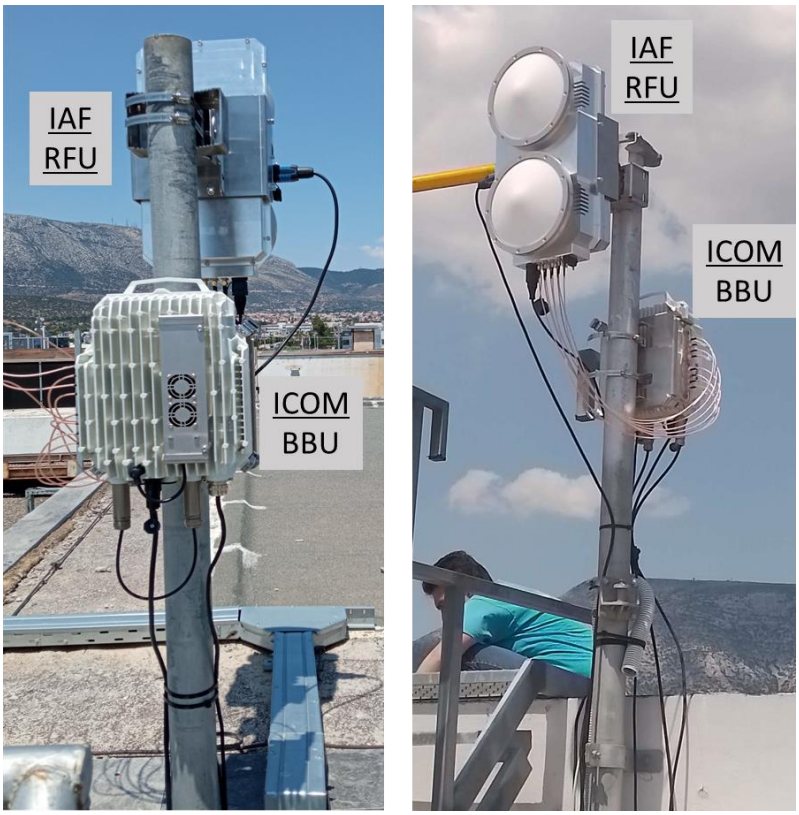

Figure 2-7: The two installed BBU/RFU pairs on the poles of the two buildings on ICOM premises.

Next, the link alignment process on both sides took place, using the mounting kits designed and manufactured by ICOM, for azimuth and elevation adjustment. Two instruments were used during the alignment process at each side: a spectrum analyser and an RF USB power meter were used in order to maximize the signal's power/quality as depicted in Figure 2-8 - Figure 2-11.

Figure 2-8: The spectrum analyzer used in the alignment process

Figure 2-9: The USB power meter used for the alignment process

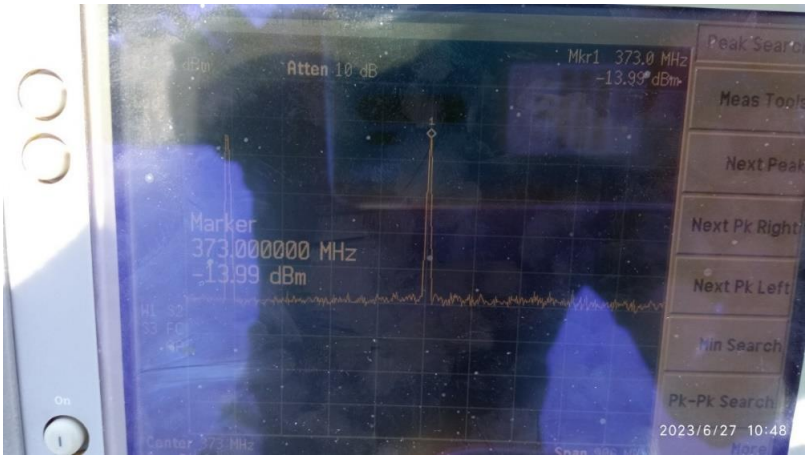

Figure 2-10: The spectrum analyser's screen used for the alignment process

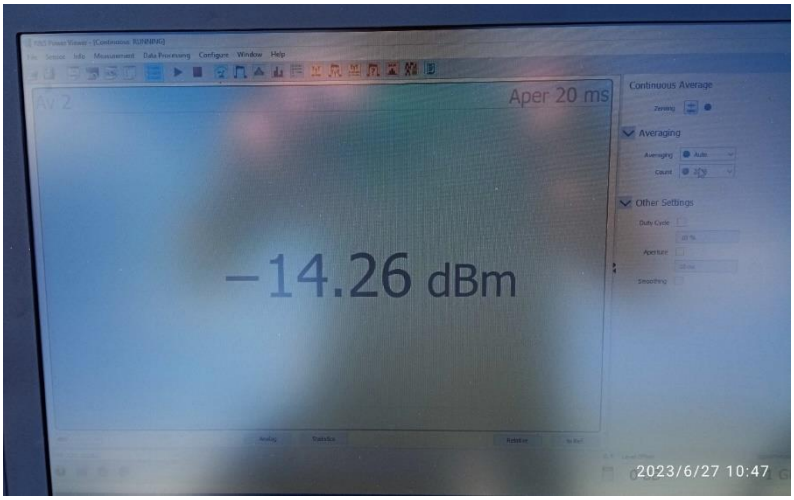

Figure 2-11: The GUI on the PC of the USB power meter showing the received RF power in dBm

After alignment, the maximization of the received power and the SNR was achieved, resulting in significantly higher figures compared to those in the indoor measurements.

2.2 Demonstration Scenario

The test scenario for the PtP D-band demonstrator, provided that optimum alignment has been achieved, consisted of the following stages (Figure 2-12):

1) Initiate the link by powering up first the RFUs and then the BBUs to avoid the risk of possible current flow into a switched-off RFU from a switched-on BBU.
2) Select a link direction to perform measurements, i.e. RFU1 to RFU2 or RFU2 to RFU1.
3) Initiate the devices at a specific pair of carrier frequencies (f_{TX}, f_{RX}) by running the Python script on the RFUs.
4) If error-free reception is achieved with the baseband units locked at the highest possible constellation, proceed with measurements, otherwise appropriately tune the parameters of the BBU and check reception.
5) Measure the received SNR while varying the transmit power.
6) When measurements are completed for this pair of frequencies, go back to step 3) to change the frequency to another pair in D-band and rerun SNR vs. Tx power measurements.
7) When measurements are completed for all pairs of frequencies, go back to 2) and reverse the link direction.
8) Repeat SNR vs. Tx power measurements for each frequency pair, executing steps 3) to 5).

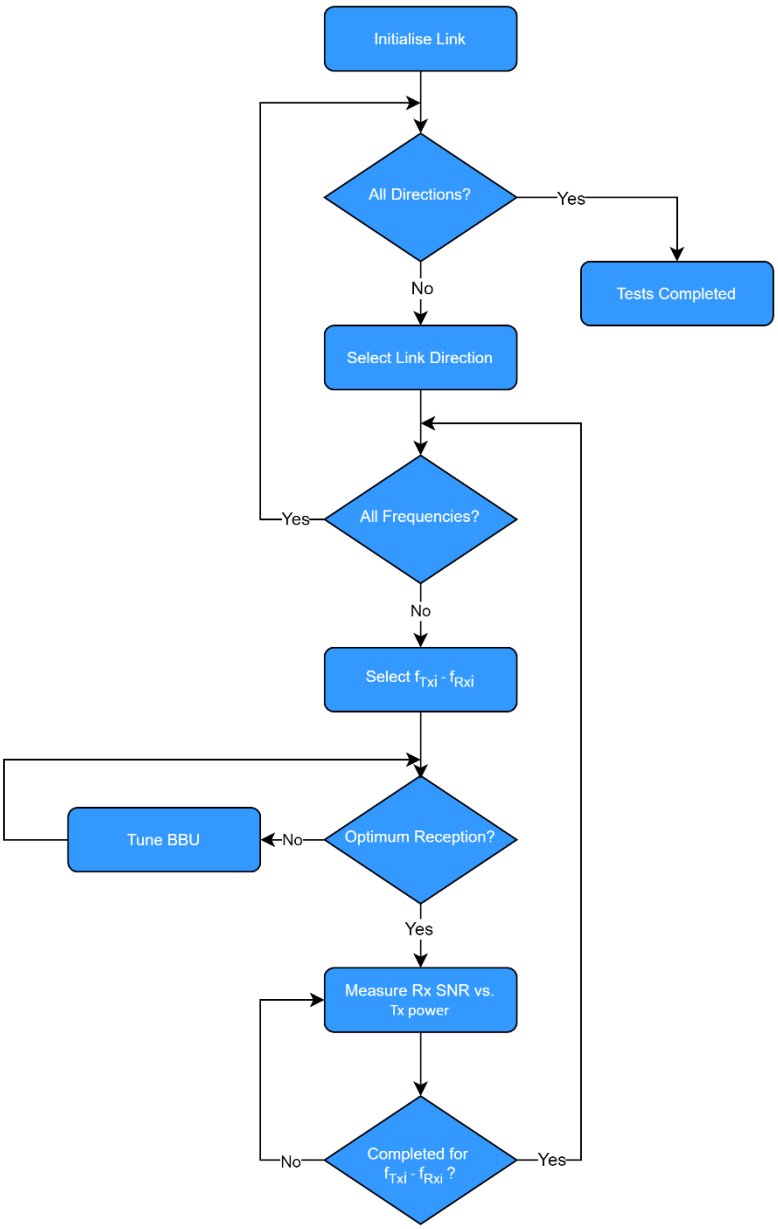

Figure 2-12: Test Plan Flowchart

2.3 Measurement and Results

The polarization-division multiplexing (PDM) is a physical layer method for multiplexing signals carried on electromagnetic waves, allowing two channels of information to be transmitted on the same carrier frequency by using waves of two orthogonal polarization states offering the doubling of the data rates. The dual polarization concept for transmission and reception in ARIADNE is based on the system topology as presented in the next figure and was reported in D3.4 [2].

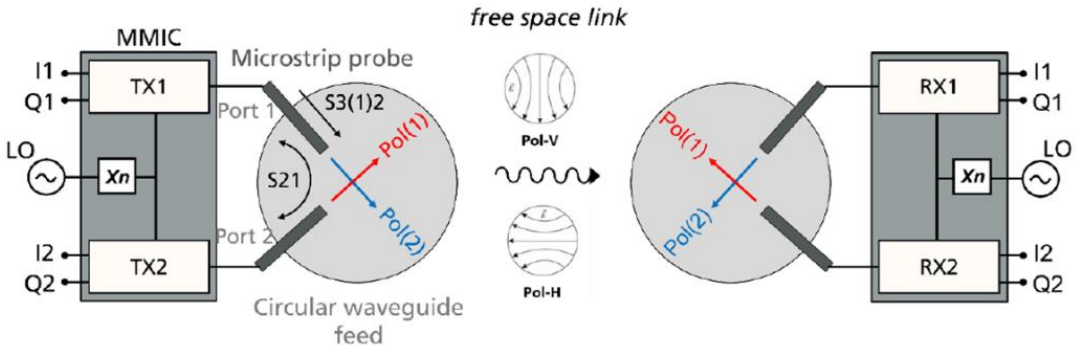

Figure 2-13: System topology for dual-polarization transmission/reception in ARIADNE [2]

Based on deliverable D3.4, the average output power of the manufactured Tx frontend modules, oscillates between around -25 dBm to -5 dBm in the frequency range 150 GHz to 160 GHz, which is the range supported by the RFU.

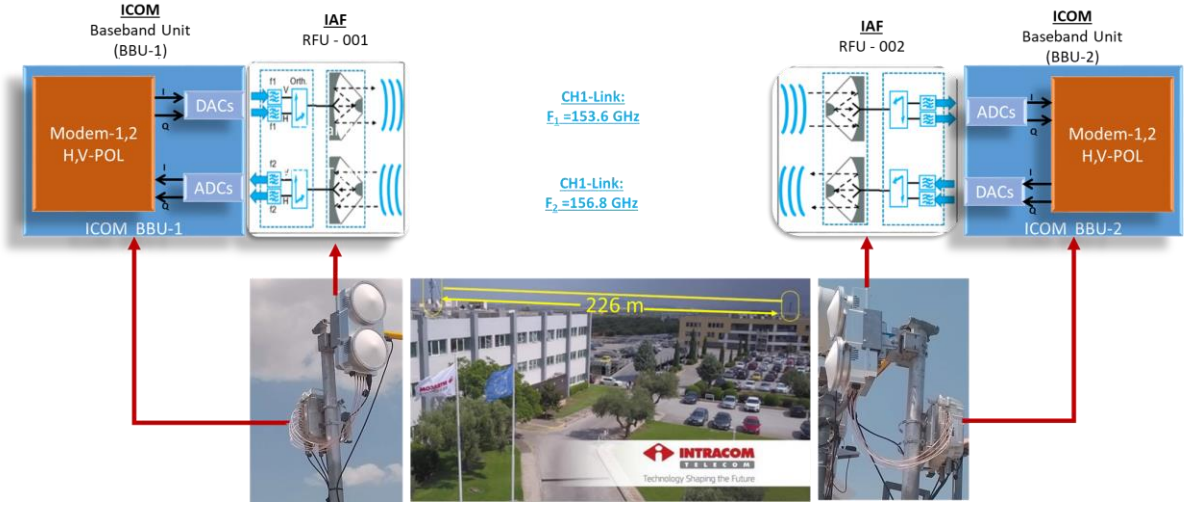

Figure 2-14: Block diagram of the outdoor experimental setup

Figure 2-14 shows the block diagram of the outdoor experimental setup while Table 2-1, shows the functional parameters and their values for this experiment.

Table 2-1: The functional parameters and their values

Parameters	Values
RF Frequency (for both directions)	[150 - 160] GHz
F_1 , F_2	153.6GHz, 156.8GHz
RF Tx output Power, Pout	[-25, -5] dBm
Antenna gain at (Tx & Rx), GTx, GRx	~ 51 dBi
I/Q input Power on Tx of RFU, P_IF	max: -5dBm
Conversion Gain of RFU, RX_CG	~ 25
Constellation size M-QAM	[4 – 1024]

Link distance, D_1	226m
FSPL (@F_1, @D_1)	122.5dB

In the first set of measurements, two carrier frequencies F_1 = 153.6GHz and F_2 = 156.8GHz were selected. The transmitted power from the BBUs as input to the IAF RFUs was selected to be about P_IF = -22dBm. For the F_1 carrier frequency the free space path losses (FSPL) [1, 2] are about 123.25dB as depicted in Figure 2-15. The received power, PRx is calculated based on the next equation using the values of Table 2-1 :

$$PR_x = \text{Pout} + \text{GTx} - \text{FSPL}(@153.6\text{GHz}, @226\text{m}) + \text{GRx} + Rx\_CG \cong -18.25\ dBm$$

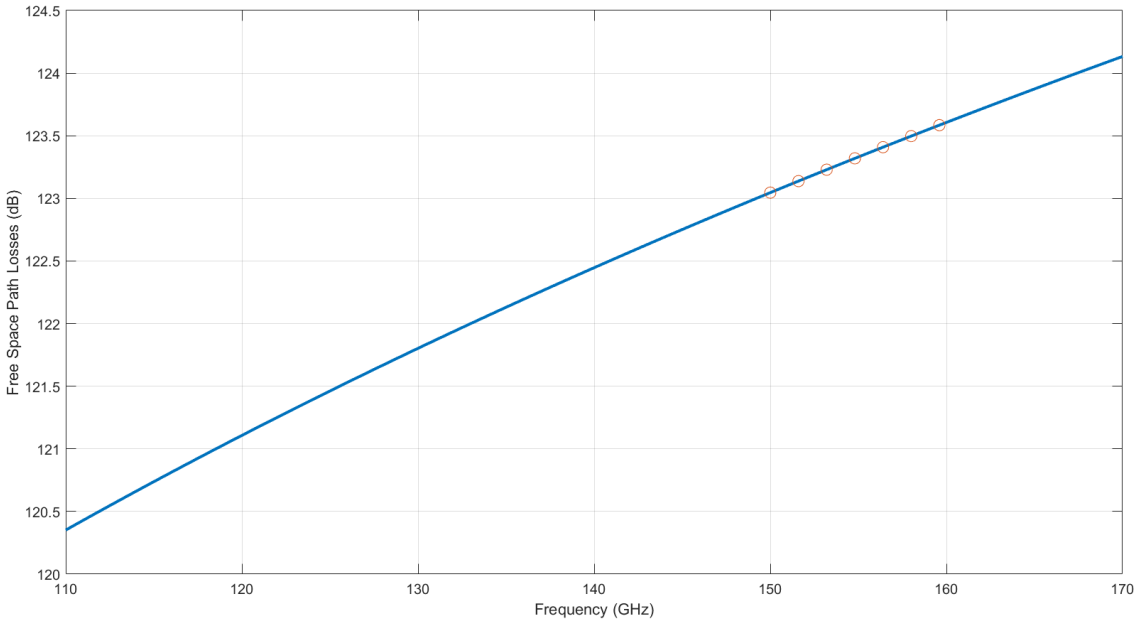

Figure 2-15: Free space path loss in the frequency range 150 to 160GHz based on Friis transmission formula [1, 2]

Next, for this received power, the BBU at the Rx side should compensate all the induced impairments and recover the down-converted and distorted QAM symbols. Figure 2-16 shows the histogram distribution of the received power of the BBU input for the two modems.

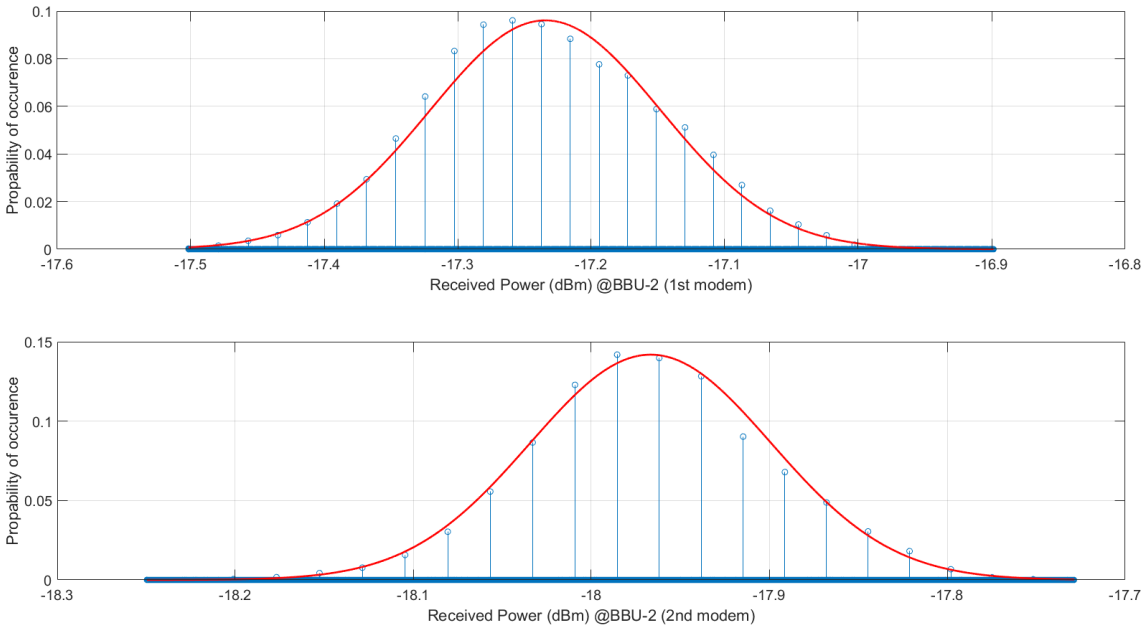

Figure 2-16: Histogram distribution of the received power in both modems of BBU-2

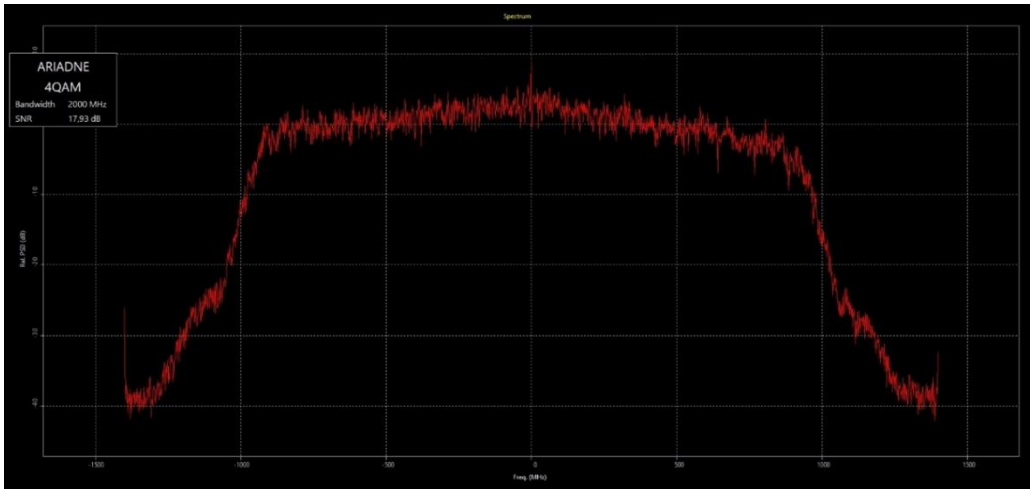

Figure 2-17: Power spectrum magnitude of the received QAM signals in the 1st modem of the BBU-1

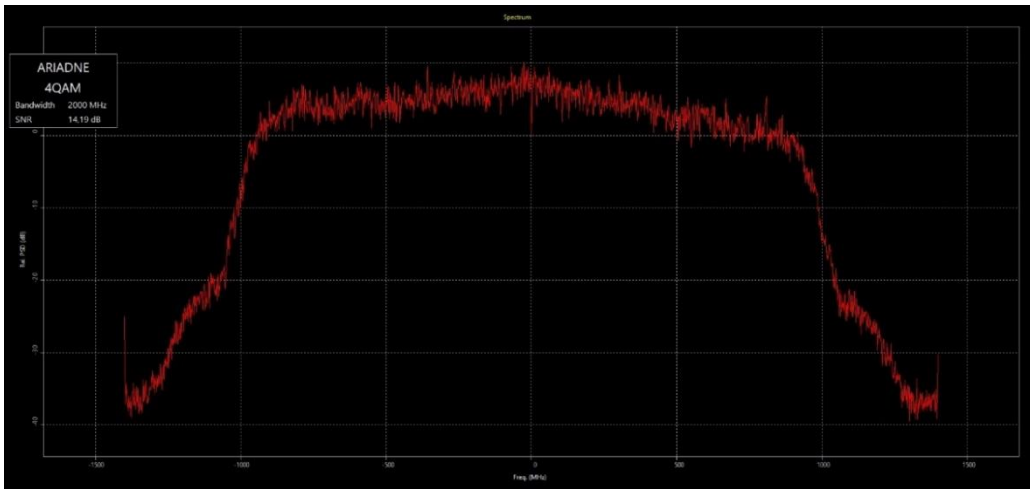

Figure 2-18: Power spectrum magnitude of the received QAM signals in the 2nd modem of the BBU-1

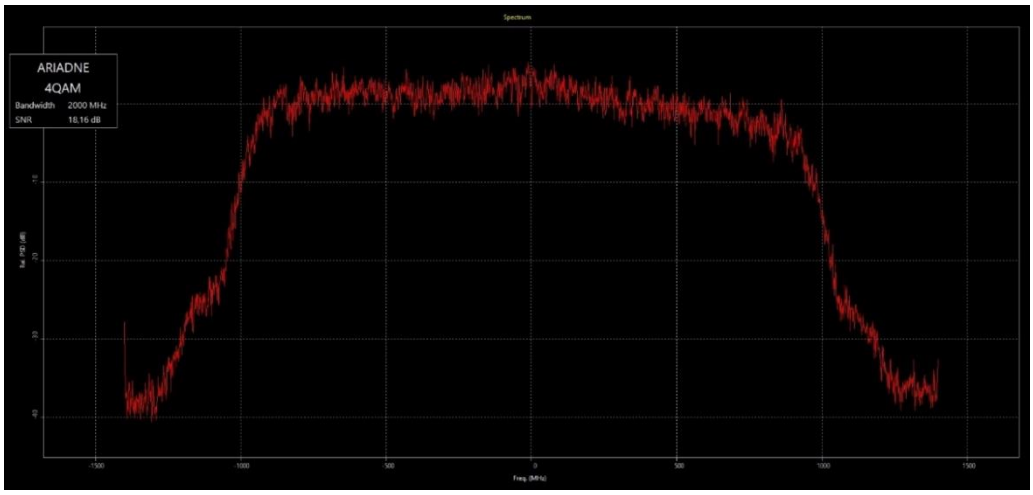

Figure 2-19: Power spectrum magnitude of the received QAM signals in the 1st modem of the BBU-2

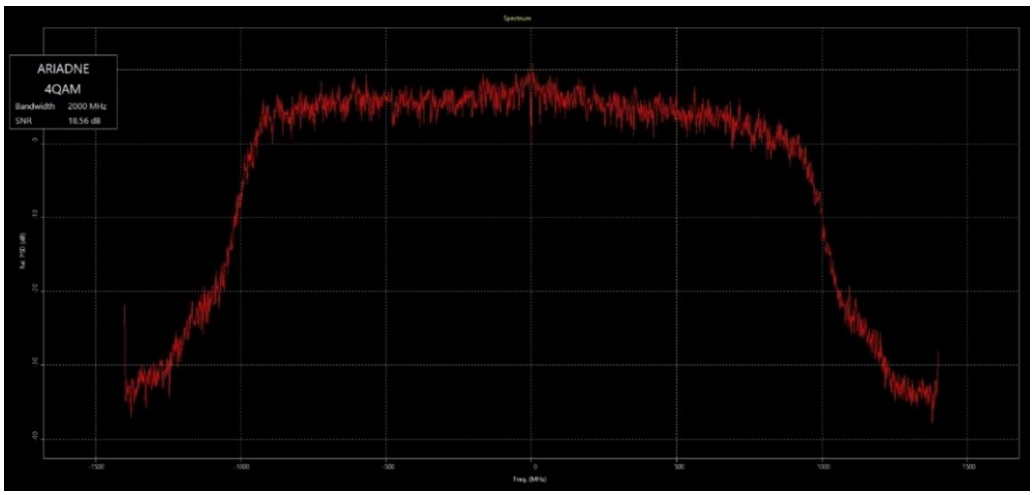

Figure 2-20: Power spectrum magnitude of the received QAM signals in the 2nd modem of the BBU-2

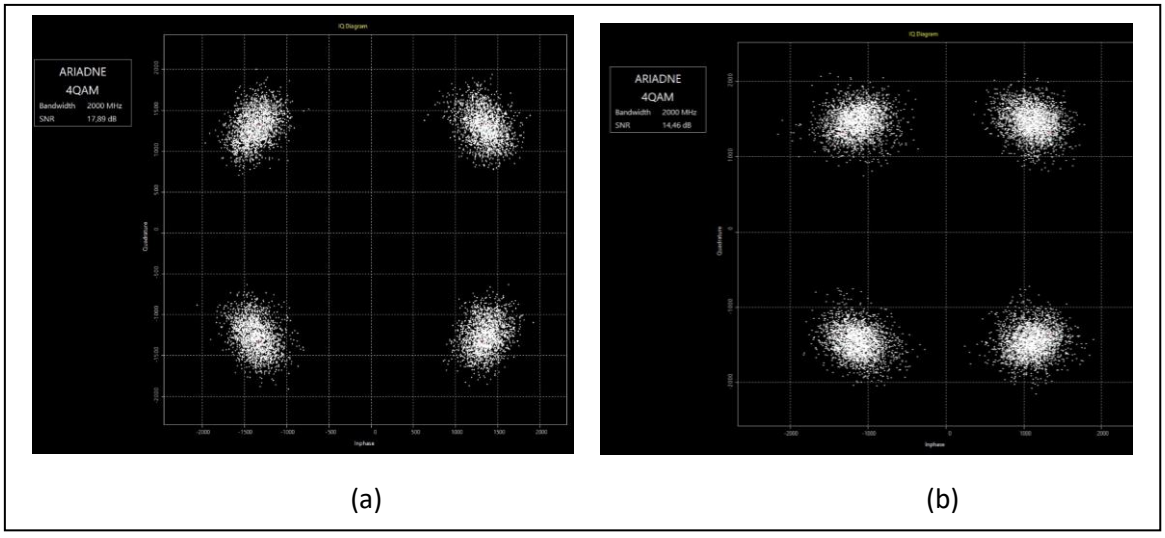

Figure 2-21: Constellation diagrams of the recovered QAM signals of the two modems of the BBU-1

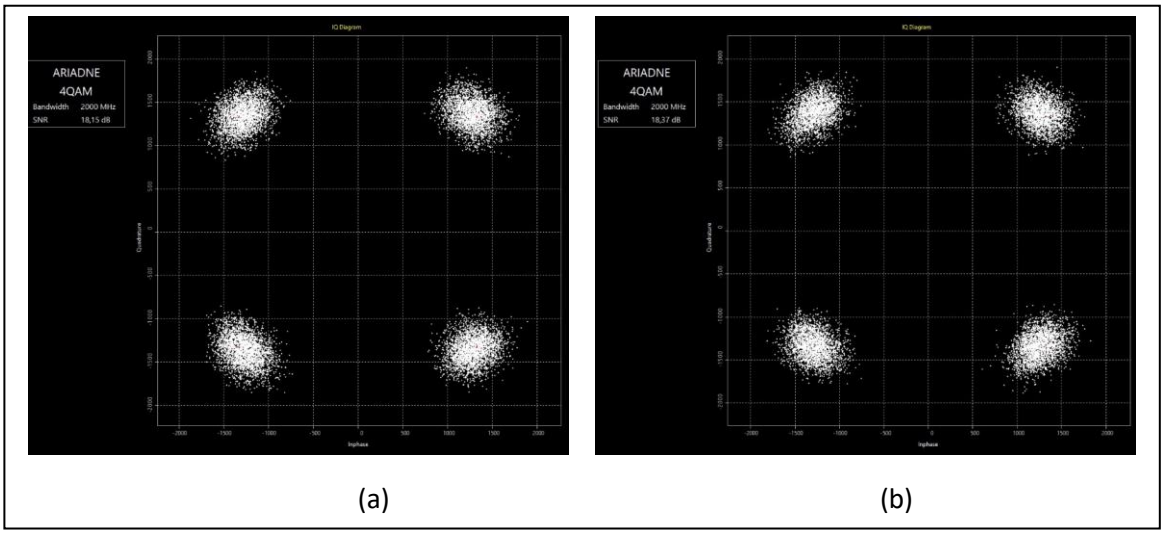

Figure 2-22: Constellation diagrams of the recovered QAM signals of the two modems of the BBU-2

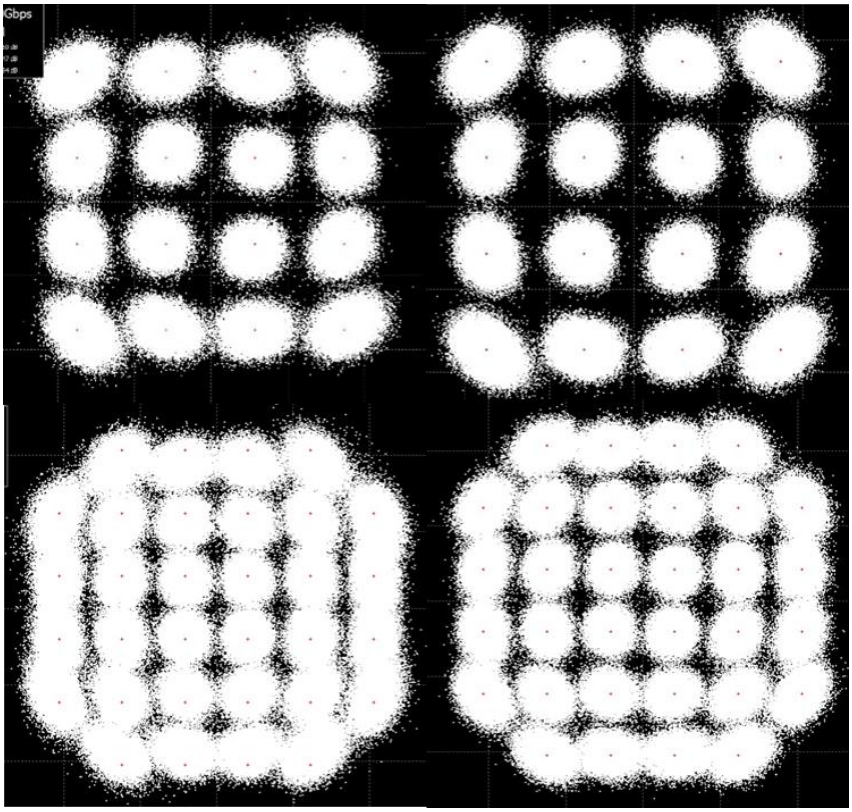

Figure 2-23: Constellation diagrams of the recovered QAM signals for the case of 16- and 32-QAM

Figure 2-17 - Figure 2-20 show the power magnitude spectra of the received QAM signals at the inputs of the two BBUs while Figure 2-21 and Figure 2-22 show the respective constellation diagrams of the compensated and recovered QAM symbols.

Similar results can be obtained changing the modulation size from 4-QAM to 16- and 32-QAM as presented in Figure 2-23. The achievable data rate in these three cases are 5.2Gbps, 10.4Gbps and 13.060Gbps.

At the receiver side of each BBU, an XPIC algorithm is running to suppress the mutual interference between the two received streams which are polarization multiplexed. The BBU estimates the cross-polarization discrimination (XPD) in dB as depicted in Figure 2-24 where the measurements and the histogram of the estimated XPD from both modems of the BBU are depicted. As can be derived from this figure, the estimated XPD in the 1st modem is about 25.3dB while in the 2nd modem, the XPD is about 22.0 dB.

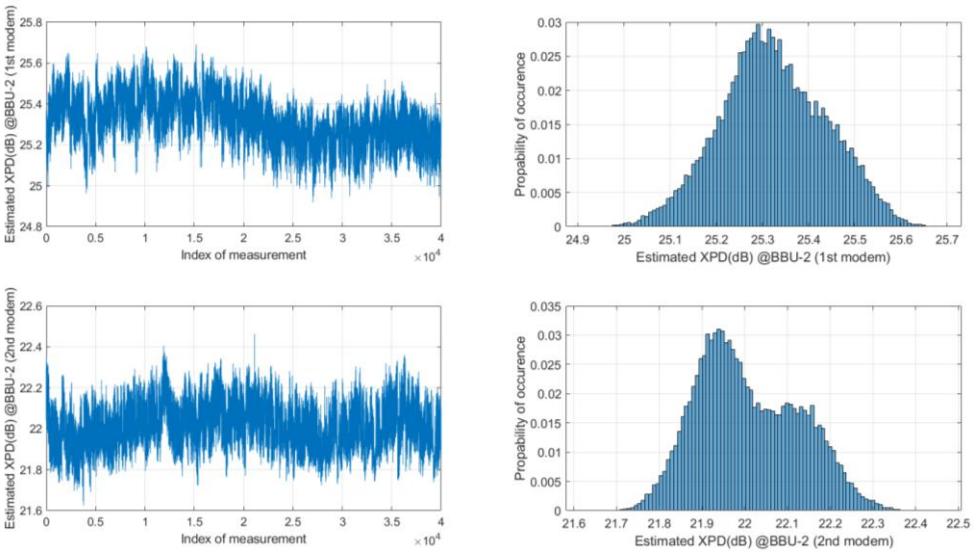

Figure 2-24 : Time traces and histogram distributions of the estimated XPD (dB) based on XPIC algorithm

In order to investigate the performance of the link, we tuned the RF transmitted power of the RFU-1/BBU-1 and we measured the bit error rate (BER) and the respective SNR (dB) on the 1st modem of the other BBU (BBU-2) as presented in Figure 2-25. As can be observed from this figure, as the Tx power and the SNR at the Rx side of the BBU are reduced, the BER is also reduced.

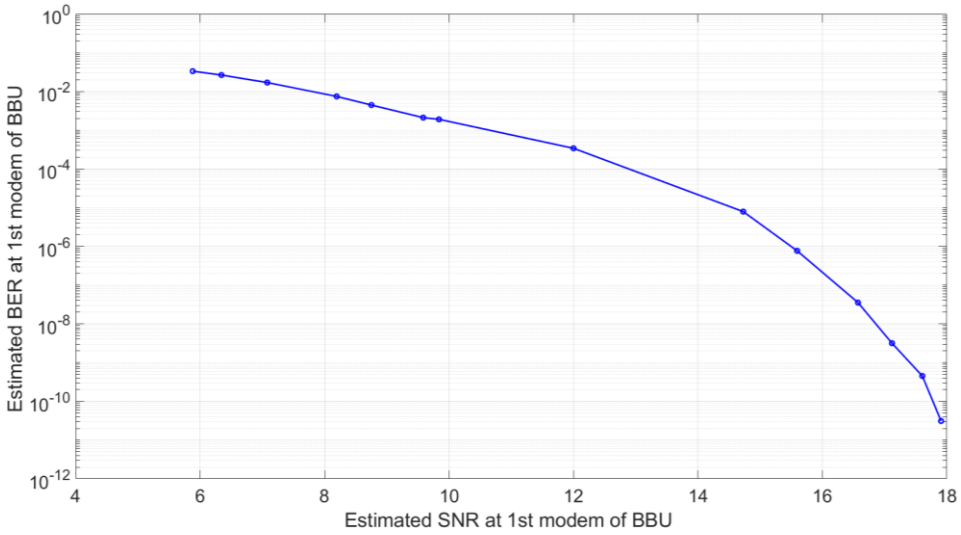

Figure 2-25: Estimated BER vs. estimated SNR (dB)

Next, we performed a new round of measurements to estimate the link path losses, where the carrier frequency F_1 was varied in the range of 150.4GHz up to 158.4GHz with a step of 1.6GHz and the carrier frequency F_2 was selected to be 160GHz. At the receiver part of the first link (BBU-2), we measured the

received power (at IF level) and based on the known transmitted power of the BBU-1 and RFU-1 we estimated the path losses of the link as depicted in Figure 2-26. In the 1st graph of this figure, we can see the free-space path losses (blue line) based on Friis formula versus the operating carrier frequency in the range of 150GHz up to 160GHz and the estimated losses in dB of D-band link including also the frequency dependence of the RFUs' transmitted, received power and conversion gains.

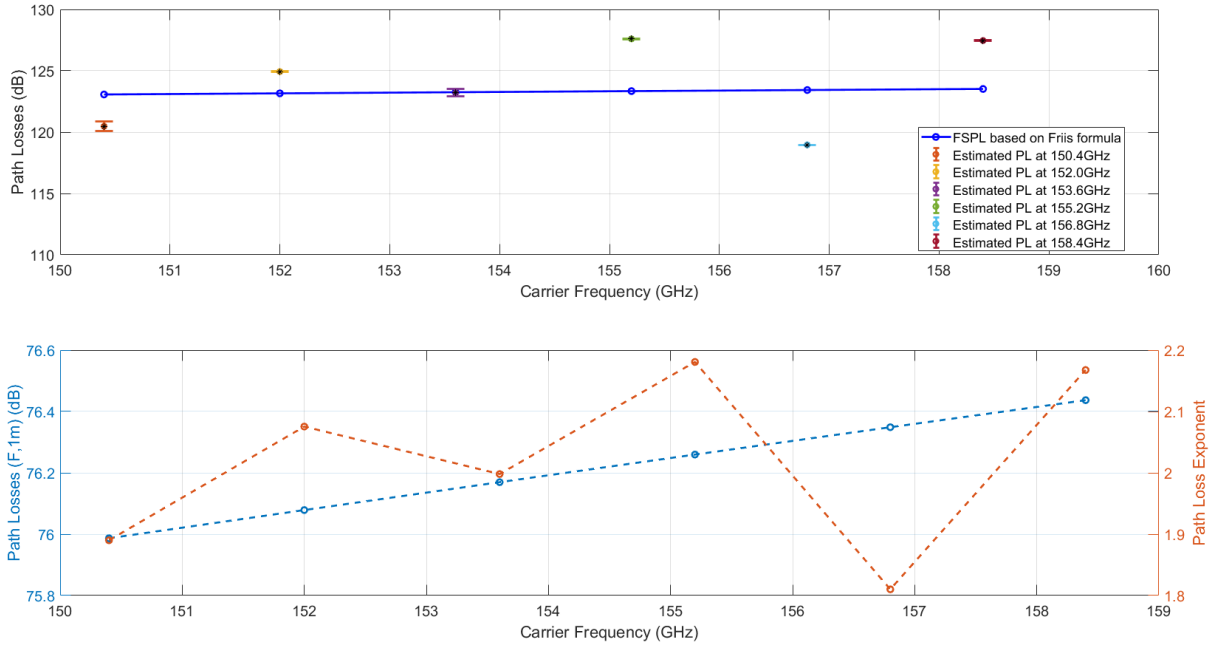

Figure 2-26 : (a) The free space path losses based on Friis formula versus the operating carrier frequency in the range of 150GHz up to 160GHz and the estimated losses in dB of D-band link, and (b) the estimated path losses (F, 1m) and path loss exponent versus the operating carrier frequency

The path losses in the real world are highly dependent on the transmission environments while the FSPL model based on the Friis formula is not accurate enough to describe the actual propagation characteristics [1, 2]. Based on the literature, there are many different path loss models to characterize the power attenuation during propagation, such as the Floating Intercept (FI) and the Close-In (CI) models [1, 2].

The CI model is a simplified path loss model with low complexity and the most frequently used model predicting the signal strength over distances for various frequencies [1]:

$$PL^{CI}(f,d) = FSPL\ (f,d_0) + 10\ \beta\ log_{10}\left(\frac{d}{d_0}\right) +\ X_\sigma^{CI}, d\ >\ d_0$$

where FSPL is the free space path loss at carrier frequency f with d0 = 1m; d_0 is a reference distance; β is the path loss exponent that characterizes the dependence of path loss on d; and X_σ^{CI} is the large-scale shadow fading that can be modelled as a zero-mean Gaussian distributed random variable with standard deviation σ (in dB). The CI model has only one variable (β), which can be obtained by the least squares linear fitting method, that is, fitting the measurement data with the smallest error.

Considering as d_0 = 1m and $FSPL\ (f,d_0)$ based on Friis formula and as $PL^{CI}(f,d)$ the measured loss data, we can use the above equation to find the path loss exponent β for different frequencies as presented in the 2nd graph (red dashed line) of Figure 2-26. In the same graph with a blue dashed line is presented the FSPL for different frequencies for the reference distance d_0 = 1m. As it is observed from this graph, the estimated values of path loss exponent β are around the theoretical free-space

path loss exponent of 2. Many factors can lead to instability in measurement campaigns. Firstly, the path loss exponent of the test band is extremely sensitive to scatter differences in the measurement environment; specifically, outdoor open environments with ground, trees, and smooth tiles will produce abundant reflections, leading to multipath fading. Furthermore, the strong directionality of mmWave beams can also create device alignment problems, especially when the distance is set at 200m and more [1].

The sample performance was first experimentally tested at Aalto university by measuring the reflection coefficients at focused-beam illumination. The setup and measured data are shown in Figure 3-2. The results confirm the desired performance as anomalous reflectors of waves coming from 50-degree direction to waves in the normal direction, as required for the indoor link demonstrator

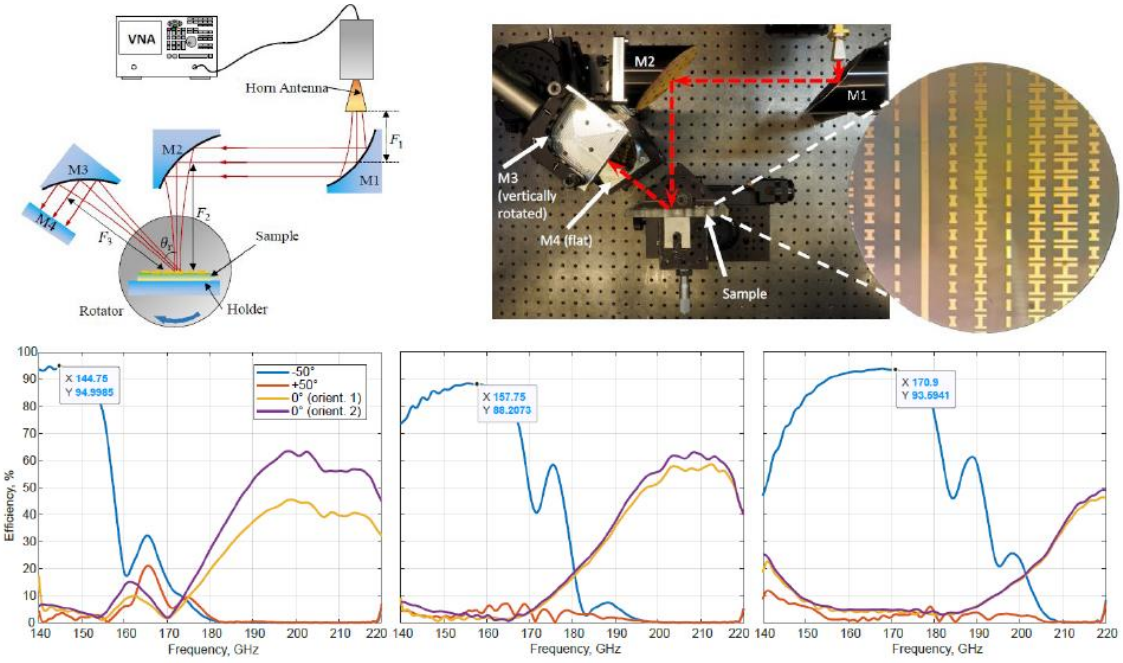

Figure 2-27: Experimental setup for testing reflection coefficients. The values of Y are the experimentally achieved efficiencies of anomalous reflection at the three operational frequencies

These preparatory actions and results are described in detail in deliverables of WP 3. The main results have been also published [5].

3 Demonstrator 2: A Metasurface-enabled point-to-point NLoS link

3.1 Test-bed Description

This demonstrator was realized using D-band anomalous reflectors developed by WP3. Here, we include a short description of the surfaces. Figure 3-1 shows the geometry of one of the designed patch arrays and simulated efficiencies at the three operational frequencies.

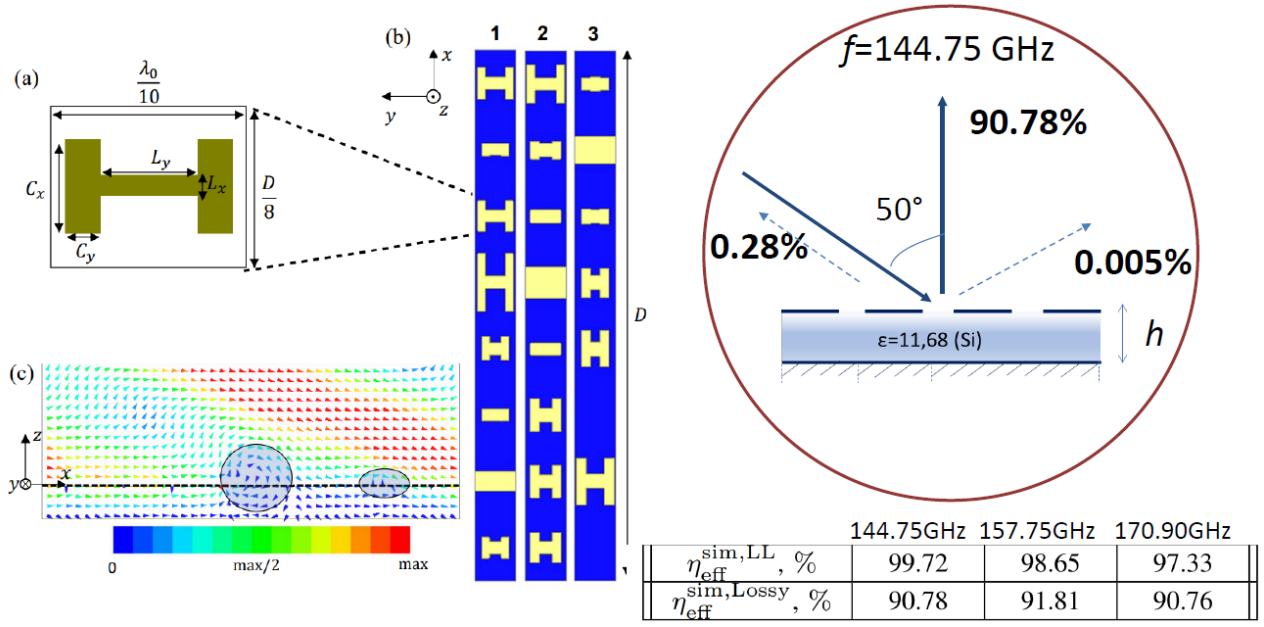

	144.75GHz	157.75GHz	170.90GHz
$\eta_{\text{eff}}^{\text{sim,LL}}$, %	99.72	98.65	97.33
$\eta_{\text{eff}}^{\text{sim,Lossy}}$, %	90.78	91.81	90.76

Figure 3-1: Metasurface geometry and simulated efficiency of anomalous reflection ("LL" - lossless model, "Lossy" - simulations include the effects of dissipation)

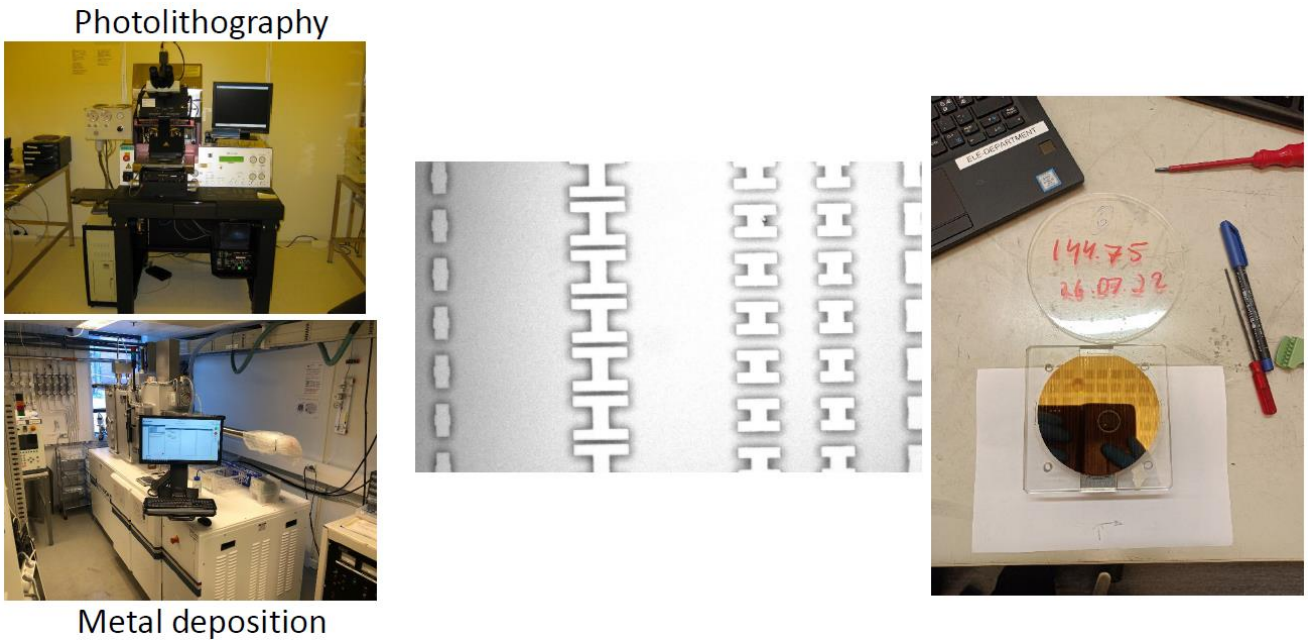

Figure 3-2: Sample manufacturing (Aalto University facilities)

3.2 Demonstration Scenario

The demonstration scenario is illustrated in Figure 3-3:

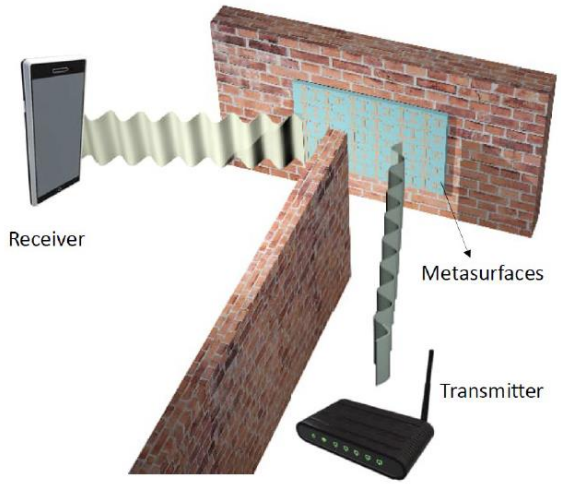

- Frequency range of interest: 144-170 GHz
- We design and test anomalously reflecting metasurfaces that reflect beams arriving at an oblique angle (50°) into the shadow in the direction normal to the wall.

Figure 3-3: Demonstrator scenario: delivering a D-band signal into the shadow of a wall via reflections in an anomalously reflecting metasurface

The main geometrical parameters, especially the reflector size needed to ensure the required signal level at the receiver position, were estimated using the developed simple analytical model of link budget for links via anomalous reflectors. That model was presented in earlier deliverable and also published in [4].

3.3 Realization of dielectric lens antennas

For the final demonstration of the MTS-enabled PtP NLoS demonstrator, which has been shown at the 2023 EuCNC in Gothenburg, Sweden, it was planned to have the ability to combine all the existing ARIADNE D-band hardware of WP3 into a single demonstrator. Hence, the ARIADNE Tx & Rx RF modules also used in the RFUs of demonstrator 1, need to work in a short-range indoor environment in combination with a specific medium-gain antenna. It becomes clear that this kind of scenario will not work in conjunction with the presented Cassegrain antennas of demonstrator 1 due to the high far-field distance. Thus, a high-performance design and manufacturing of easily adaptable antenna structures meeting the demonstrator requirements is necessary, which is fulfilled by using presented medium-gain dielectric lens-antenna structures.

3.3.1 Dielectric lens antennas final design and prototyping

Based on our previous work presented on Deliverable D3.3 and D5.2, an elliptical dielectric lens antenna design has been proposed as a solution for the indoor communication scenario and though demonstrator 2. As described in D5.2 the initial theoretical lens model has been evolved in terms of geometry so as to meet with IAF's RF-frontend specifications and fabrication requirements. Before proceeding to final designs, a sensitivity analysis has been carried out using the theoretical model. It is assumed that the conclusions from this analysis results will be valid for the case of the final designs.

3.3.1.1 Sensitivity analysis towards lens antennas final design

The analysis was based on lens antennas radiation performance using a parametric simulation in terms of mechanical misalignment of the lens regarding the feed horn position. This analysis is critical regarding the prototyping and assembling procedure, as such discrepancies could occur. The

misalignment concept can be seen in Figure 3-4. The misalignment has been examined along x and y axis (Δx, Δy).

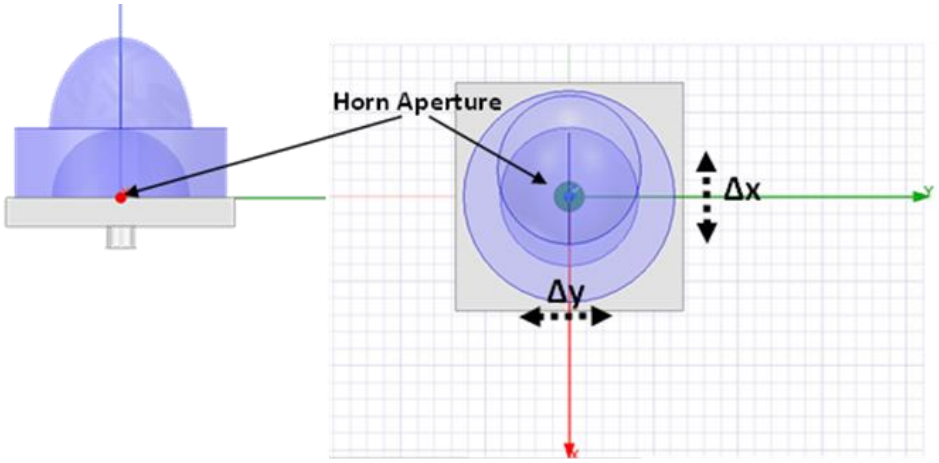

Figure 3-4: Lens misalignment to horn position (lens antenna side view and top view)

The contour gain plots for four out of nine parametric cases examined are depicted in Figure 3-5. The shift of the main radiation spot can be clearly seen due to the misaligned lens compared to the ideal case (Δx=0mm, Δy=0mm). More specifically the maximum achieved gain values at the desired theta angle of all examined cases can be seen in Table 3-1. Gain degrades compared to ideal case by a maximum of 3 dB. However, it should be noted that the misaligned cases yield similar high gain as the ideal case but at other (non-desired) theta angles. The effect of lens displacement is visualized in Figure 3-5 using contour radiation patterns. It is noticed that the max gain angle shift follows the direction of misalignment of the lens. The dash line perpendicular to the theta axis shows the displacement of the maximum gain value compared to the ideal case (a) where no misalignment is considered.

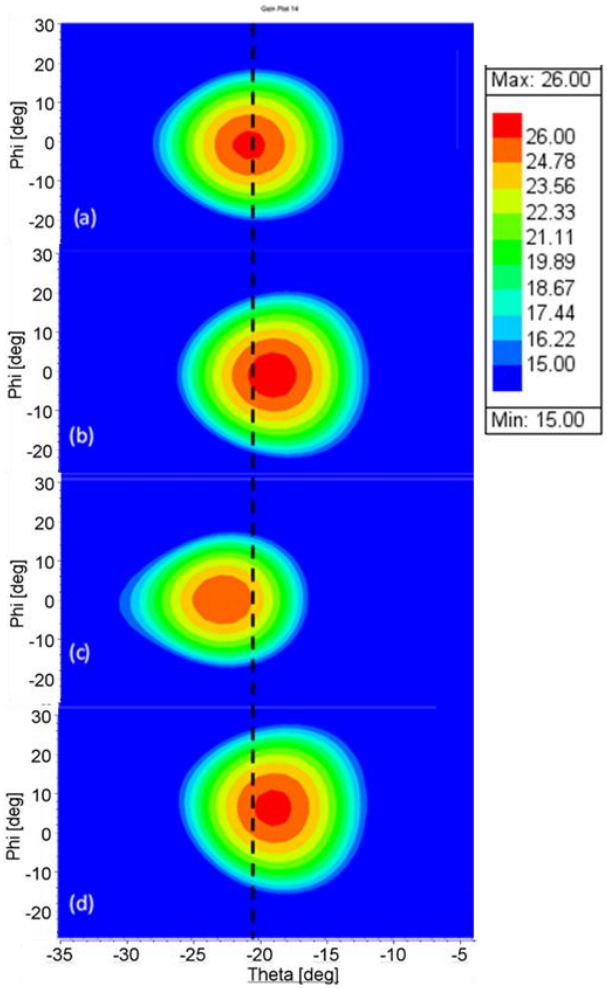

Figure 3-5: Contour plots of gain radiation patterns for various misalignment cases (Δx, Δy): (a) (0mm, 0mm), (b) (0.5mm, 0mm), (c) (-0.5mm,0mm), (d) (0.5mm,-0.5mm).

Δy	-0.5 mm	0 mm	0.5 mm
Δx	**Gain [dBi]**		
-0.5 mm	**23.23**	**24.75**	**24.33**
0 mm	**24.90**	**26.32**	**26.02**
0.5 mm	**24.93**	**26.27**	**25.78**

Table 3-1: Gain variation for misalignment cases (Δx, Δy) at theta=-20.5 deg

3.3.1.2 Detailed design of lens antennas and feed-package

Based on the lens antenna analysis described in D3.3, the elliptical lens and the feed horn package with manufacturing details (waveguide flange, screws, alignment pins etc.) have been designed as shown in Figure 3-6a. After discussions between IAF and NCSRD the proposed lens detailed design has been evolved in the design presented in Figure 3-6b. Main reason for this is the facilitation of the manufacturing of the lenses. Also, it has been concluded that the materials to be used for the manufacturing and though for the design of the whole antenna system are HDPE dielectric (εr=2.3, tanδ=0.0005) for the lenses and Brass Gold Plated for the feed horn package. However, at final fabrication the package has been implemented with aluminum material. It is assumed that no significant differences are occurred since EM properties of both conductive materials are very close (σ_{Brass}=1.59*10^{7}S/m, $\sigma_{Aluminum}$=3.5*10^7 S/m).

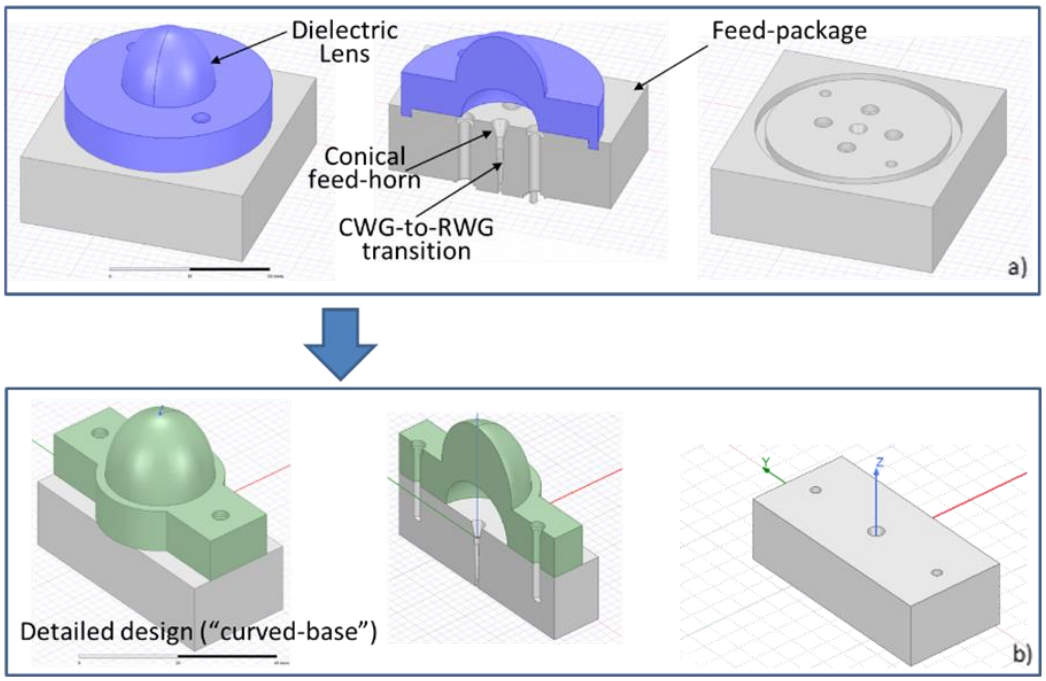

Figure 3-6: Evolution of the design of lens with the feed horn package

The final schematics of NCSRD designed lenses, based on the above evolution, are presented in Figure 3-7 for four different lenses. More specifically, for 0° tilt angle three lenses have been designed with three different Focal Lengths (15mm, 20mm, 25mm). This was done in order to have a series of lenses with different achieved gain values but all of them with gain larger than 25dBi. Lenses with different focal lengths can be used for different indoor scenario distances. For tilt angle 20° one lens with F=25mm has been designed aiming for a gain of at least 27dBi. Titled angle lens can be used to avoid manual rotation of the lens antenna itself (by paying a small reduction in gain). All lenses should use the same feed horn package as they can be easily assembled and disassembled on it.

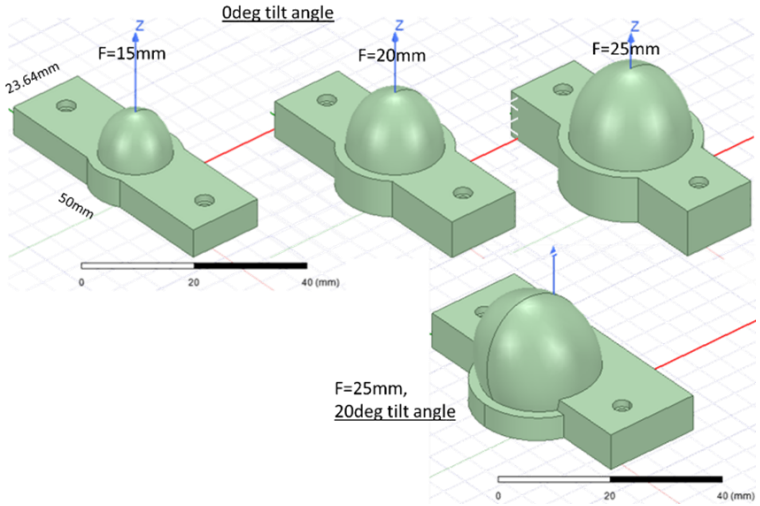

Figure 3-7: Three 0deg-tilt lenses for various F (15mm, 20mm, 25mm) and 20deg-titled lens with F=25mm

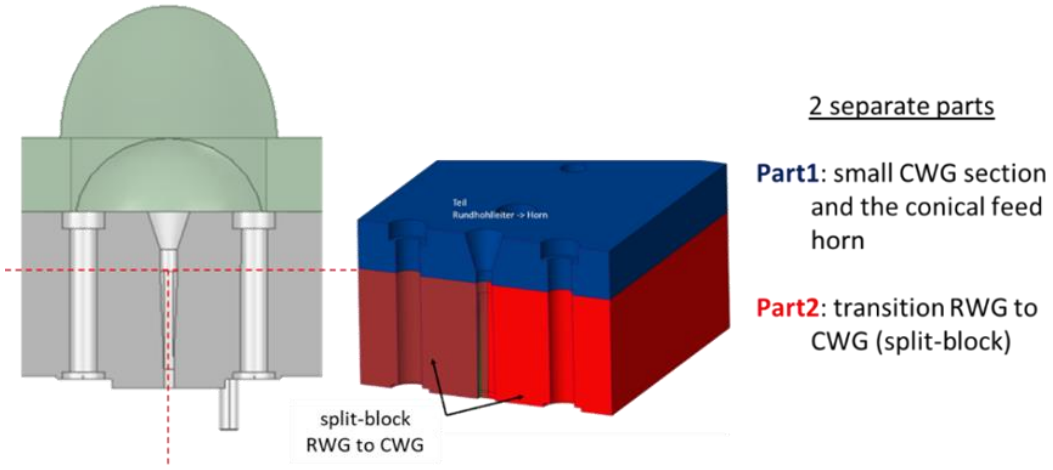

Figure 3-8: Feed horn package and CWG-to-RWG transition

The main reason for adding to the feed-package design the rectangular to circular waveguide transition part (RWG-to-CWG) is to be compatible with IAF's measurement facilities connectors. Moreover, the way the feedhorn package is designed and fabricated offers two different feed capabilities. One with circular waveguide (G-low), compatible with IAF RF-frontend, and one with rectangular waveguide (WR-06) compatible with IAF measurement system. In Figure 3-8 shows the feedhorn package constructed with different parts. The blue contains the circular waveguide (CWG) and the red one the rectangular one (RWG), while both parts are aligned and connected with screws. This split-block package offers the possibility of multi-purpose usage. The schematic of the feed horn with the RWG-to-CWG transition can be seen in Figure 3-9a. These dimensions have concluded after optimization carried out by using HFSS and aiming to achieve best reflection coefficient (S11) performance within the D-band.

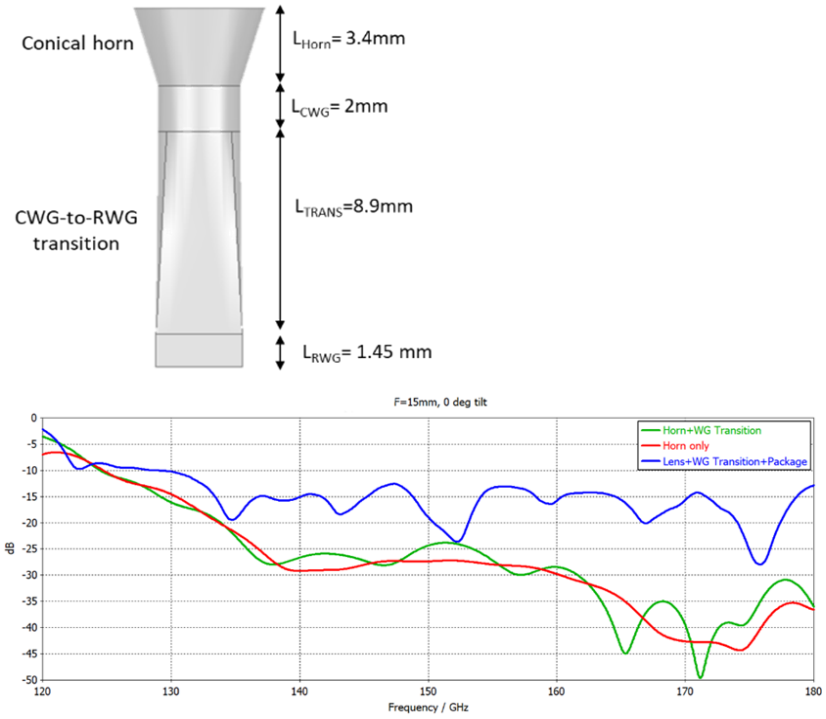

Figure 3-9: a) Horn with CWG-to-RWG transition, b) S11 performance

Additionally, a comparison in terms of S11 for the circular horn, the CWG-to-RWG transition with horn and for the whole antenna system (feed horn package and lens embedded above) is presented in Figure 6b. The radiation pattern of the feed horn can be seen in Figure 3-10. Compared to the standalone feed horn antenna under the lens, the feed horn package effect has been examined. Indicatively in Figure 3-11 the radiation pattern of the detailed Lens (F=15mm) for the cases -with and -without package is presented. It can be seen that the effect of the horn package is stronger at the side lobes and not affecting the main lobe significantly.

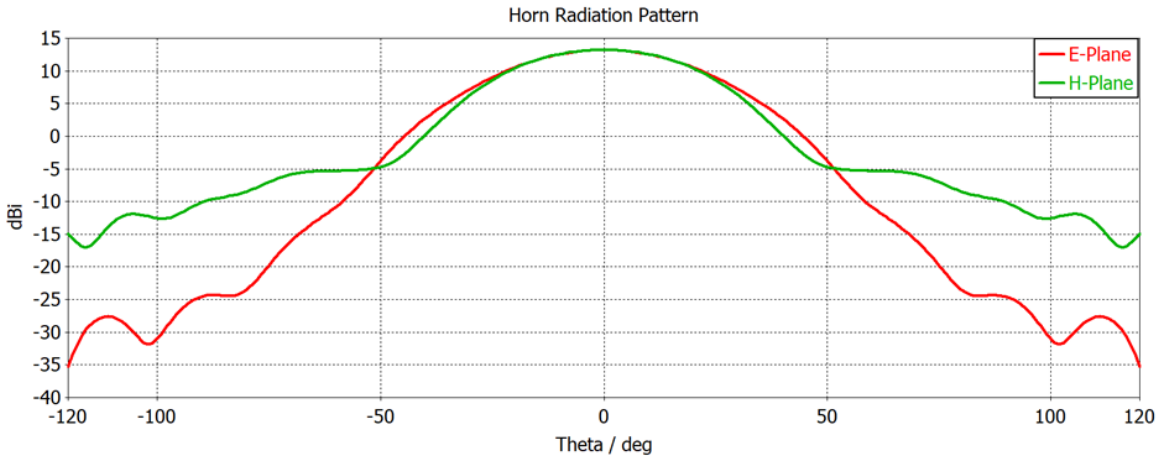

Figure 3-10: Radiation pattern of horn antenna at E-plane and H-plane

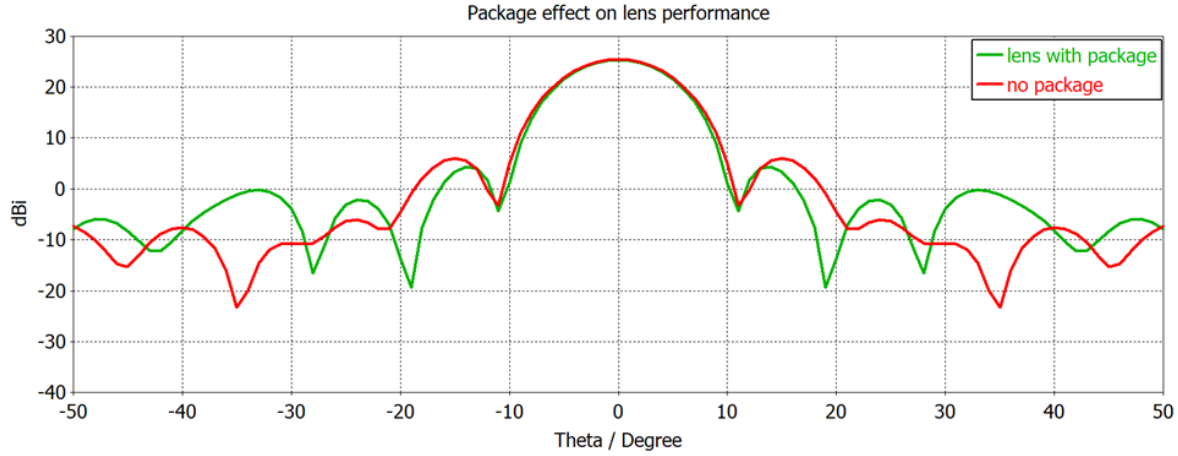

Figure 3-11: Radiation pattern (E-plane) of lens antenna (F=15mm) @144.75GHz with and without package

Another critical parameter that has been examined in order to proceed to the final lens design is the feed horn's phase center. In order to avoid phase errors that could lead to performance degradation, horn must be adjusted so as the phase center of the horn is positioned on the focus of the lens. Using CST studio, the phase center of the horn was found for all four D-band channels. As the same horn will be used for all D-band frequencies, an average value equal to a 1.2mm displacement in z axis direction was chosen for the phase center correction. In Figure 3-12 the radiation patterns for phase center corrected and not corrected case is presented respectively. When the horn is placed in the "correct" position, a 0.3dB increase in gain is noticed, while at the same time the sidelobe level is suppressed. Finally, it should be noted that the horn's displacement was implemented by decreasing the height of the base of the lens by 1.2mm.

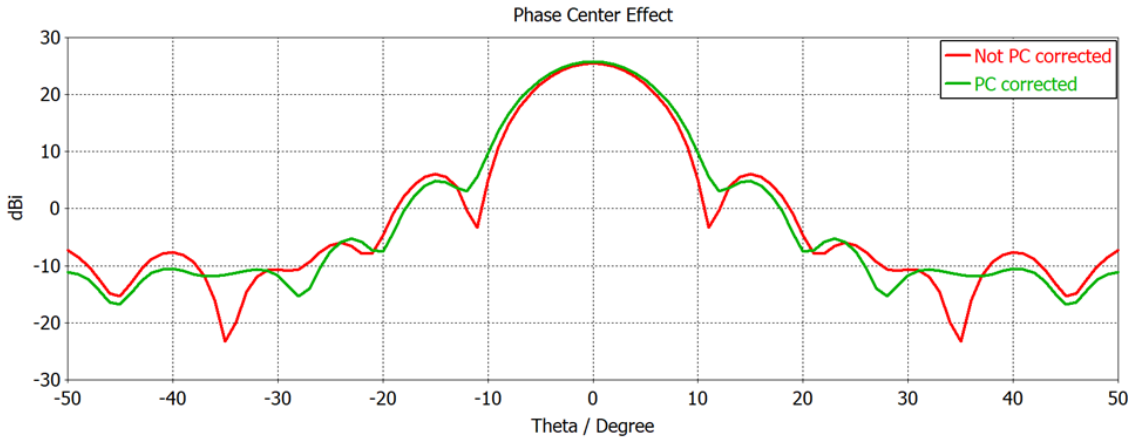

Figure 3-12: Radiation pattern (E-plane) of lens antenna (F=15mm) @144.75GHz with and without phase center correction

3.3.1.3 Simplified design for manufacturing

The above-described designs (Figure 3-7) have been further modified, in collaboration of NCSRD with IAF, and aiming of creating designs which are simplified in terms of geometry and though in terms of manufacturing. The simplified designs ("flat-base") of the lens are depicted in Figure 3-13. The performance of the simplified lenses is similar to the NCSRD detailed designs ("curved-base"). This is proved with the far field radiation patterns for lenses at 0° and 20° tilt cases for F=25mm shown in Figure 3-14. Similar behaviour stands for lenses F=15mm and F=20mm.

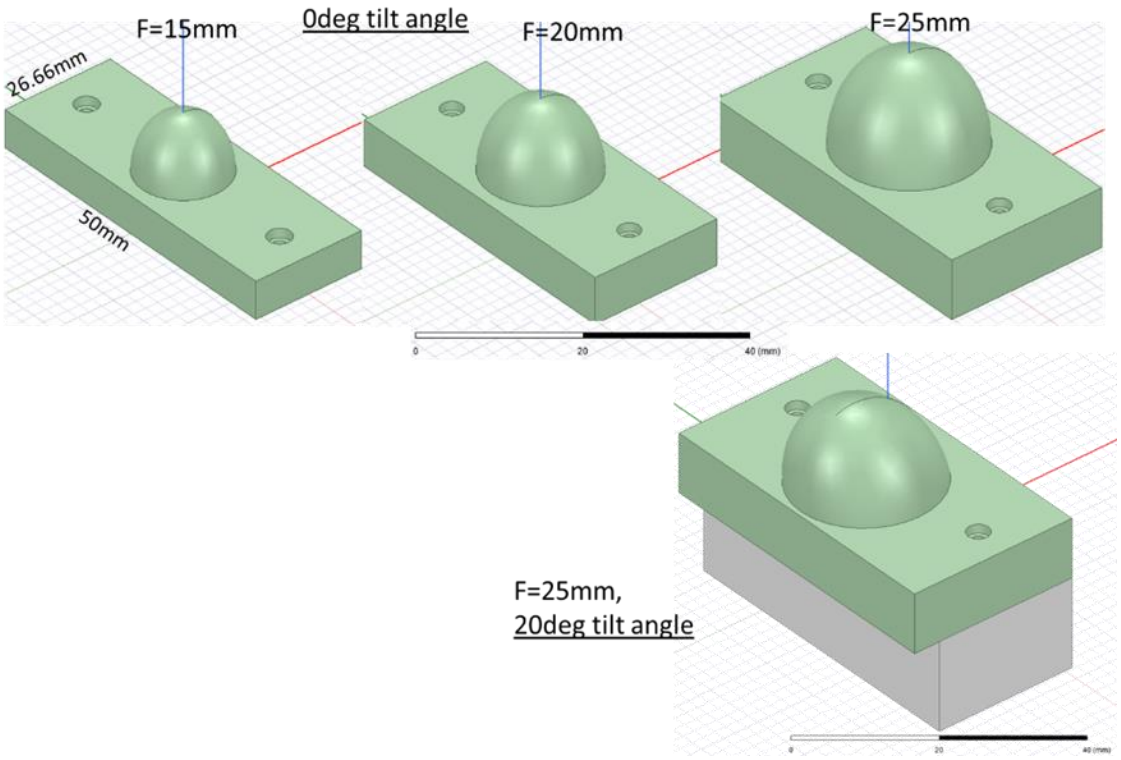

Figure 3-13: Simplified designs: 0° tilt lenses for various F (15mm, 20mm, 25mm) and titled lens for F=25mm

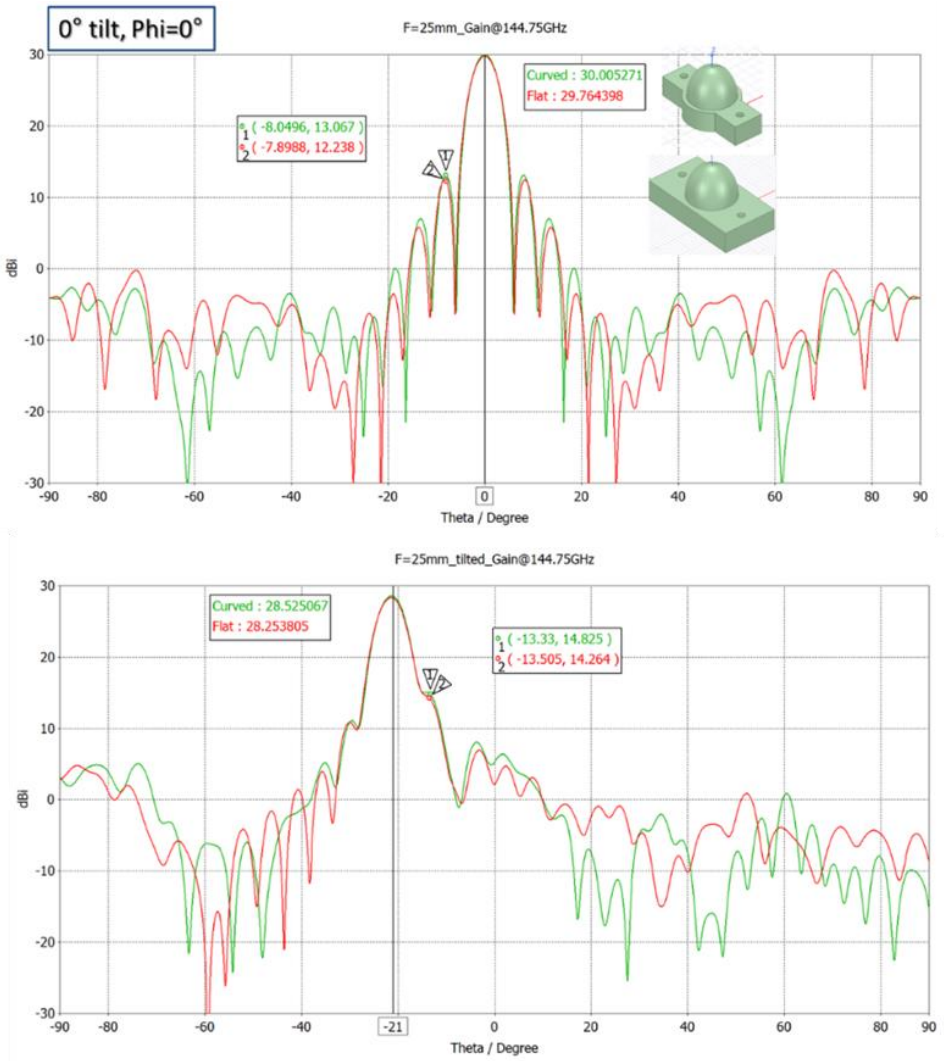

Figure 3-14: Far Field radiation patterns (H-plane) for lenses F=25mm (0°and 20° tilt) at 144.75GHz (green: "carved-base", red: "flat-base")

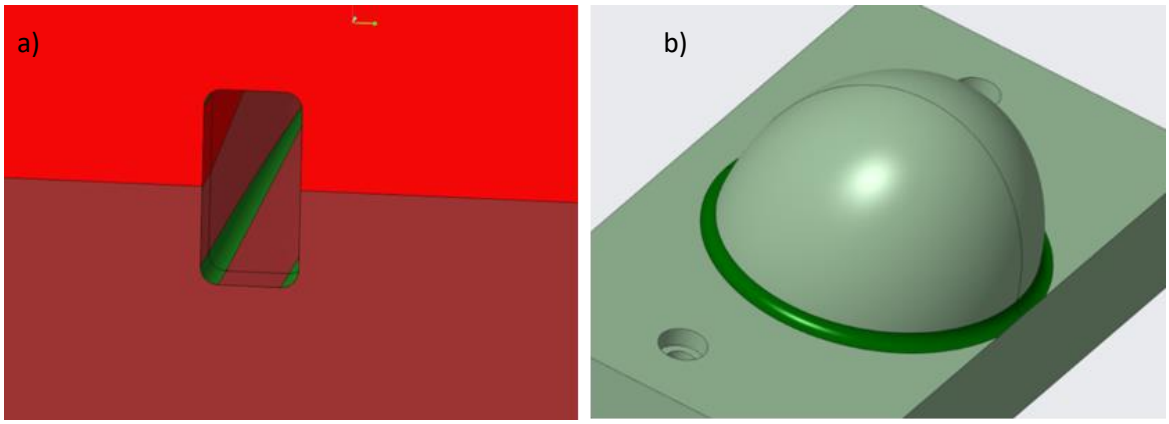

Figure 3-15: Final lens antenna model adjustments (details) for manufacturing (from step CAD file). a) waveguide port, b) dielectric lens (tilted)

For practical manufacturing reasons, some adjustments have been made for the final lens antenna model implementation. More specifically in Figure 3-15a, the waveguide port is shown with rounded edge corners instead of orthogonal. Also, Figure 3-15b a smooth transition between the ellipsoid parts and the base of the dielectric lens has been made. Both adjustments were included in EM simulations and no significant impact in the RF performance was noticed.

3.3.2 Manufacturing / assembly of lens antennas and feed-package

In Figure 3-16(a) and (b), the realized horn-package as well as an exemplary lens (20 ° tilt, F=25 mm), both manufactured at IAF's mechanical workshop, are shown. In addition, the milling of the negative half-sphere is clearly visible by observing the bottom of the lens on the right side of Figure 3-16(b). For antenna measurements, the lens under test is attached to the horn package obviously.

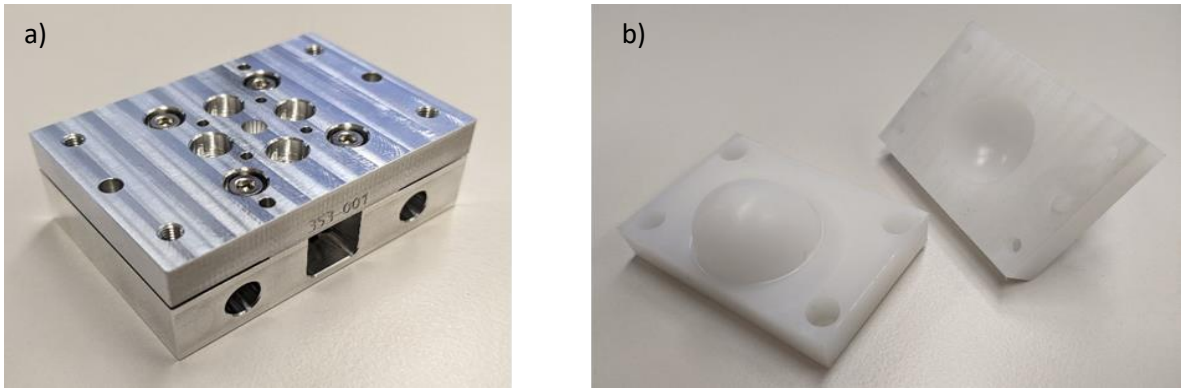

Figure 3-16: Manufactured horn-package (a) and exemplary HDPE 20 ° tilted lens (b)

3.3.2.1 Characterization measurement of lens antennas

After manufacture and assembly of lens antennas, the characterization measurements at IAF follow to compare estimated performance with simulations and though evaluate antenna radiation performance. The block-diagram of the measurement setup can be seen in detail in Figure 3-17 . Also, in Figure 3-18, two photos of the measurement procedure are presented.

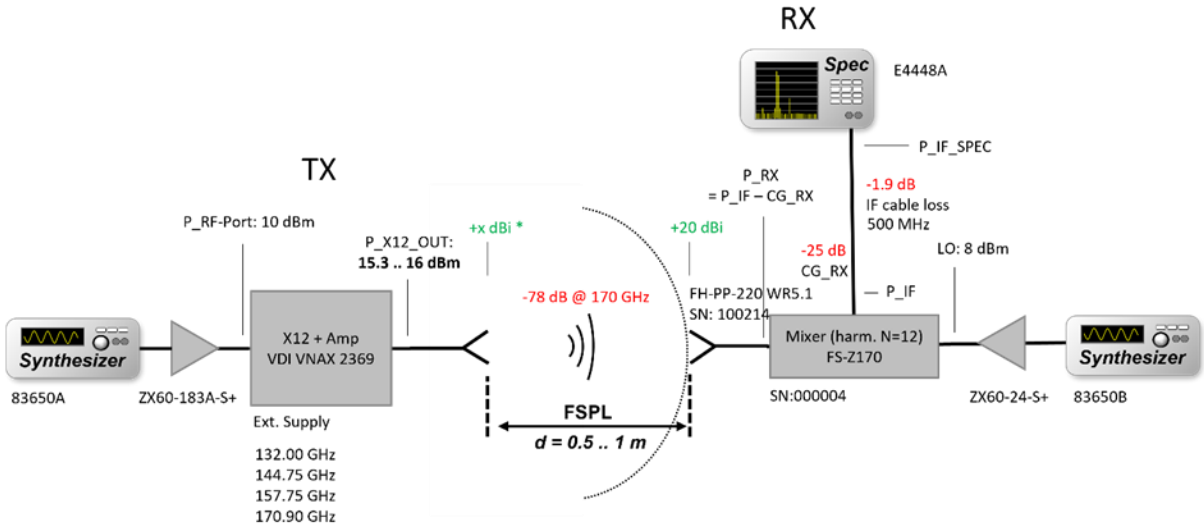

Figure 3-17: Lens antennas characterization measurement set-up at IAF

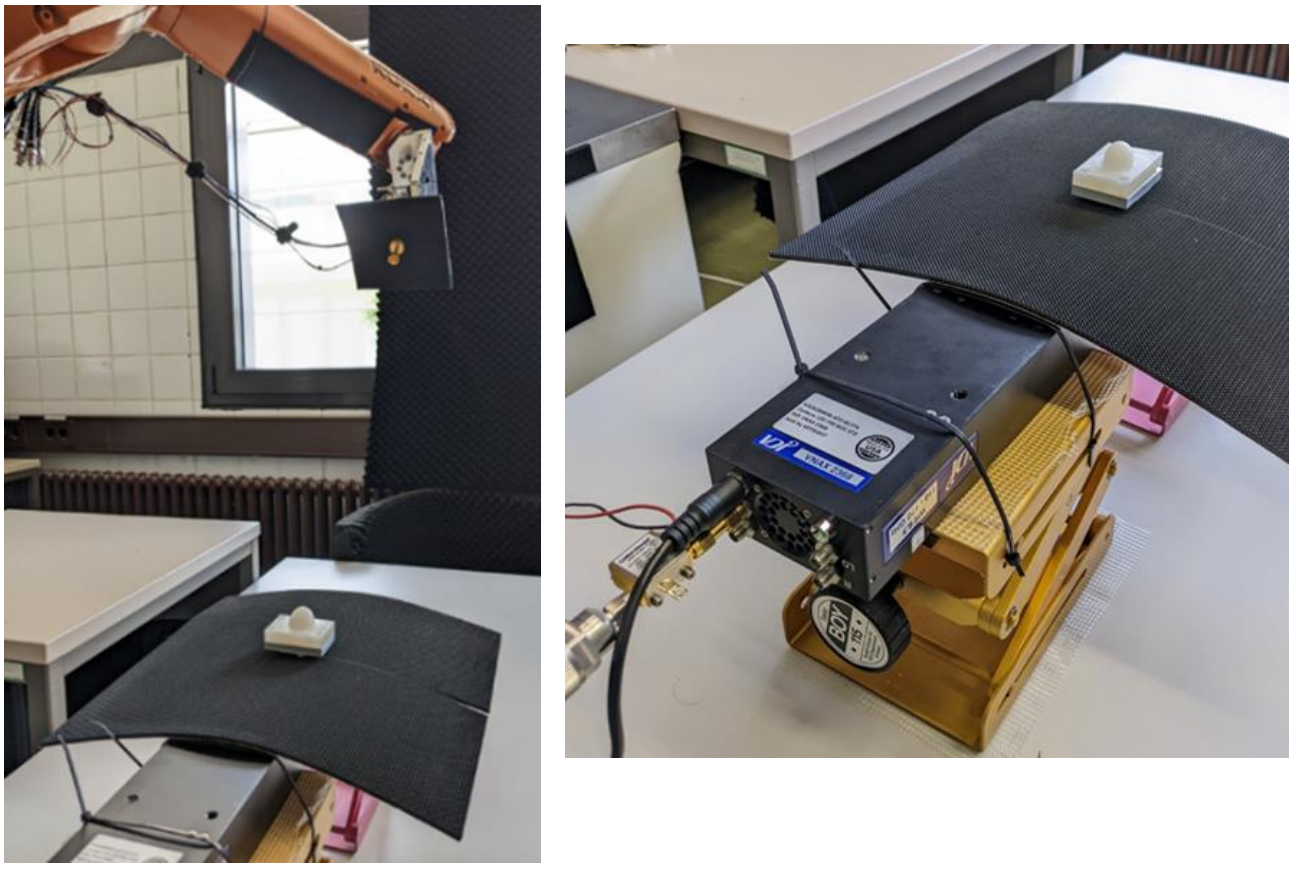

Figure 3-18: Lens antennas measurement procedure at IAF

3.3.2.2 Evaluation of lens antennas measurement results

A comparison of the radiation patterns of the simplified final lens antennas designs with the measured prototypes is shown in Figure 3-19 for the 0° tilted cases and focal lengths F=15mm, 20mm and 25mm, while in Figure 3-20 the 20° tilted case is shown for F=25mm. It can be generally noticed that a very

good agreement is achieved especially for the E-plane measurements. A slight displacement on theta angles can be noticed, regarding the maximum gain, between measurements and simulation. This could be due to various factors such as measurement alignment and lens misalignment.

Figure 3-19: Radiation patterns E and H-planes of 0° tilted lenses for F=15mm, F=20mm and F=25mm

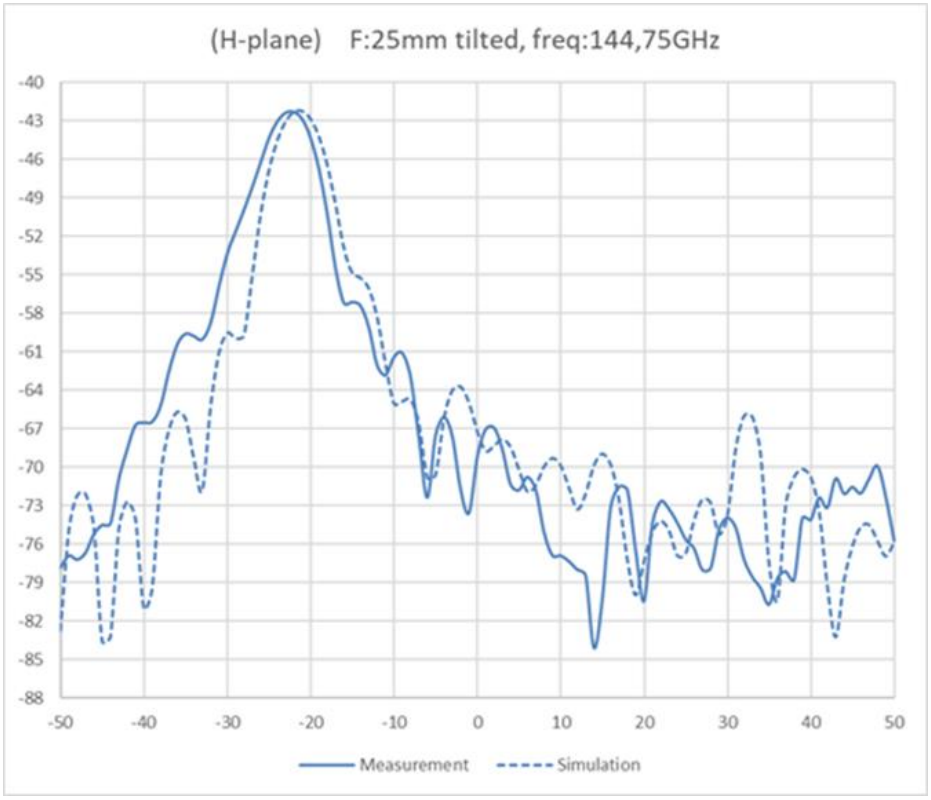

Figure 3-20: Radiation pattern (H-plane) of 20° tilted lens, F=25mm

3.4 Measurement and Results

As shown in Figure 3-1, a lab environment with little use of anechoic material is used to conduct the RF antenna radiation measurement. As to be observed in the picture, included into the 19-inch rack on the left, two signal sources for the generation of LO baseband signals for the Tx and Rx path of the experiment. Furthermore, a spectrum analyzer, which is connected to the IF port of a subharmonic receiving mixer is placed there. DC supplies are used to power LO baseband amplifiers due to the use of very long cable assemblies. On the table, there is a commercially available vector network analyzer frequency extension module by VDI which acts as a frequency multiplier-by-twelve to generate signals in the full D-band frequency range, which is between 110 GHz to 170 GHz. Those signals are emitted using a medium-gain horn antenna with approximately 26 dBi of antenna gain. Possible unwanted multipath propagation is prevented using anechoic material at critical locations in the experiment, though it is removed in the image for better visibility. The metasurface structures are processed on top of a 4-inch fused-silica wafer, further simply called "sample". It is tilted by a fixed angle of 40 ° with respect to the incidence EM-plane by using a tiltable wafer mounting construction. The horizontal distance is chosen in a way, that the sample is illuminated by a -3 dB spot diameter of approximately 20 mm to achieve a good trade-off between its far-field distance and its radiation efficiency.

Using a six-axis robot arm, a receiving low-gain horn-antenna with approximately 20 dBi in combination with the receiving mixer undertakes a radial trajectory in a distance of approximately 700 mm with respect to the illuminated sample. The digitized IF data of the spectrum analyzer finally is used to generate an antenna radiation pattern.

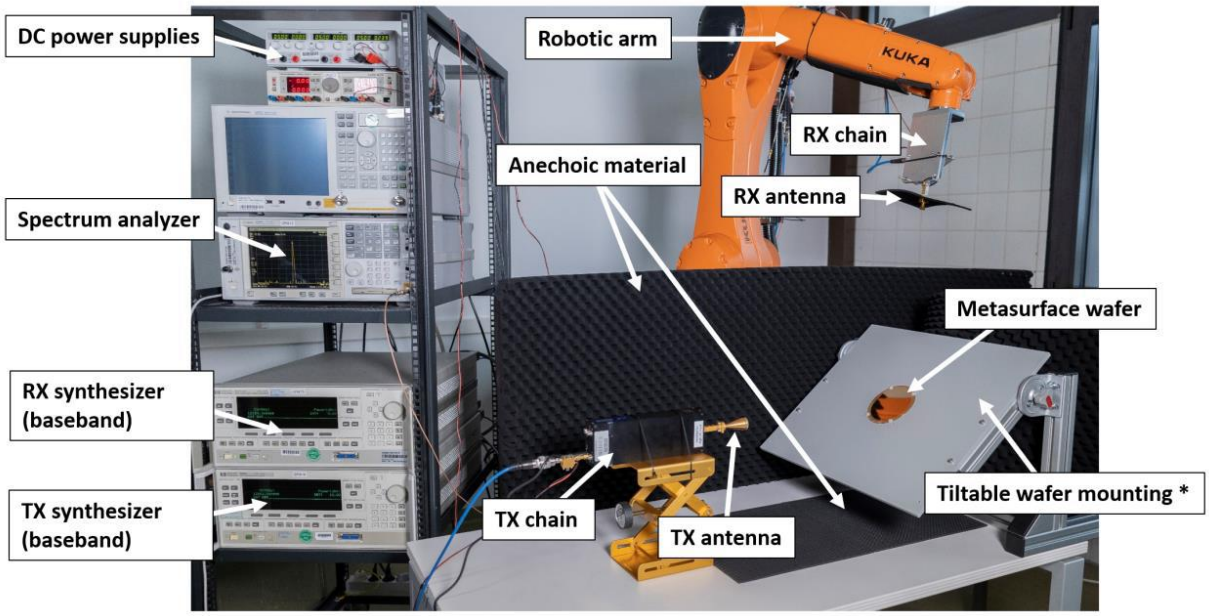

Figure 3-21:: Lab environment with MTS measurement set-up. Anechoic material around wafer removed for enhanced visibility.

Figure 3-4 shows the block diagram of the proposed measurement setup. Antenna radiation patterns are generated at the ARIADNE sub-band frequencies 144.75 GHz, 157.75 GHz, as well as 170.9 GHz. All of the three MTS samples were specifically designed to work best at those respective frequencies.

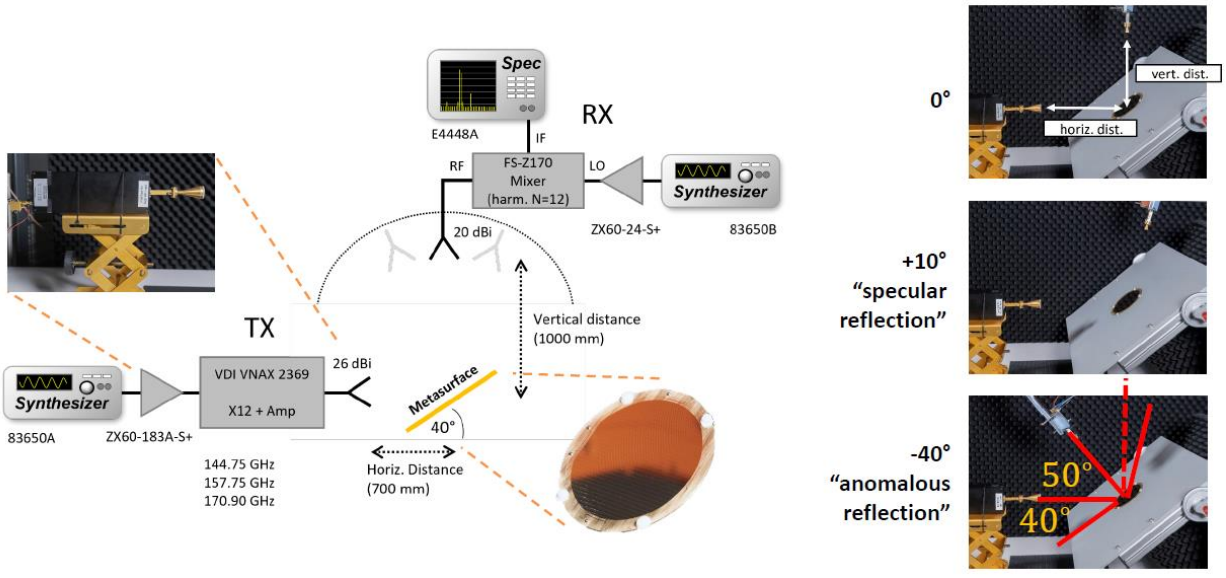

Figure 3-22: Left: Block-diagram of measurement setup of a MTS-enabled PtP NLoS demonstration targeting demonstrator 2. Right: Angular coherencies of the proposed measurement setup w.r.t. the moving robot arm. (a): 0 °, (b): +10 ° (specular reflection), (c): -40 ° (anomalous reflection).

For a better understanding of the angular coherencies, Figure 33 may be observed. With respect to the moving receiving antenna, Figure 3-4 (a) shows 0 °, Figure 33 (b) shows +10 °, which is the location of the specular reflection in this case, and Figure 33 (c) shows -40 °, which is the normal direction of the MTS sample as well as the anomalous reflection in this case.

As to be observed in the three resulting plots (Figure 3-5, Figure 3-6, Figure 3-7) for three MTS samples S05, S06 and S08 investigated, respectively, an incident signal in addition to its heavily suppressed specular reflection at +10 ° undergoes a strong anomalous reflection into the normal direction of the illuminated sample, to be observed at -40 ° in the radiation plot. Hitting the design frequency of the MTS samples, the reflection each is maximal at -40 °, which again is the normal direction of the sample. Changing the frequency away from the design-frequency shifts the beam in another direction, due to the nature of the designed radiating phase-dependent elements.

By illuminating a simple metal plate instead of an MTS sample, only the “to-be-expected” specular reflection at +10 ° is visible, to also be observed in each of the three plots.

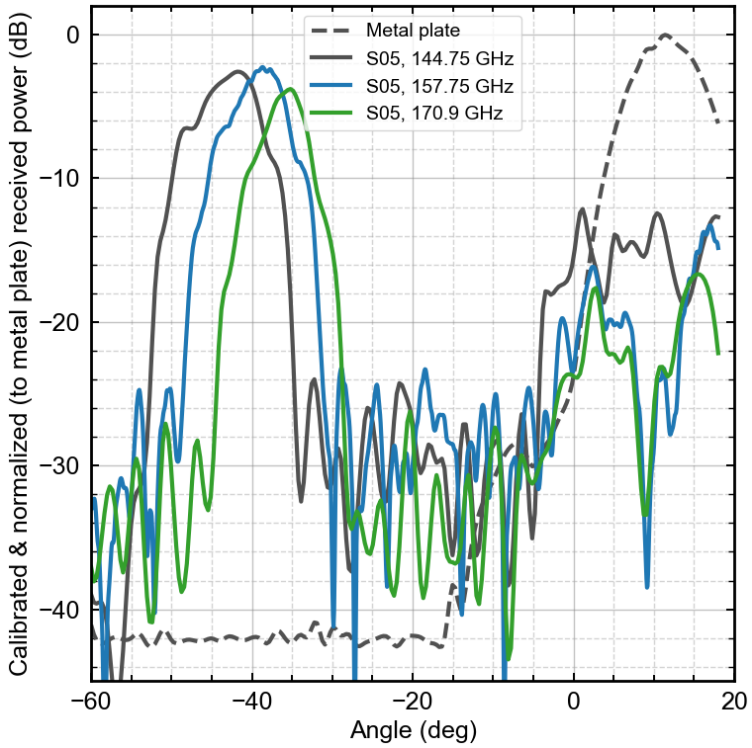

Figure 3-23: Far-field radiation plot of MTS sample S05 at various frequencies using proposed measurement setup. Design-frequency of S05 is 157.75 GHz.

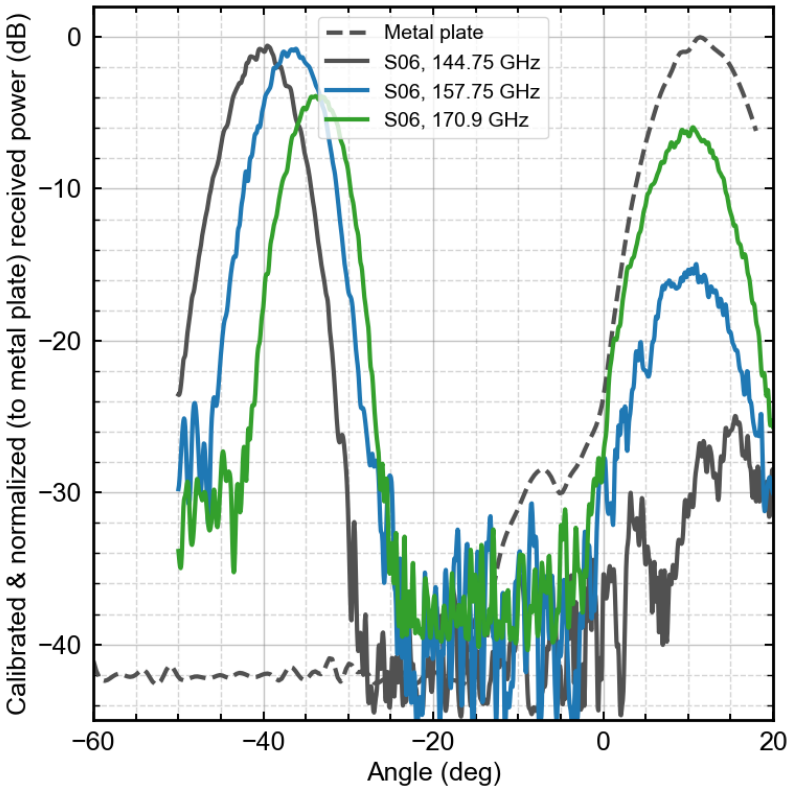

Figure 3-24: Far-field radiation plot of MTS sample S06 at various frequencies using proposed measurement setup. Design-frequency of S06 is 144.75 GHz.

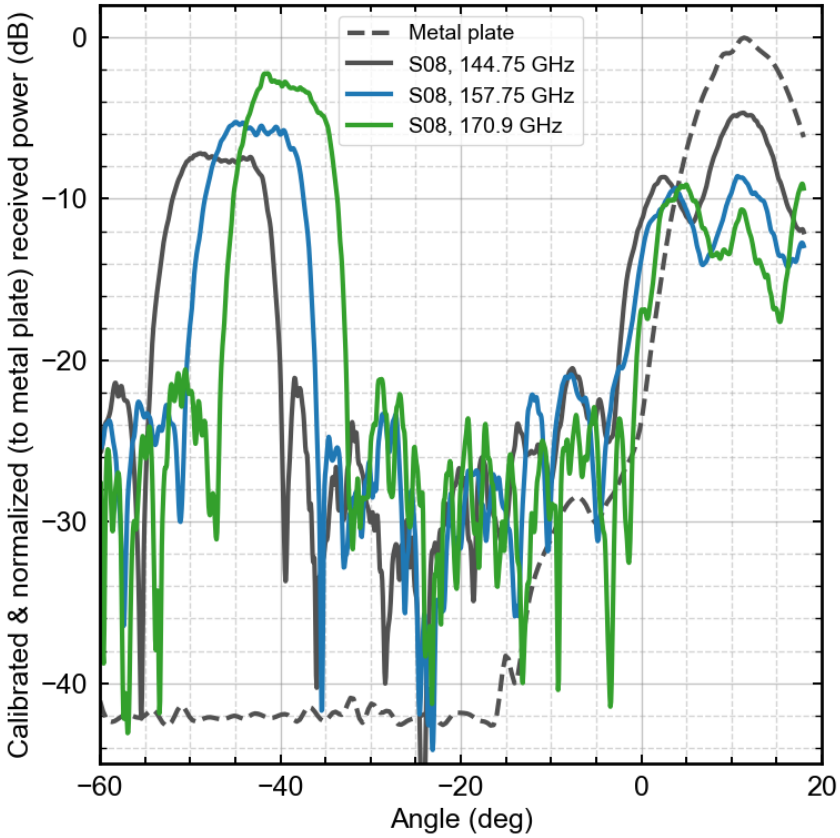

Figure 3-25: Far-field radiation plot of MTS sample S08 at various frequencies using proposed measurement setup. Design-frequency of S08 is 170.9 GHz.

To conclude, different frequencies in combination with their specifically designed MTS wafers have been examined, all matching the excellent predictions by simulation made by project partners in WP3. Thus, the (static) RIS structures are working as expected. However, the efficiency is only roughly estimable by comparing the received power levels with the received power levels measuring a flat metallic surface. In addition, care must be taken to maintain reasonable horizontal and vertical distances in order to perform the measurement in the far field region of the sample to overcome near-field interference effects.

From the lab environment a demonstrator was built up as shown in figure 3-8. This demonstrator was presented at the EuCNC in Gotheburg.

Figure 3-26: Metasurface demonstration on the EuCNC in Gotheburg 2023

The setup for the demonstration consists of the RX- and TX-Modules from the ODUs, the metasurface wafer and an oscilloscope to demonstrate the anomalous received signal.

4 Demonstrator 3: An intelligent D-Band network demonstrator

4.1 AI/ML application for LoS-aware directional connectivity

Beyond 5G (B5G) systems are expected to integrate AI/ML algorithms and techniques in various layers of the network management stack. Within the context of LoS-aware fronthaul connectivity scenarios that are part of the ARIADNE use cases, we developed a solution for LoS aware directional connectivity as part of our (Altair RapidMiner) work conducted in WP4. This includes a software application, henceforth referred to as a demonstrator application that solves the User Equipment (UE) to Access Point (AP) association problem for dense and evolving networks. The details of this work are presented in the WP4 deliverable D4.4 (chapter 2 entitled “Directional Connectivity using AI/ML in Dense and Evolving Networks”). This work achieved important objectives of tasks T4.1 and T4.2 within the context of solving UE-AP association problem under dynamic settings for very large scale and dense B5G networks. The demonstrator developed in this regard represents a system that employs our “Hybrid Metaheuristics and Machine Learning” framework, which delivers a dual solution – i.e. one produced by online optimization algorithms and the other by machine learning models. This hybrid solution is now encapsulated in a tailor-made graphical user interface (GUI) based application, which enables the end-user to actively evolve the network using trigger events and extract an on-the-spot solution from the AI/ML methods which dynamically adapts to the changes committed by the end-user.

In addition, a secondary scenario showcases the work conducted in WP4 regarding the influence of attributes on the prediction of LoS or pathloss for a given propagation environment that effects the channel properties between the base station (BS) and the mobile station (MS).

4.1.1 Demonstration scenario 1.1: AI/ML based UE-AP association (a joint resource allocation and LoS blockage minimization problem) in dense and evolving networks

The demonstrator for this scenario implements an AI/ML solution that shows continuous reliable connectivity between a UE and an AP by associating all UEs to optimal APs under dynamic conditions, where the network is large (usually 100+ APs and 600+ UEs), has dense LoS blockages and continually evolves. Hence, this demonstrator differentiates itself as an online, real-time problem-solving application that illustrates the use of both Metaheuristic optimization algorithms and Machine Learning predictive models. Providing high quality associations in such large-scale, dense, and evolving networks increases the association challenge manifolds because the associations must satisfy the resource requirement of each UE in an environment where the partial blockages obstructing the LoS between UEs and APs are frequently changing. Thus, partial blockages must be automatically detected and considered in real-time. This demonstrator addresses this real-time problem, which on one hand allows an end-user to interact with our Hybrid Metaheuristics-Machine Learning framework through a custom-made GUI, and on the other hand, delivers a dual solution (i.e., UE-AP associations) that can be used to initiate pro-active handovers while also consolidating network resources. The former allows a good quality of service to the end user while the latter allows to utilize network resources at the APs in an optimal manner, where some APs may not even be needed at full operational level, hence saving energy and operational cost.

The main concept is that, given a recurring optimization problem such as the UE-to-AP association problem, which is a joint resource allocation and LoS blockage minimization problem, first a network model comprising of UE demands, AP resources and topology is represented as a dataset. Next, this dataset is loaded into the demonstrator, which allows to solve the UE-AP association using either the “Online Optimization” or “Online Predictor” modules. The solutions from both approaches can be compared for quality side by side. The diagram shown in Figure 4-1 depicts the architecture of the mentioned Hybrid Metaheuristic-Machine Learning framework, which the demonstrator implements as a GUI application. The framework also paves way for online learning as well although that is considered beyond the scope of this work.

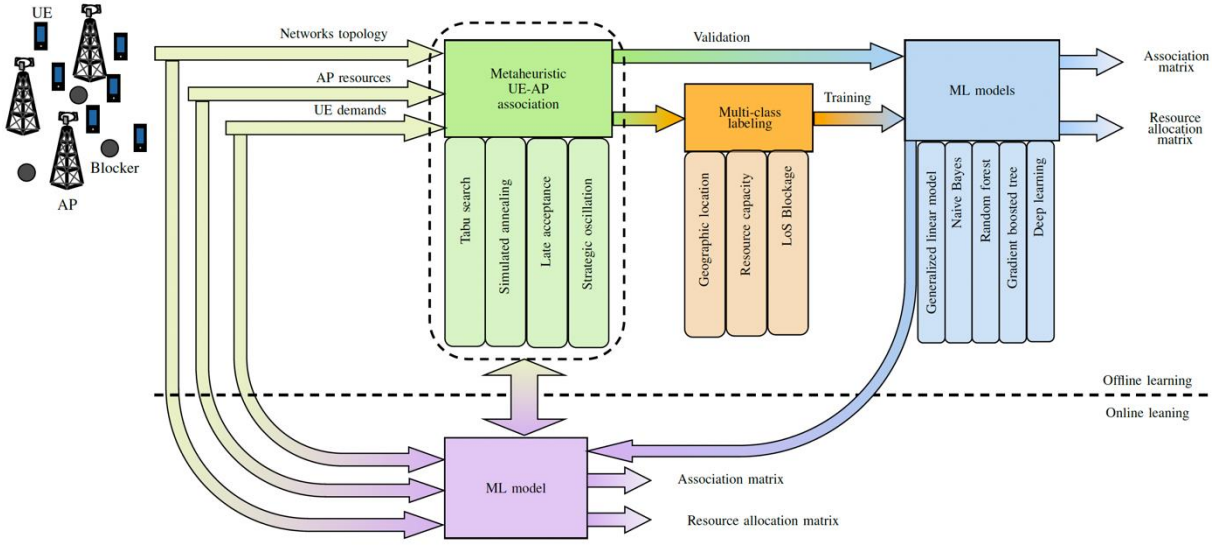

Figure 4-1: Design of Hybrid Metaheuristic-Machine Learning Framework

As shown in Figure 4-1, once the network model is loaded as a dataset, the online optimization module starts to solve the problem in a continuous fashion. We have the ability to use any of the Metaheuristic algorithms supported by the online solver such as Tabu Search, Simulated Annealing, Late Acceptance or Strategic Oscillation. The GUI also allows the end-user to provide various trigger events that may change the problem instance being solved in real-time where the solution also adapts accordingly in near-instant manner. The assignments discovered by the Metaheuristic algorithms are treated as ground-truth i.e. each UE is assigned an optimal AP that satisfies problem constraints. Based on our work in WP4 on this problem, we have also shaped this assignment problem as a Supervised Machine Learning problem by creating a label attribute that comprises multiple classes as shown in Figure 4-1. The ground-truth is used to generate training data for Machine Learning models, which are updated at regular intervals.

The ML models that have already been trained on the existing datasets are available in the online predictor module of the demonstrator. When applying the ML model to get predictions for UE-to-AP associations, the demonstrator also shows the time taken to do data preparation, getting the predictions (scoring), and post-prediction resolution step which are of importance to evaluate the low latency connection establishment requirement in terms of runtime incurred by the use of ML models for the association problem.

Figure 4-2 shows the overall design of the demonstration application that was conceived at an earlier stage of the project and documented in Deliverable D5.1. It shows the basic pillar and interactions. The green arrows are interactions, while the blue boxes represent different sub-components of the application that enable the two main modules of the GUI application namely the “Online Optimizer” and “Online Predictor”. These two modules are shown respectively in the Figure 4-3 and Figure 4-9, which show the two front-end screens of our demonstrator application.

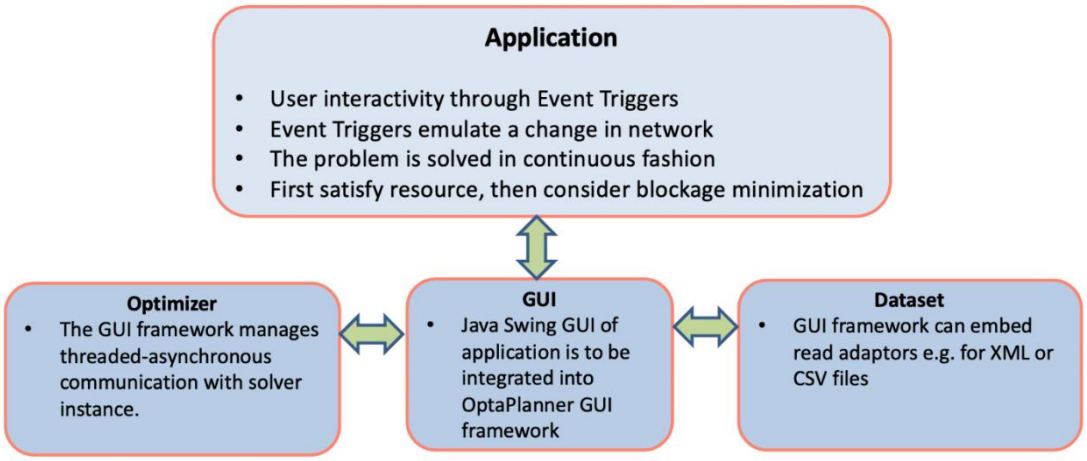

Figure 4-2: Conceptual design of demonstration application

4.1.1.1 Online Optimizer Module

Figure 4-3 shows the “Online Optimizer” module of the demonstrator. It allows to load an unsolved dataset to load the network model. This can be done using the “Open” button or just clicking the pre-loaded dataset seen in the “Unsolved dataset shortcuts” panel. Next, the “Solve” button is pressed to start solving the problem and the system automatically discovers the optimal UE-AP assignments that are rendered in the “Network Plot” shown in the central area of the demonstrator. Below this plot, an “Optimization Progress” and “Link Quality” plot is dynamically rendered as well. The left side of the

demonstrator shows various “Solution Quality” panels. The first panel shows the state space of the problem inherent in the dataset. The state space gives the theoretical upper bound of all possible UE-AP combinations. The panel also shows the current score in terms of initial (unsolved stage), hard and soft score (updated during solving). The following panel is the “Network Usage” panel which shows how many APs are used out of available APs, and the “Link Blockages” information, which shows the quality of LoS links in terms of number of blockages existing between the UE and the AP assigned to it by the online solver. The best assignments are those which minimize all links to zero blockages. Nevertheless, the panel shows also links with 1, 2 or more than 2 blockages for a comprehensive evaluation and later comparison with the solution produced by the ML model predictions.

The next panel is “Triggers to Simulate Network Evolution”, which allows the end-user to trigger a particular change event in the network such as adding a new UE, remove a selected UE, move a selected UE, change the resource requirement of a selected UE, add a new AP or remove a selected AP. Changes induced by these events are reflected in the network plot, optimization plot as well the link quality plot – providing multi-modal and real-time insights to the end-user. Whenever a trigger is executed, the network is considered to have evolved and hence its state (i.e. updated dataset as well its corresponding ground-truth) can be saved as evolved dataset using the “Save as” button. The evolved dataset (comprising of UEs, APs, Blockages among them) are usually to be saved once the best solution (having hard and soft score of 0) is achieved. Hence, online optimizations can be used to provide just-in-time solutions as well as frequent snapshots of the network, which are leveraged for (re)training of the ML predictive models in our hybrid scheme. The complete detail about each AP in terms of how much resource it offered, the UEs assigned to it along with the total resource required by all the assigned UEs is shown in the “AP Allocation Details” table. Likewise, all details about the UEs are shown in the “UE Allocation Details” table. This allows for adaptiveness and qualitative analysis of the resource allocation metaheuristic algorithm for network changes triggered in real time.

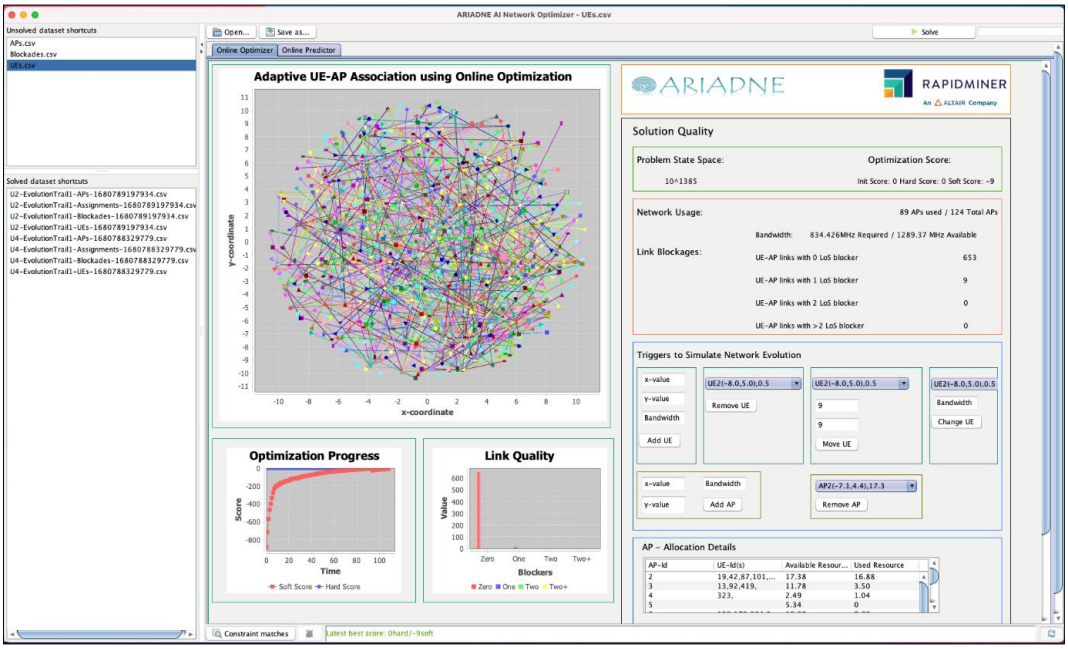

Figure 4-3: AI/ML Demonstrator for UE-AP Associations - View of Online Optimizer Module

In the following, we briefly explain the use of triggers in this demonstrator application.

Adding a UE

Figure 4-4 shows the result of "Add UE" trigger. As seen in the yellow colored tooltip, a new UE with identifier 663 has been added at (x,y) coordinate location (4,11) and automatically assigned to AP with identifier 121, which is determined to be the optimal AP to serve the new UE, without violating the hard constraint (resource satisfaction) and soft constraint (LoS blockage minimization) in the global solution – as evidenced by the Hard and Soft score values of 0.

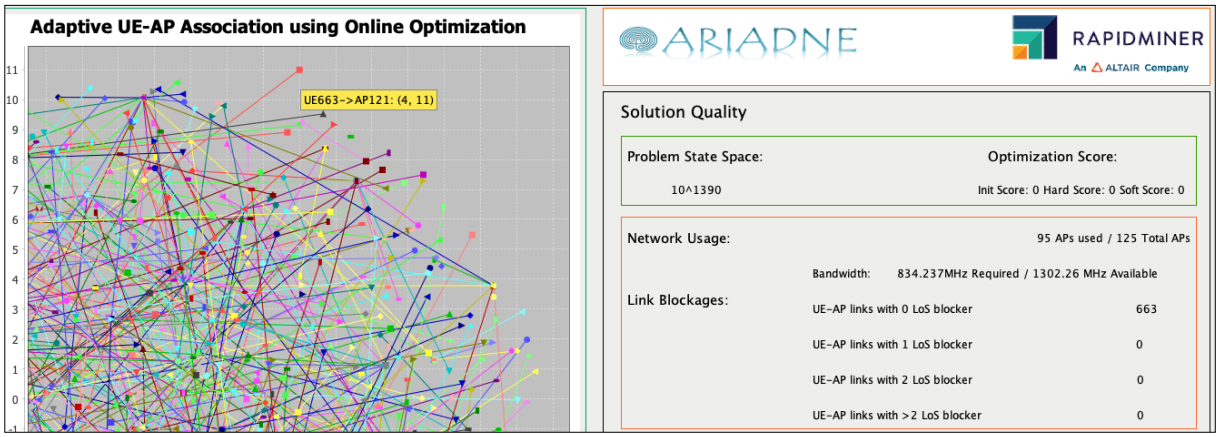

Figure 4-4 A new UE added in the network

Moving a UE

This trigger allows to simulate mobility of a UE (or multiple UEs) from their original location to a specific direction, thereby studying the resource satisfaction and LoS blockage avoidance in a particular geography or for a particular density of UEs and APs. As seen in Figure 4-5, the UE 663 is now moved to a new location (-9, 10), which has also changed its assignment to a new AP (AP 41). However, the new globally optimized score is reached after several optimization iterations.

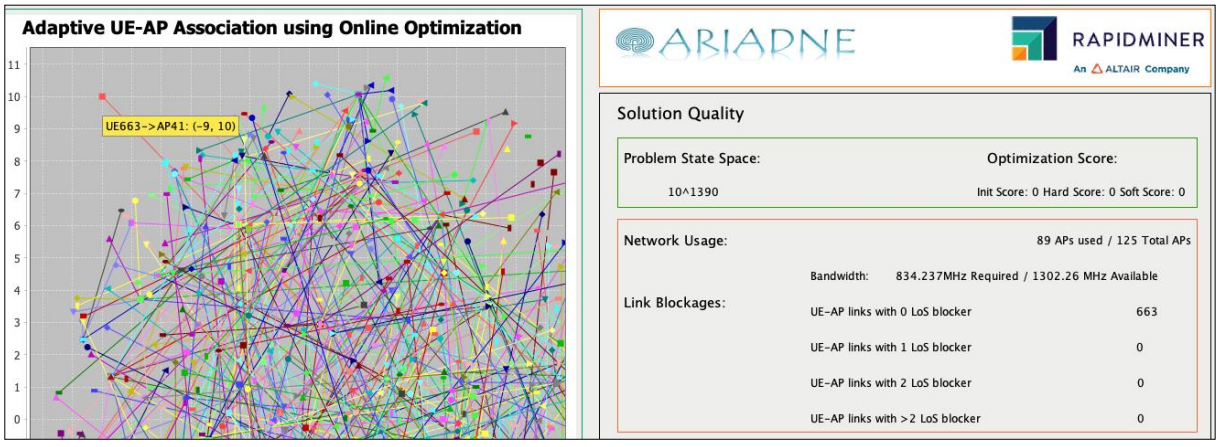

Figure 4-5 An existing UE is moved in the network

Changing a UE's resource requirement

This trigger allows to change its original resource requirement (i.e. bandwidth). As seen in Figure 4-6, the left panel shows UE104 located at (x,y) location (-0.7,9.5) required 2.0 MHz of bandwidth. In the

upper table of the right-hand panel, the figure further shows the allocation details of AP75 (highlighted) where all UEs assigned to it – along with UE104 are listed, along with the "Available Resource" i.e. bandwidth available at AP75 (17.09 MHz) and the "Used Resource" i.e. sum of bandwidth required by all UEs assigned to it (14.22 MHz). In the lower table of this right hand panel, allocation details of UE104 are highlighted, which show that it is allocated to AP75, requires resource (2.0 MHz bandwidth) and faces 0 LoS Blockers when connecting with AP104.

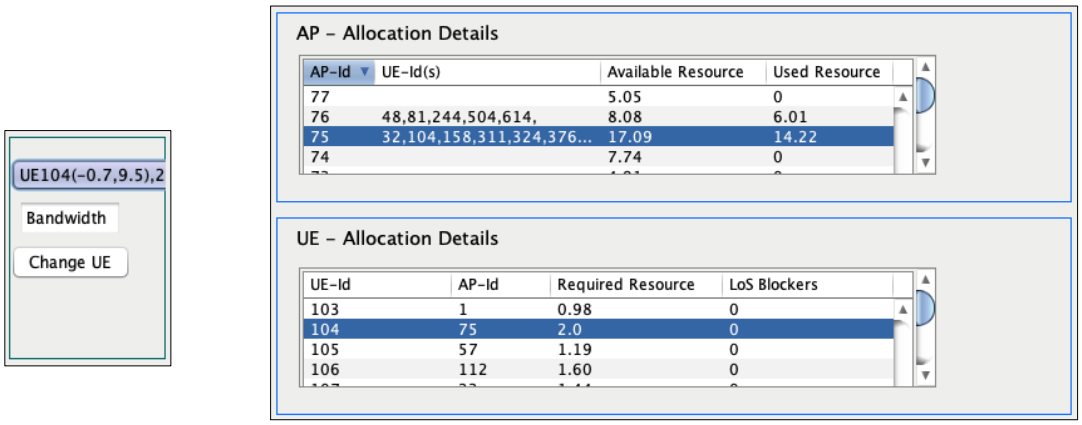

Figure 4-6 Before Resource Change Trigger: UE104 requires 2.0 MHz bandwidth resource and is assigned to AP104

After the required resource is increased to 5.0 MHz, the assignment is updated as well. The new assignment details are shown in **Error! Reference source not found.**, where the left and right hand panel reveals the updated resource and allocation information. The UE is allocated to AP10 which has ample resources to offer and also has no blocker in the LoS between it and the UE.

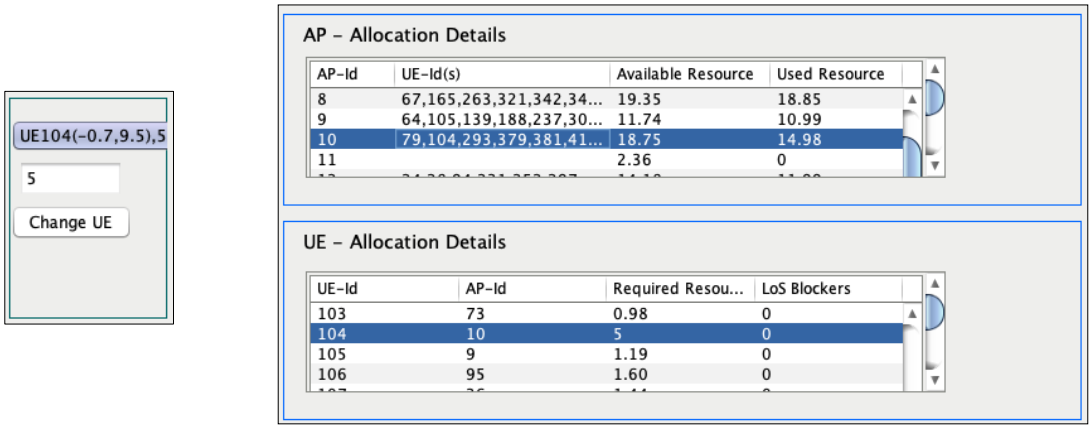

Figure 4-7: After Resource Change Trigger: UE104 now requires 5.0 MHz bandwidth resource and is assigned to AP10

Removing a UE

Removing a UE or multiple UEs is also enabled with a simple selection of the UE from the list box and clicking the Remove UE button from the triggers panel.

Adding and Removing an AP

An AP can be added to modify the topology of the network in order to study different levels of AP and UE densities in a particular direction. This trigger is suitable for network topologies that build up

spontaneously e.g. in case of natural disasters or crowded events, where access points (such as drones) may need to be deployed without much prior planning in order to cater for additional connectivity requirements. As shown in Figure 4-8, the upper left hand trigger panel allows to specify the x and y coordinates (here (0,0) is entered) and the available resource (here 10.5 MHz is entered). Upon pressing the "Add AP" button, the AP is added to the network and can be also be seen in the list box of APs for the "Remove AP" button as well in the "AP Allocation Details" table.

Generally, the central locations of the network are expected to be under high demand as the resource contention increases. However, in this case, the figure shows that no UEs were assigned to this newly added AP as the current solution was already optimal. The designer may stress test the system by removing multiple APs or those located in strategic locations (where more coverage is required), by using the "Remove AP" button which almost always result in high utilization of the remaining APs especially where UE density is higher.

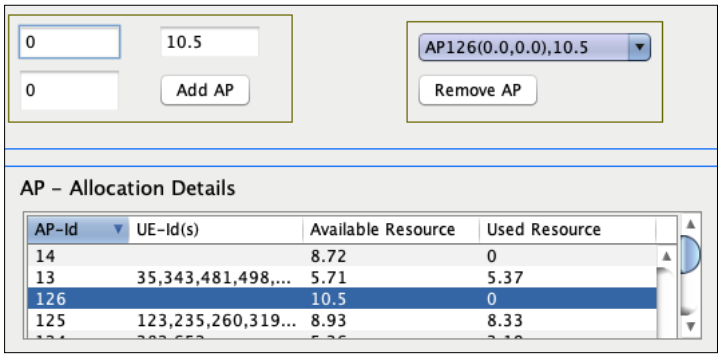

Figure 4-8 Addition and Removal of an AP

4.1.1.2 Online Predictor Module

Figure 4-9 shows the second module "Online Predictor" of the demonstrator. It also allows to load the same datasets (representing network models) as the "Online Optimizer". However, here we are not interested in executing the "Solve" button but we draw our attention to the first panel under "Solution Quality", which lets the end-user select one of the four pre-trained ML models that would predict the UE-AP associations when the "Predict Associations" button is clicked. The following panel displays the "Network Usage" and "Link Blockages" information. Similarly, the AP and UE level association details are shown in the table components. As soon as predictions are received by applying the selected ML model, the "Network Plot" updates itself. In contrast to the "Online Optimizer" module, the "Online Predictor" module shows a plot for "Prediction Runtimes" in addition to the "Link Quality" plot. The prediction runtimes are important metrics because the association problem requires a low latency solution. The prediction runtimes are decomposed into time spent on data preparation (referred shortly as "Prep"), scoring the data i.e. applying the model on data to get predictions (referred shortly as "Score"), post-prediction step to resolve the predicted class to an actual AP belonging to that class (referred shortly as "Resolve") and average time to predict assignment for 1 UE (referred shortly as "1 UE-AP"). All plots are zoomable, which allows a drill-down behavior if the values are not visible in default resolution. Tooltips are provided to data elements being displayed in plots as well for further guidance to the end-user.

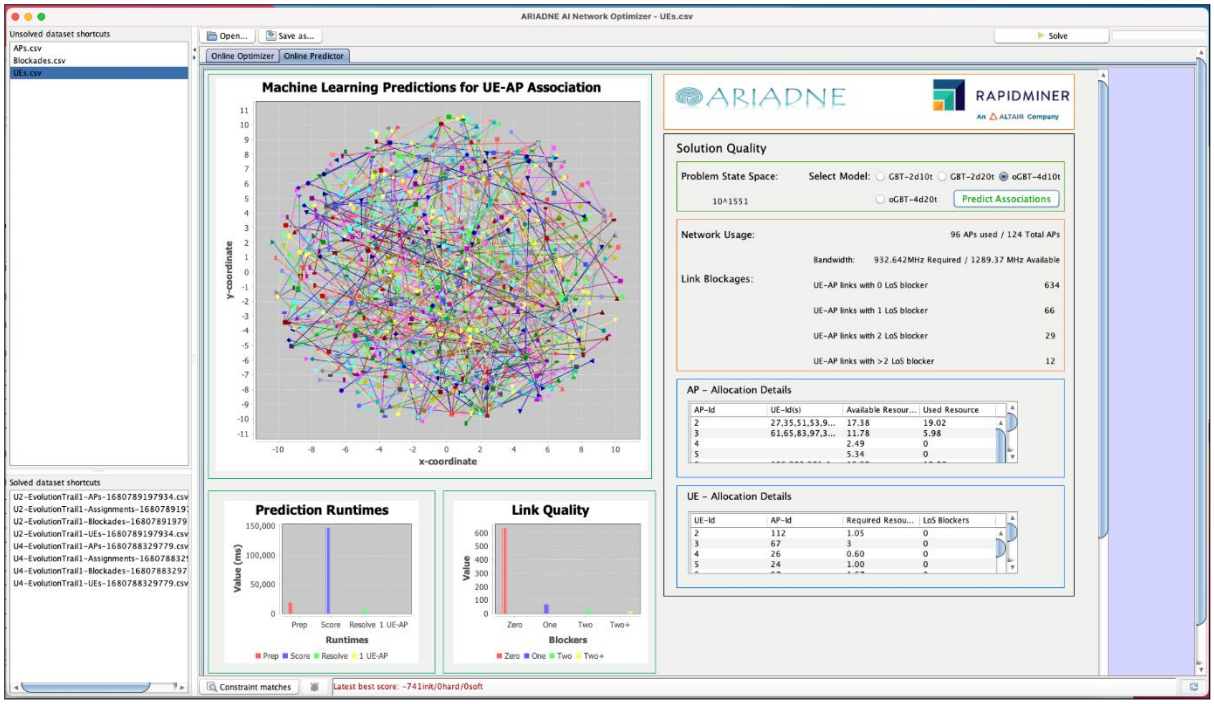

Figure 4-9: AI/ML Demonstrator for UE-AP Associations - View of Online Predictor Module

Conclusion

In conclusion, the demonstrator for the UE-AP association problem has achieved our vision behind the Hybrid Metaheuristics-Machine Learning framework, which is summarized below:

1. Identify a reusable, common, and configurable approach that can deliver highly customized AI/ML models that can be showcased to solve the UE-AP association problem for the given network model.
2. Enable the end-user (analyst, engineer or data scientists) to evaluate and compare the quality of both optimization and prediction-based solutions.
3. Study the transformation of different constraint-based optimization problems into a Machine Learning-based predictive paradigm by way of studying and solving the UE-AP association problem.
4. Solve the problems under dynamic settings which is achieved using online optimizations and enabling continuous updates of the ML models by discovering ground-truth solutions to different (evolved) snapshots of the network. In this way, the demonstrator also eases the generation of more training data by letting the user easily interact with the demonstrator GUI.
5. Conferring the ability to retrain or update the ML models regularly with new data until an acceptable performance level is reached for a variety of changes that are expected in the real network.

4.1.2 Demonstration scenario 1.2: Exploration of ML predictions for environment-specific LoS Connectivity

This is a secondary scenario, which is developed as an extended contribution. It is based on the analysis of challenges and opportunities for Machine Learning in the channel modelling domain for both LoS and NLoS cases by applying predictive exploration to environmental and wave level channel properties. The objective here is to understand the feasibility of predicting the existence of LoS and analyzing the

statistical relation between attributes of mobile channels and geometrical link condition as seen in datasets supplied by project partner AALTO.

Different datasets representing different indoor and outdoor environments have been studied in the course of the project, for which ML models have been trained and reported in previous WP4 deliverables (more recently in D4.4 chapter 3 entitled “ML model for environment-specific LoS connectivity at the physical layer”). Briefly, the latest work has focused on the dataset representing Helsinki-Vantaa airport Terminal 2 as generated by the domain experts (from AALTO) using the Ray-Tracing network tool. This environment contained two BS at a fixed location and 100 routes for each BS, where a MS is considered to be moving in each route. Each route has 150 datapoints. For each route, a separate uniform distribution of stationary pedestrians is generated – some of which interfere or obstruct the LoS between the MS and BS. In general, this and previously considered datasets contained geometric locations of BS and MS (along the routes) and values of multiple channel level attributes as received by the MS at each location point within the route. The problem was shaped as a Supervised Machine Learning problem specifically as a binominal classification problem, where the two classes for the label (prediction) attribute are “LoS” or “NLoS” (represented by 1 or 0 respectively). Different ML models were trained to predict the label attribute and their performance was thoroughly compared. The confidence associated with each prediction reflects the strength of prediction.

From the demonstration point of view, the main objective of this work is to assist the end-user (e.g., an engineer, analyst or data scientist) in understanding the influence of various attribute values on the prediction made by the ML model. Given a datapoint, the model predicts whether the LoS exists at the location (represented by the datapoint) or not. The objective is to empower the end-user to understand how the LoS becomes available or unavailable, given wave propagation properties in a particular datapoint. This relationship is not easy to understand due to multiple non-linearities in data and ML methods have not been fully explored in this regard. If ML predictions can reach good approximations, then the MS can be enhanced with a predictive component that can timely trigger a pro-active handover or engage with an NLoS component in the network, to establish better connectivity before the connection with current BS is interrupted or fully lost.

Once trained, these models can already be interactively explored using the Model Simulator feature of RapidMiner Studio. The extended work described in this section refers to a web-based demonstrator application that could bring this interactive exploration capability as a stand-alone application, potentially with visual components not currently available in RapidMiner Studio. The objective is to assist the end-user by revealing insights on how different input attributes effect the distribution of the two classes as predicted by the ML model. The conceptual design of this demonstration application is shown in Figure 4-10.

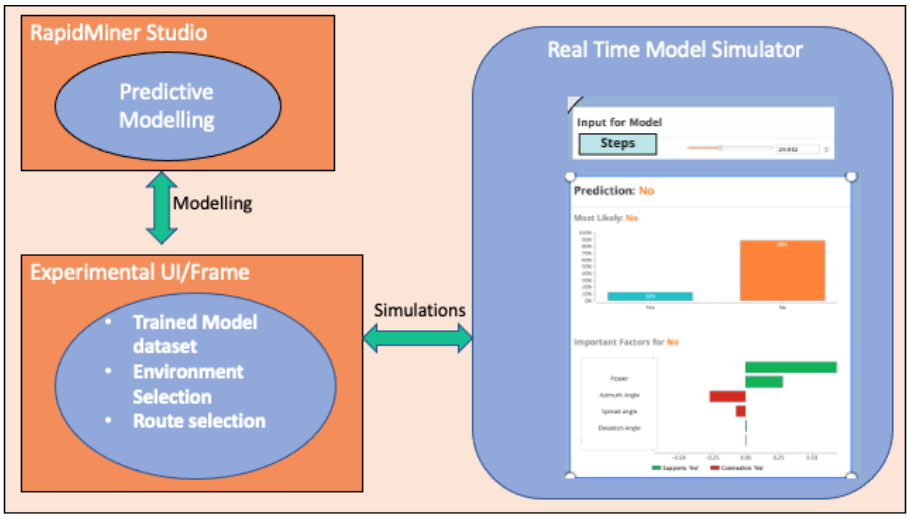

Figure 4-10: Conceptual design to explore the influence of features on ML predictions

As illustrated diagrammatically, after a predictive ML model is trained on the data, a model simulator component can interactively explore the influence of attributes on the prediction made by the ML model. In the following, we present the user interface and the associated features of the web-based demonstrator application.

Description of the Demonstrator Features

The Homepage for this particular scenario is described in Figure 4-11, along with a brief discussion of the problem definition and strategy. This figure contains three images. The first image (to the left) is a blueprint for the outside site where the measurements for the channel modelling were taken. The geometrical conditions, including link pathloss, delay spread, angle spread at the BS and MS, relative coordinates of the BS and MS, and lastly the likelihood of LOS, are shown in the second image (shown at the right side). In addition, the third image (at the bottom of the page) shows how the condensed parameters obtained from the extensive channel sounding were constituted in a dataset, which was further used to train and test the ML model by implementing a RapidMiner ML pipelines. Given the condensed parameters, feature selection and parameter tuning for the training set were carried out and tested for the prediction of LOS of a connection. In general, ML algorithms aid in the extraction of important aspects from the data for potential forecasts. Therefore, to strengthen prediction capabilities of the LoS/NLoS identification without knowing the specificity of data, all tested ML systems were validated using test datasets.

Figure 4-11: Demonstrator Homepage

The main part of the demonstrator application is developed as an interactive Dashboard, whose user interface is shown in figures Figure 4-12, Figure 4-13, **Error! Reference source not found.** – placed separately due to the space limitation. From the demonstration point of view, the main objective of this work is to assist the end-user (e.g., an engineer, analyst, or data scientist) in understanding the influence of various attribute values on the prediction made by the Machine Learning (ML) model. Given a datapoint, the model predicts whether the LoS exists at the location (represented by the datapoint) or not. The topology inherent in the dataset may hold arbitrarily complex interdependencies among attributes, which also vary with the density of BS and MS in a given dataset. Hence, the objective is to empower the end-user to understand how the LoS becomes available or unavailable, given wave propagation properties in a particular datapoint. Therefore, in summary, this demonstrator assists in explaining the predictions by ML model and the condensed parameters. This part of application focuses on various aspects. The first step is to the import the data in the demonstrator. This is performed using the “Import Data” button (highlighted by a green rectangle) in **Error! Reference source not found.**. The pre-requisite condition is that the dataset must contain the prediction and label (ground truth) attributes for LoS connectivity. After the data is uploaded, the dataset is shown in the tabular view with all the attributes along with the original label and predicted LOS with their respective confidence scores.

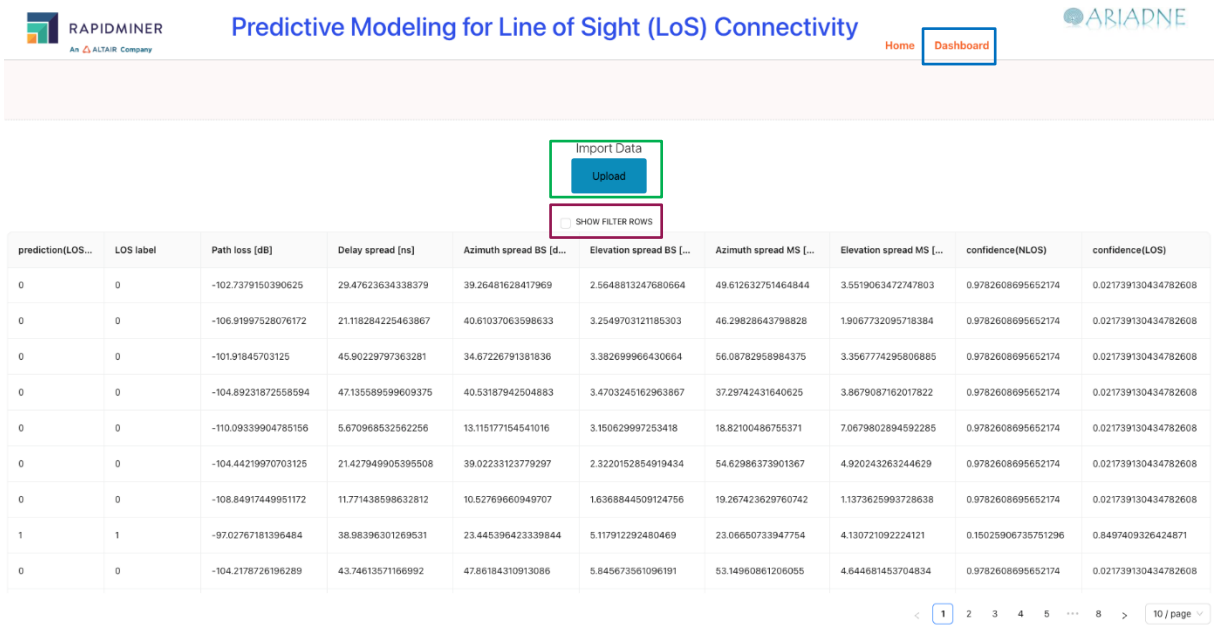

prediction(LOS...	LOS label	Path loss [dB]	Delay spread [ns]	Azimuth spread BS [d...	Elevation spread BS [...	Azimuth spread MS [...	Elevation spread MS [...	confidence(NLOS)	confidence(LOS)
0	0	-102.7379150390625	29.47623634338379	39.26481628417969	2.5648813247680664	49.612632751464844	3.5519063472747803	0.9782608695652174	0.021739130434782608
0	0	-106.91997528076172	21.118284225463867	40.61037063598633	3.2549703121185303	46.29828643798828	1.9067732095718384	0.9782608695652174	0.021739130434782608
0	0	-101.91845703125	45.90229797363281	34.67226791381836	3.382699966430664	56.08782958984375	3.3567774295806885	0.9782608695652174	0.021739130434782608
0	0	-104.89231872558594	47.135589599609375	40.53187942504883	3.4703245162963867	37.29742431640625	3.8679087162017822	0.9782608695652174	0.021739130434782608
0	0	-110.09339904785156	5.670968532562256	13.115177154541016	3.150629997253418	18.82100486755371	7.0679802894592285	0.9782608695652174	0.021739130434782608
0	0	-104.44219970703125	21.427949905395508	39.02233123779297	2.3220152854919434	54.62986373901367	4.920243263244629	0.9782608695652174	0.021739130434782608
0	0	-108.84917449951172	11.771438598632812	10.52769660949707	1.6368844509124756	19.267423629760742	1.1373625993728638	0.9782608695652174	0.021739130434782608
1	1	-97.02767181396484	38.98396301269531	23.445396423339844	5.117912292480469	23.06650733947754	4.130721092224121	0.150259067357512 96	0.8497409326424871
0	0	-104.2178726196289	43.74613571166992	47.86184310913086	5.845673561096191	53.14960861206055	4.644681453704834	0.9782608695652174	0.021739130434782608

Figure 4-12: Import Data

Additionally, the results are shown on two panels (Figure 4-12) after the dataset has been uploaded. The user can now interact with attributes in the left top panel to gain a better understanding of how each attribute affects the forecast of LOS connectivity. The user can adjust all slider values (each represents an attribute) within the minimum and maximum range, which defines the beauty of this user interface, and immediately can see the impact on forecasts on the right top panel and bottom panel of the dashboard in the form of three different charts namely Histogram chart, Pie chart and Group Bar chart.

By manipulating the sliders, one can not only develop intuition for the intricate models in form of three different charts but can also view the selected dataset by activating “show filters” checkbox. With the slider settings currently selected on the left panel, this Bar chart shows the most likely situation, which is 85% of NLoS connectivity and only 15.7% for LoS connectivity. Additionally, a Pie chart shown in the bottom left panel provides a clear comparison between actual vs predicted NLoS and LoS cases. Viewed together, the two pie charts allow a visual interpretation of the confusion matrix. When considering the current set of values in, the likelihood for predicted NLoS vs. observed NLoS is slightly greater by 3% however it is slightly lower for LoS connectivity by 3%, which attests to the good level of prediction accuracy. The Group Bar Chart (shown in the bottom right panel) further confirms the differences between LoS vs NLoS connections in terms of their actual and predicted results – thereby providing furher explainability into the model’s prediction. With the slider values as they are, it represents around 85% for NLoS and 15% for LoS connectivity.

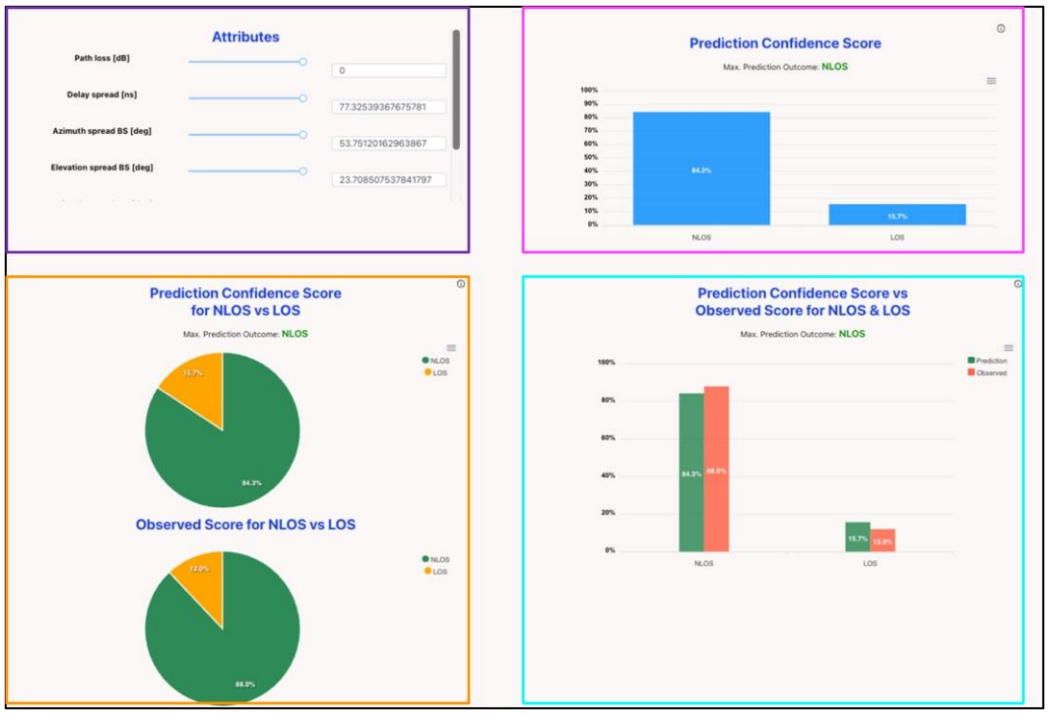

Figure 4-13: Interactive exploration of observed vs predicted and NLOS vs LOS values

Finally, a correlation chart is developed as shown in Figure 4-14 that interactively shows the positive and negative correlation of attributes on the prediction. For the analyst, it is of high interest to explore the most influential attributes for the subset of data as filtered out using the slider values. All charts are interactive with respect to the slider criteria. For instance, the prediction results depicted in the histogram chart (see top right chart of **Error! Reference source not found.**) reflect the distribution of LoS and NLoS datapoints from the dataset that satisfies the current filter criteria. The effect of this criteria on the Correlation chart is depicted in **Error! Reference source not found.**. The chart shows green and red bars to the right and left respectively, where green bars show how certain attributes (in this case, “Path loss” and "Elevation spread BS”) are positively correlated, while the red bars are negatively correlated to the prediction.

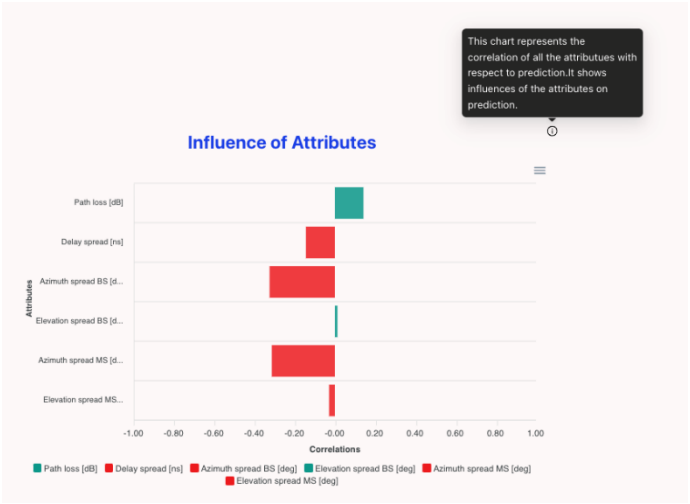

Figure 4-14: Correlation chart showing positively and negatively influencing attributes

In this way, the complexity hidden in the model is better understood by the domain expert regarding the critical role different wave and channel properties play in a given environmental model. This understanding is vital for maintaining reliable and continuous LoS or NLoS based connectivity.

Conclusion

In this part of our work, we developed a demonstration application that enables the end-user to interactively explore the influence of input attributes such as steps in a route, delay spread, the azimuth angles related to the BS or MS, etc. on the model's predictions. Using this method, the end-user may quickly develop an intuition about predictions made by complex models. These insights may be very helpful when designing a network for coverage maximization of an indoor or outdoor environment or when deploying ML models on MS device that make autonomous decisions regarding connectivity management.

4.2 Deep Reinforcement Learning for B5G Wireless Communications

This section includes the result for the Deep Reinforcement Learning demonstrator already presented in D5.2. Since results in D5.2 were already final, this section simply contains the very same material from D.2, included here for the sake of completeness.

Future wireless networks beyond 5G (B5G) are expected to meet the massive demand for data rates especially for the extended reality (XR), augmented reality (AR) and mixed reality (MR). In order to meet various requirements, the future new radio not only considers the sub-6 GHz but also takes millimeter-wave (mmWave) band and terahertz (THz) band into implementation. Downlink beamforming technique has attracted attention from both industry and academic. When the UEs are moving, the base stations (BSs) need to have effective mechanism to allocate proper beamforming vector to the moving UEs. This leads to our motivation to address this research direction in order to make the UEs'; real time interaction with the environment easy by using deep reinforcement learning (DRL).

In general, the system capacity of wireless communications is represented by the weighted sum rate when the UEs have different priority and require different capacity. The summation of the achievable rate of all UEs can be also the overall throughput representation of the network. We consider single beam/multi beam selection for downlink multi-UE MISO scenario.

In this section, we extend the simulation results from ARIADNE D4.4, where we illustrate dynamic beam selection from a predefined codebook beam set to serve multiple UEs at the same time.

We use proximal policy optimization (PPO) based actor-critic algorithm for distributed DRL to implement dynamic beam selection scenario.

4.2.1 Demonstration Scenario 2.1: Deep Reinforcement Learning for Beamforming Optimization

4.2.1.1 Implementation of DRL for Beamforming Optimization

An agent corresponds to the base station (BS) and the actions correspond to codebook selection. In Figure 4-15, the base station predicts one or more beams from the predefined codebook beam set to serve moving UEs.

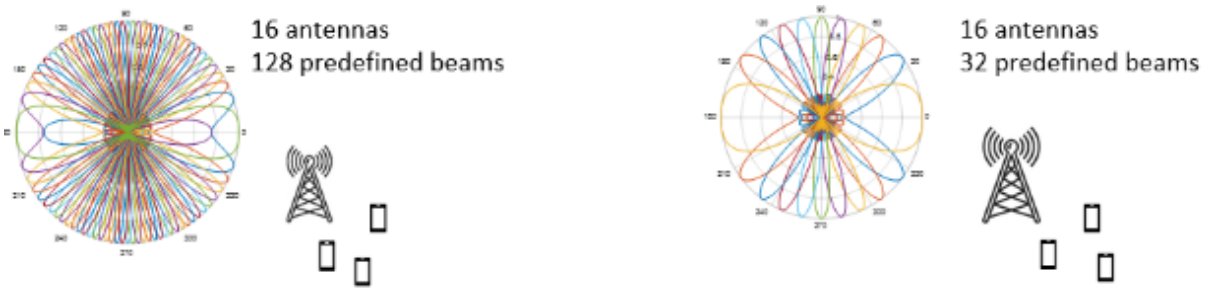

Figure 4-15: Predefined beam codebook selection

The objective is to maximize the cumulative reward, which is defined as the sum of the UEs data rates. The environment (observation space) is modelled by information related to the signal-to-interference-plus-noise-ratio (SINR) of the UEs and the UEs' positions over time. Environmental states generated over time by the agent's interaction with the environment, as outlined above, are input to a long short-term memory (LSTM) network. The overall approach and information flow is illustrated in Figure 4-16.

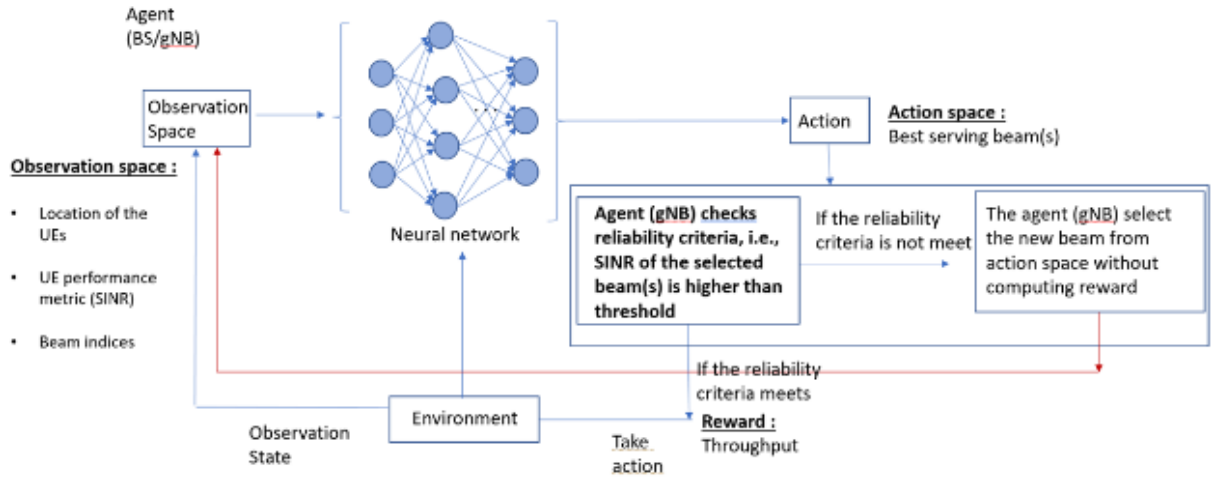

Figure 4-16: Iillustration of single-agent DRL for beam prediction with the association of observation space, environment, and action space

4.2.1.2 Demonstration Results

In this section, the simulation results are extended from ARIADNE Deliverable D4.4, Chapter 6. Figure 53 shows the reward function versus number of episodes.

The BS allocates codebook beam to serve 10 UEs at the same time. We assume that the BS deploys 16 antennas with 16 predefined beams, and in the other setup, the BS deploys 16 antennas with 32 predefined beams. The UEs are randomly located near by the BS. UEs are close to each other, and the UEs move to the same direction with 3km/h speed. From Figure 4-17, when the BS select an optimal beam from 32 predefined beams, the throughput is higher than selecting from 16 predefined beams.

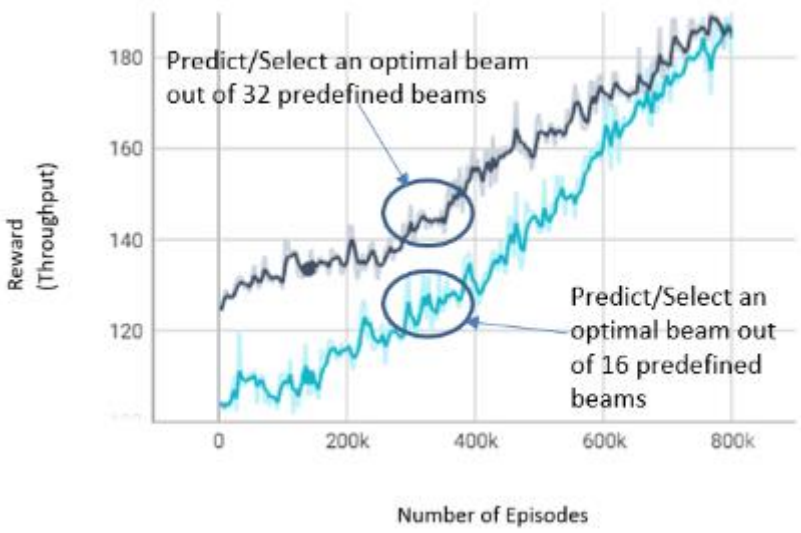

Figure 4-17: Reward versus number of episodes

In Figure 4-18, the value explained variation versus reward is shown, where we can see that the value explained increases and converge. This means that the model learns and converge to the optimal solution. The histogram of reward functions is shown in Figure 4-19.

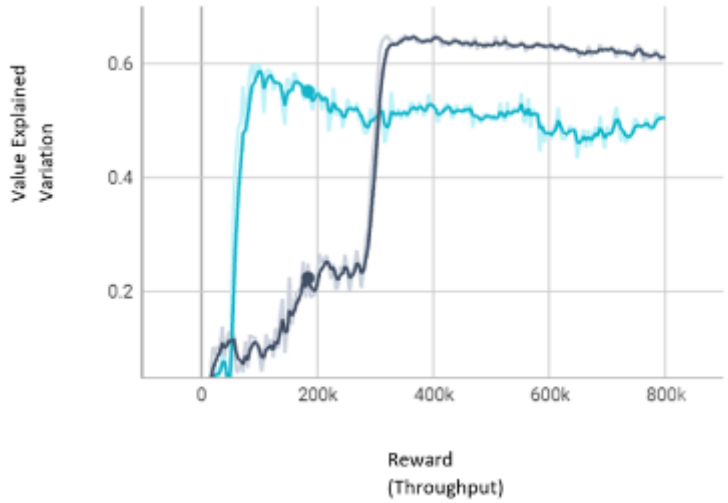

Figure 4-18: Value variation versus reward

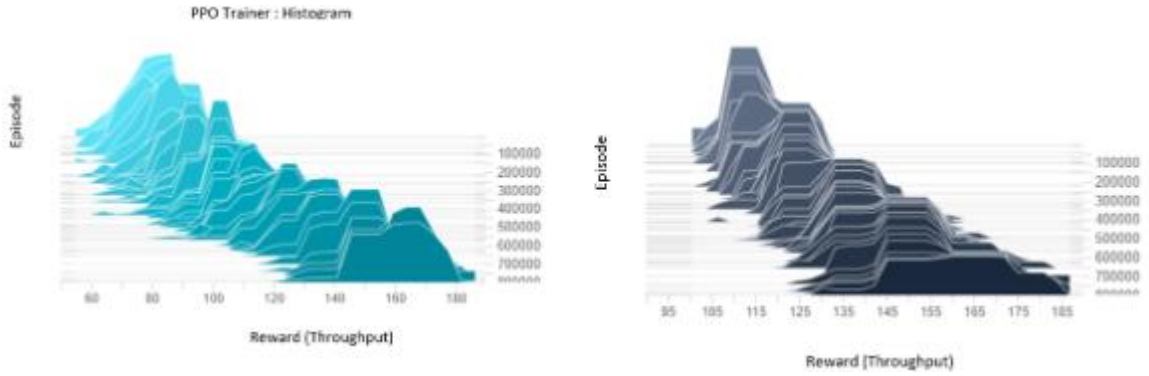

Figure 4-19: Histogram of Reward

In Figure 4-20, the BS allocates multiple beams to UEs where the BS allows more than one UE to be served by the same beam. In this case, the BS can select 4 beams to serve 20, 25 and 30 UEs at the same time. The reward/throughput of 30 UEs is the highest, although the intracell interference is high due to high number of UEs. The throughput is still increased significantly, this means that the reinforcement learning model work effectively. The BS can select optimal beams to maximize the system throughput.

Furthermore, we can recheck the convergence of the algorithm by checking the policy loss function in Figure 4-21. We can see that the policy loss is decreasing and converge after some episodes to reach convergence.

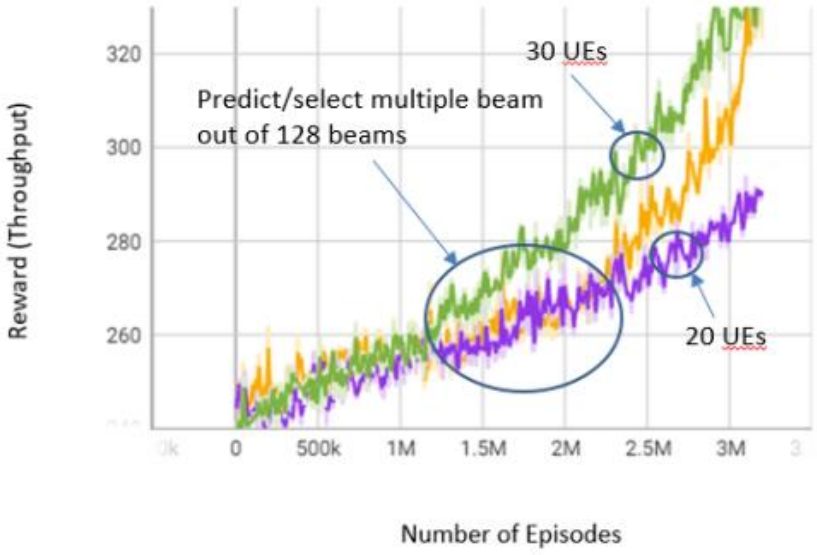

Figure 4-20: Reward versus number of episodes

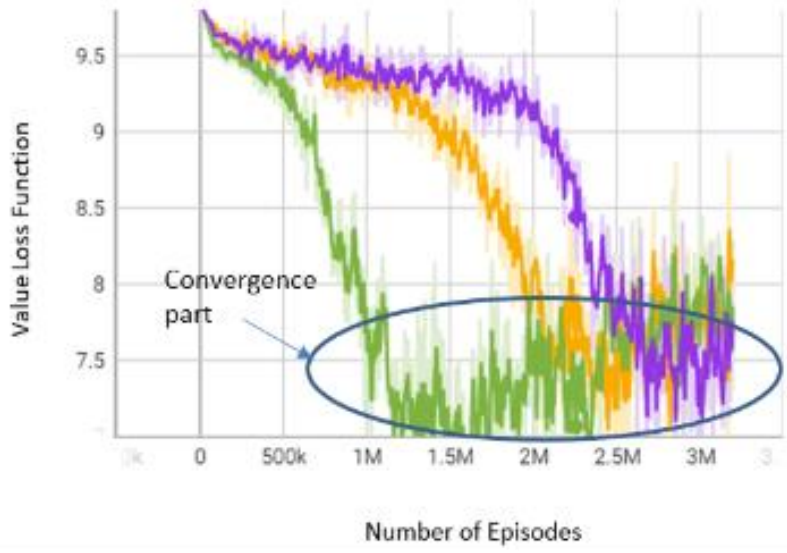

Figure 4-21: Value loss function versus number of episodes

The histograms of the cases when BS/gNB serves 20, 25 and 30 UEs are presented in Figure 4-22. The x-label represents reward and y-label represents number of episodes.

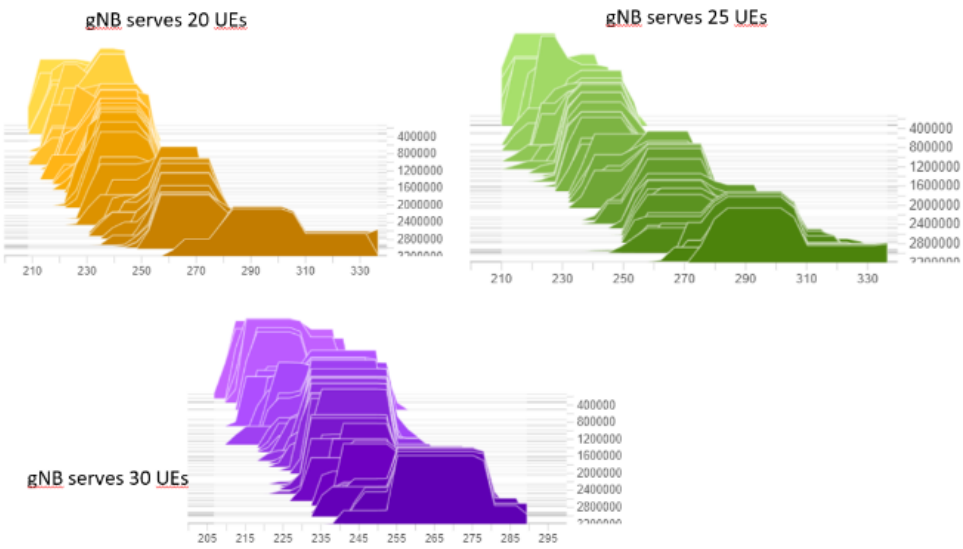

Figure 4-22: Histogram of reward when BS/gNB serves 20, 25, and 30 UEs

4.3 Complex Event Forecasting for Handover Reduction

The objective of this scenario is to demonstrate the reduction of handover events during a simulation session of a D-band network by harnessing AI prediction tools. Specifically, our aim is to monitor an area where multiple UEs are moving and predict the load of APs ahead of time, in a given time frame. This prediction will help us to establish a ranking for each AP for every time slot of the simulation session which will be exploited to minimize the total number of handover incidents throughout the simulation.

To achieve this goal, we initially utilize the system-level simulation platform of D-band networks described in D4.4 and employs the Ford-Fulkerson algorithm for UE-AP association. Additionally, we leverage the capabilities of the ML prediction tool (Wayeb) to forecast the load on APs and determine their corresponding ranking.

Finally, we present the number of handover incidents for each time slot within a given simulation scenario, comparing results with and without the implementation of the ML prediction tool. The aim of the present software demonstration scenario is to highlight the reduction in handovers achieved through the deployment of Complex Event Forecasting techniques.

4.3.1 Demonstration Scenario 3.1: Handover reduction in time evolving scenarios using FFA for UE-AP association

Brief Description of the System Level Simulation Platform

In this scenario, we exploit the system level simulation platform described in Deliverables 4.3 & 4.4. Specifically, we consider a geographical area, which is assumed to be a square with dimensions 50 m × 50 m. Furthermore, 4 obstacles are placed within this area, which are modelled as rectangular parallelepipeds with dimensions 10 m × 10 m × 5 m. They are located uniformly and symmetrically in the simulated area. Also, there are 5 APs (magenta dots in Figure 4-23), which are fixed in predefined

coordinates (Table 4-2). They are placed at height of 2 m from the ground. Moreover, we assume the presence of 45 UEs within the simulated area (Figure 4-23).

In order to involve time evolution, it is assumed that a simulation session has duration T = 1000 sec. The simulation session is divided into successive time slots. Each of them has duration dt = 0.5 sec (i.e., the session consists of 2000 time slots). For the mobility of the UEs, we exploit the following model. Firstly, UEs' initial place is chosen randomly within the periphery of the simulated area. Then, for the first 1000 time slots of a simulation session, if y-coordinate of a UE belongs in the interval [-25, 10], then the UE has destination AP1, AP3 or AP4 with probability equal to 1/3. On the other hand, if y-coordinate of a UE belongs in the interval (10, 25], UE has destination AP1 or AP4 with probability equal to 1/2. For the next 1000 time slots of the simulation session, the destination of a UE is set randomly within the simulated area. As an example, the trajectories of 8 UEs within the simulated area are demonstrated in Fig.1 by the multicolor lines.

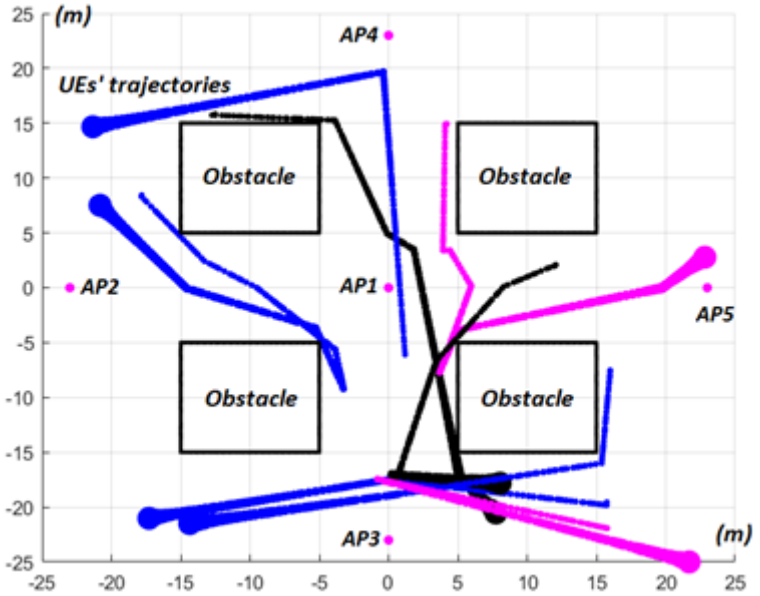

Figure 4-23 Trajectories of 8 UEs within simulated geographical area. The largest dot of a specific trajectory corresponds to the initial placement of the UE, while the smallest one corresponds to its final position.

Table 4-2 APs coordinates

	AP1	AP2	AP3	AP4	AP5
x (m)	0	-23	0	0	23
y (m)	0	0	-23	23	0

UE-AP association

For the UE-AP association, we make the following assumptions. The wireless link between a UE and an AP is considered as Line of Sight (LOS) if the line sector between UE and AP is free of obstacles, while it is assumed to be totally blocked, if the line sector intersects with an obstacle. If the link between UE and AP is totally blocked, the received power of the UE from the specific AP is equal to the default noise level. In our case, the default noise level is considered to be -128 dBm. In order to determine the

received power of a UE from every AP where the link is LOS, we make use of Friis's equation. For the examined case, it is considered that the transmitted power from each AP is P_T= -5 dBm, the gains of transmission and reception antennas are G_T= 14 dBi and G_R = 7 dBi, respectively, while the path loss exponent values and the respective standard deviation of large-scale fading for LOS links for carrier frequency f = 142 GHz, are considered to be β = 2.1 and σ = 2.84 dB, respectively. The required received power threshold so that an AP can serve a UE is set at P_{thr} = -90 dBm.

Furthermore, each AP has total available bandwidth 7 GHz, divided into 14 slices of 500 MHz each one. Moreover, we assume that an AP allocates one bandwidth slice to an associated UE.

A common criterion to determine in which AP a UE will be allocated, is the level of the power that the UE receives from each AP of the network. Specifically, a UE is allocated to the AP that provides the highest level of received power (the so-called conventional allocation (CA) method). However, an AP can only serve a maximum number of UEs, due to bandwidth limitations. Thus, if an AP is overloaded, (i.e., it has already allocated its entire available bandwidth), any new request for service from other UEs will be rejected. Hence, in the considered case, an AP can serve up to 14 UEs.

Hence, some UEs would not be served according to CA method, although they could be potentially served from other APs that provide them power over the required threshold and have unexploited bandwidth slices. To maximize the number of served UEs of a given network for a specific time slot, we make use of Ford-Fulkerson max flow algorithm (FFA). FFA is an algorithm that determines the maximum flow between two specific nodes of a given graph. In the considered case, FFA indicates the maximum flow between a source node and a sink one of a given graph that corresponds to the network status for a specific time slot of the simulation session.

Such a graph is depicted in **Error! Reference source not found.** for a graph that consists of a Source node, N' nodes corresponding to the non-served UEs, M nodes corresponding to APs and a Sink node. Here, N' ≤ 45 and M = 5. Source node is connected to each non-served UE node. Every non-served UE node is connected with every AP node, while each AP node is connected to the Sink node. The capacity of the edges between Source node and UE nodes is equal to 1 (i.e., the number of bandwidth slices that a UE requests). The capacity of the edges between the *i*-th non-served UE node and the *j*-th AP node, where *i*= 1, 2, ..., *N*' and *j* = 1, 2, ..., *M*, is equal to 1 if the power of the *i*-th UE received from the *j*-th AP is over the predefined threshold, P_{thr}, and 0 otherwise.

The capacity of the edges between the node of the *j*-th AP and the Sink node is equal to *n-l(j)*, where *n* is the total number of available bandwidth slices at each AP (i.e., *n* = 14), respectively and *l(j)* the number of exploited bandwidth slices of the *j-th* AP. Namely, the capacity of these edges is equal to the number of available bandwidth slices of each AP, respectively.

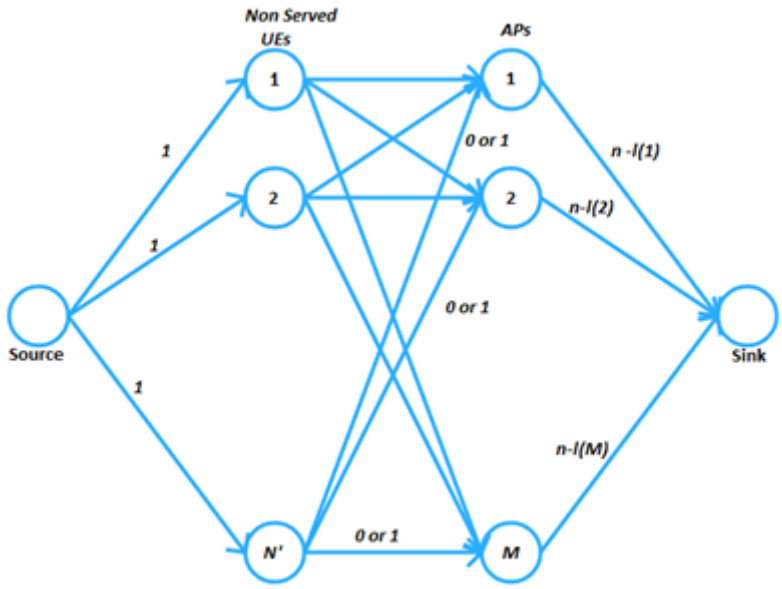

Figure 4-24: Network's graph for the application of max-fow algorithm (FFA) towards UEs allocation to APs.

Handover Reduction Using Complex Event Forecasting

Although the use of FFA ensures the maximization of served UEs, in time evolving scenarios, there is an increase of handover events, i.e., events where a UE cannot be further served from the AP it was associated with and asks to be served by a new one. However, this procedure demands extra network resources.

Towards that direction, we are exploiting the capabilities of the AI prediction tool (i.e., Wayeb) described in Deliverable D4.4, Chapter 4. Specifically, in scenarios involving time evolution, APs could be ordered in the network graph of the FFA in a descending manner, according to the load score that Wayeb forecasting engine provides for each of them. Since FFA prioritizes APs to serve a non-served UE according to that order, the main goal of deploying this method is the association of a UE to an AP at a specific time instant, which will be also able to provide service in future time slots with high probability. Essentially, the main idea is the following: the higher the percentage of UEs' requests to a given AP in the future (i.e., the load score of the AP), the higher the probability that a random UE will request connection to the specific AP.

Demonstration of Handover Performance with and without AI forecasting

Regarding the visualization of the procedure described above, namely the system level simulations, important metrics are monitored, i.e., the number of handovers for each time slot of the simulation session accompanied with the UEs' movement within the simulated area, in order to show the impact on system performance by introducing intelligence through forecasting of service requests among the APs of the network. Such examples are depicted in Figure 4-25 to Figure 4-28, respectively, where the snapshot of the placement of UEs within the simulated geographical area is provided together with the APs' load with and without AI and the respective Wayeb score for each AP (Figure 4-25 and Figure 4-27). The time evolution of handovers with and without enabling AI is shown in Figure 4-26 and Figure

4-28. The performance improvement is apparent when forecasting is deployed in comparison with the case where no forecasting is provided and is depicted in animated manner.

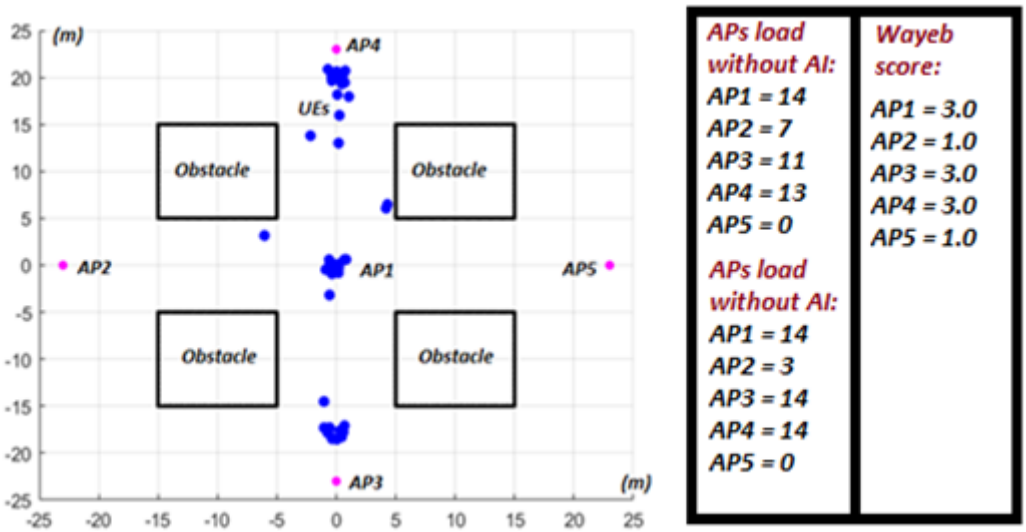

Figure 4-25 Snapshot of UEs' placement (blue dots) within the simulated area at the 131st time slot of the simulation session. At the right side, the load of each AP is provided with and without AI together with Wayeb score.

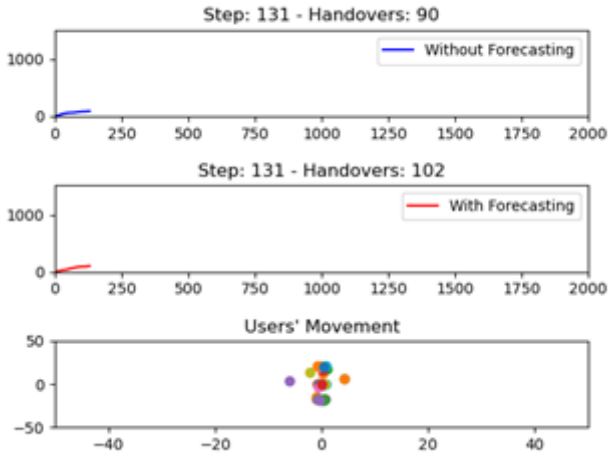

Figure 4-26 Snapshot of time evolved handover performance with and without forecasting at the 131st time slot of the simulation session

Figure 4-25 and Figure 4-24 correspond to the 131st time slot of the simulation session, while Figure 4-27 and Figure 4-28 correspond to the 1489th time slot of the simulation session.

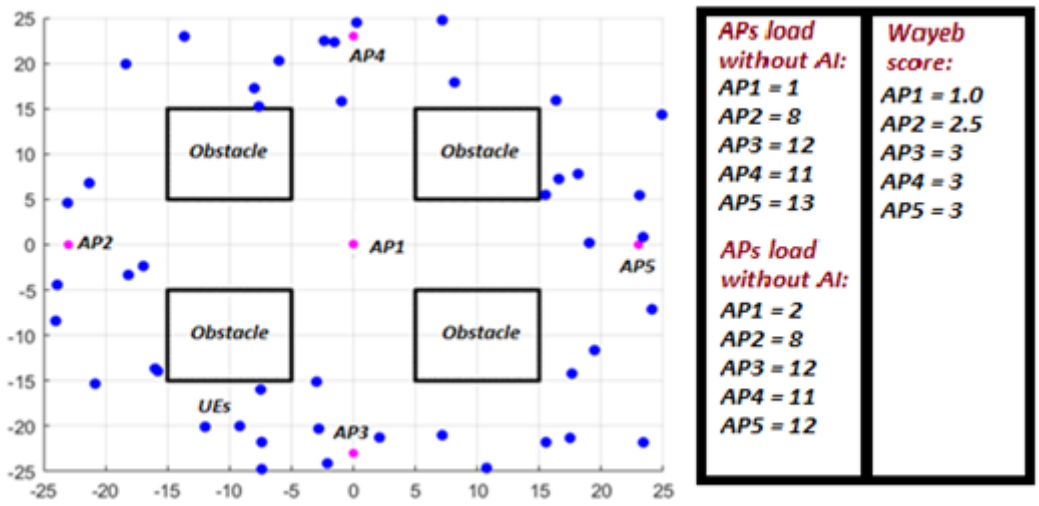

Figure 4-27 Snapshot of UEs' placement (blue dots) within the simulated area at the 1489th time slot of the simulation session. At the right side, the load of each AP is provided with and without AI together with Wayeb score

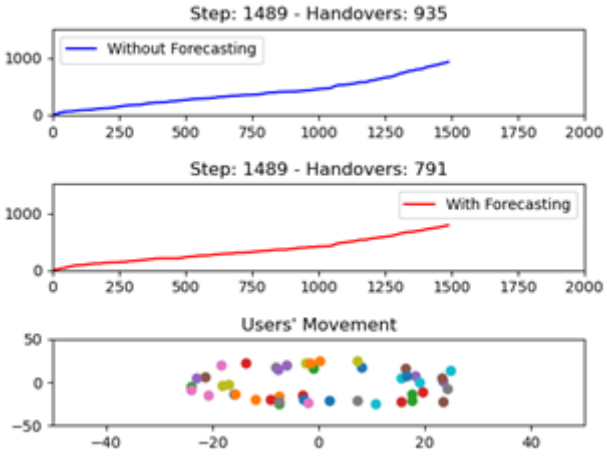

Figure 4-28 Snapshot of time evolved handover performance with and without forecasting at the 1489th time slot of the simulation session

5 Conclusions

This deliverable "D5.3: Report on the final demonstrator" presents the final measurements and results carried out in ARIADNE for its varied hardware in order to assess the different technologies and architectures researched within the project. It should be noted, that in the final demonstrator deliverable D5.3 all the intermediate results shown here are further updated and final conclusions are drawn.

The results from the PtP Los hardware demonstrator were presented while the indoor and outdoor testbeds were described. An outdoor error-free link in the frequency range of 150GHz up to 160GHz in a distance of 226 m was presented based on the main hardware blocks – the BBU of ICOM and the

RFU of IAF – that were developed within WP3. This demonstrator is leveraging the advantages of the spectral-efficient polarization multiplexing technique performed by the RFU in synergy with a powerful XPIC and strong channel impairments mitigation capabilities in the BBU, achieving bit rates up to 13Gbps.

For the second hardware demonstrator, an MTS-enabled PtP NLoS link making use of all of the developed D-band hardware components of WP3, namely the MTS sample, directive dielectric lens antennas, and the RF frontend. This demonstrator was presented in EuCNC in Gotheburg, showcasing a stable additional wireless channel between two sources via anomalous reflection from a specifically designed environment addressing ARIADNE Pillar II. Here the demonstration scenario and the testbed description along with the implementation of the dielectric lens antennas, along with their measurement and results.

Finally, regarding the software demonstrations, which aim at highlighting how ARIADNE incorporates intelligence into various aspects of network management, three main use cases have been selected and presented, namely, (i) AI/ML application for LoS-aware connectivity, (ii) Deep Reinforcement Learning for 5G/B5G Wireless Communications, and (iii) Complex Event Forecasting for Handover Reduction.

The implementation of the software demonstrations was further refined towards their final stage. The software tools and the results showcased are part of the research work conducted within WP4. However, it is noted that more software tools were exploited, if necessary, for the needs of the demonstration. In the present deliverable, the provided information summarizes the main technical/technological aspects of the three demonstration cases and describes the features and metrics that can be visualized and/or animated to showcase the selected scenarios and highlight part of the ARIADNE achievements on incorporating intelligence in D-band networks by means of AI/ML techniques.

References

1. C. Bian, W. Li, M. Wang, X. Wang, Y. Wei, and W. Zhou, “Path Loss Measurement of Outdoor Wireless Channel in D-band,” *Sensors*, vol. 22, no. 24, p. 9734, Dec. 2022, doi: 10.3390/s22249734.
2. S. Sun *et al*., "Investigation of Prediction Accuracy, Sensitivity, and Parameter Stability of Large-Scale Propagation Path Loss Models for 5G Wireless Communications," in *IEEE Transactions on Vehicular Technology*, vol. 65, no. 5, pp. 2843-2860, May 2016, doi: 10.1109/TVT.2016.2543139.
3. ARIADNE Project, "Deliverable 3.4 - "Report on fabricated MMICs and frontend performance," 2020.
4. S. Kosulnikov, F. S. Cuesta, X. Wang, and S. A. Tretyakov, Simple link-budget estimation formulas for channels including anomalous reflectors, *IEEE Transactions on Antennas and Propagation,* vol. 71, no. 6, pp. 5276-5288, 2023.
5. S. Kosulnikov, X. Wang, S. A. Tretyakov, Discrete impedance metasurfaces for 6G wireless communications in D-band, Preprint https://arxiv.org/abs/2302.07313, 2023-